REVIEWS OF
MODERN PHYSICS

VOLUME 45, NUMBER 2, PART I APRIL 1973

Inner-Shell Vacancy Production in Ion-Atom Collisions*

J. D. GARCIA†
University of Arizona, Tucson, Arizona 85721
and
R. J. FORTNER, T. M. KAVANAGH
Lawrence Livermore Laboratory, Livermore, California 94550

Theoretical and experimental work relevant to the creation of atomic inner-shell vacancies in collisions of ions and atoms is reviewed. The experimental data on total excitation cross sections and electron and x-ray emission spectra are discussed in some detail. Energy loss data from inelastic scattering experiments involving heavy ions are also reviewed. An attempt is made to relate the different kinds of data to one another and to the available theoretical models. Excitation by the light ions (protons, alpha particles) has been well described theoretically in terms of perturbation by an incident point charge. However, no comprehensive model yet exists for the case of incident heavier ions, although the heavy-ion data for low collision velocities support an interpretation based on the formation of a transient quasi-molecule. The literature has been reviewed to about April 1972.

CONTENTS

1. INTRODUCTION

Although investigations of inner-shell excitation by heavy particle impact date back 40 years or more, only in the last decade have experiment and theory begun to yield a cohesive picture of the attendant events. These recent developments have been due in part to the application of experimental techniques new to this area. This new evidence has in turn spurred development of theoretical models.

This paper presents a guide to the various manifestations of the excitation of inner-shell atomic electrons. The direct evidence, emission of characteristic x rays and electrons, is augmented by examination of total energy losses in ion–atom collisions. It is assumed that in a collision that creates an inner-shell hole, the atomic systems are reasonably well separated prior to the

* Work performed under the auspices of the U.S. Atomic Energy Commission.
† Supported in part by grants from the National Aeronautics and Space Administration, the Office of Naval Research, and the U.S. Office of Aerospace Research.

emission of the observed photons or electrons. If the collision partners involved were very close at the time of emission, the observed energies of the decay products would differ by varying amounts, depending on the separation; that is, they would be broadened as well as shifted in energy. In our opinion, no definitive data on such a variation exist at this time.

Our aim is to present and criticize some of the pertinent experimental results, employing available theoretical models to relate the various kinds of experimental data. While there is, at this time, no complete theoretical framework for understanding *all* aspects of such collisions, many major features are amenable to explanation. Such a presentation should provide an overview which will help to generate new experiments in areas where data are lacking, and to stimulate new theoretical developments.

We first discuss protons and alpha particles. The major aspects of inner-shell vacancy production by these projectiles can be understood on the basis of point charged particle perturbations of atomic states. Such projectiles, however, also provide evidence that this picture will become inappropriate for heavier ions. For ions heavier than alpha particles, the deviations of the experimental results from the point charged particle picture have become dominant and a new approach to understanding the collisions is necessary. This is especially true because most of the data are in the low and intermediate velocity ranges.

2. POINT CHARGED PARTICLES—PROTONS AND ALPHA PARTICLES

2.1 Introduction

Inner-shell vacancy production by protons and alpha particles is well understood and provides a good background for the discussion of heavier-ion collisions. As we will see, the data are well characterized by models in which the effect of these ions on atomic systems is considered to be a perturbation by a point charge. Historically, these were the first heavy ions to be used for inner-shell excitations, and the gross features of such events were understood as early as 1933 on the basis of plane wave Born (PWBA) calculations (Henneberg, 1933). Merzbacher and Lewis (1958) have reviewed the field up to 1958.

Recent work in this area has involved extension of the energy range up to 160 MeV, new measurements of the spectral distribution of the emissions, and measurement of the probability of the event as a function of the impact parameter. Substantial effort at systematic exploration of cross sections makes it possible to present at this time a cohesive picture of inner-shell excitation by protons or alpha particles. New theoretical models and refinements of old models have provided a reasonable framework for discussion of the collision events.

2.2 Theoretical Models

The simplest models all make the assumption that the production of an inner-shell vacancy by heavy, charged particle impact occurs as a result of the direct Coulomb interaction of the incident heavy charged particle with the bound electron. Three such formulations have been applied to this problem: The Born approximation (Henneberg, 1933; Merzbacher and Lewis, 1958), the impulse approximation (Gryzinski, 1965; Garcia, 1970), and the impact parameter method (Bang and Hansteen, 1959). The first two of these are "high-energy" formulations, in the sense that they are expected to be valid only for incident particle energies much larger than the binding energies of the electrons. For incident energies in the vicinity of threshold, the electrons can adjust nearly adiabatically to the presence of the proton, and a molecular orbitals model is more appropriate (see Sec. 3).

As a quantitative measure of the meaning of "high energy," let us examine the criterion usually given for the validity of the Born approximation. If Z is the nuclear charge, z_1 the projectile charge, and v the relative velocity, the condition is (Mott and Massey, 1965, p. 111)

$$z_1 Ze^2/\hbar v \ll 1. \tag{2.1}$$

This implies, for proton vacancy production in K shells of not-too-small atoms, that $(m_e E_p)/(m_p u_K) > 1.3\times 10^{-2}$ or $E_p/u_K > 24$, where u_K is the K shell binding energy, and E_p is the proton energy. This is almost identical to the condition for validity of the impulse approximation (see Mott and Massey, 1965, p. 338). We should not expect good quantitative agreement for energies less than or near this limit. It is precisely this condition (2.1) which instigated the impact parameter treatment of Bang and Hansteen (1959).

In a first Born approximation, it is assumed that the incident and inelastically scattered particle can be described by plane waves. The interaction responsible for vacancy production is the Coulomb interaction between the bound electron and the incident particle. The initial and final states of the atom are thus described in terms of a transition from the electron's initial bound state to a state described by a continuum wave function with the other electrons remaining in their initial states. Vacancy production due to excitation of the electron to unoccupied orbitals, rather than to the continuum, is negligible (see Merzbacher and Lewis, 1958, p. 174). The expression for the cross section is conveniently written as a differential in terms of the momentum transferred $\hbar\mathbf{q}$ for ionization into a given final state Ψ_f as

$$d\sigma_{fi}(\mathbf{q}) = 16\pi z^2 (e^2/\hbar v)^2 (dq/q^3) \times \left| \int \exp(i\mathbf{q}\cdot\mathbf{r}) \Psi_f^*(\mathbf{r}) \Psi_i(\mathbf{r})\, d^3r \right|^2, \tag{2.2}$$

where z is the projectile charge, v its velocity, and $\mathbf{r}$ the

coordinates of the electron relative to the atomic nucleus. To obtain the total cross section, this expression must be integrated over all momentum transfers compatible with the production of a final state Ψ_f and summed over all permissible final states (i.e., integrated over all allowable kinetic energies and directions of motion of the ejected electron).

Most of the existing estimates have further approximated the initial state with hydrogenic wave functions with an effective charge Z_s, to account for screening (Slater, 1930). The parameters, θ_s, η_s, defined by

$$\theta_s = n_s^2 u_s / Z_s^2, \qquad \eta_s = (Z_s^2)^{-1}(\hbar v/e^2)^2, \quad (2.3)$$

where n is the principal quantum number of the sth shell, and u_s is the binding energy (in atomic units), are then introduced for convenience in scaling. We note that θ_s is proportional to the ratio of the true binding energy to that predicted by a hydrogenic wave function ($\epsilon_s = Z_s^2/2n^2$), and η_s is proportional to the ratio of the incident energy to ϵ_s. In terms of these parameters, the total cross section for vacancy production in the sth shell is given by

$$\sigma_s = (8\pi z^2 a_0^2 / Z_s^4 \eta_s) f_s(\theta_s, \eta_s), \quad (2.4)$$

where a_0 is the Bohr radius, and f_s is the result of the integration of Eq. (2.2). For K and L shells, the expressions for f_s are given as quadratures by Eqs. (4.12), (4.14), and (4.15) of Merzbacher and Lewis (1958). For K shells this becomes

$$f_K = \int_{w_{\min}}^{w_{\max}} dw \int_{Q_{\min}}^{\infty} \frac{dQ}{Q^2} \mid F_{wK}(Q) \mid^2, \quad (2.5)$$

where $Q_{\min} = w^2/4\eta_s$, $w_{\min} = \theta_K$, $w_{\max} = \infty$, and

$$\mid F_{wK} \mid^2 = \frac{2^7}{1-\exp(-2\pi/K)} \frac{Q(Q+\frac{1}{3}w)}{[(Q-w+2)^2+4(w-1)]^3} \times \exp\left(-\frac{2}{(w-1)^{1/2}} \arctan \frac{2(w-1)^{1/2}}{Q-w+2}\right).$$

A similar expression is available for L shells (Khandelwal and Merzbacher, 1966; Choi and Merzbacher, 1969). The integration limits given here, as discussed by Merzbacher and Lewis (1958), are not exact in that they neglect terms of higher order in the ratio of electron to projectile mass; for most practical purposes however, they are correct. Merzbacher and Lewis (1958) also shows plots of σ_K and σ_L as functions of η for various values of θ.

Bang and Hansteen (1959) have treated approximately the effects which nuclear repulsion of the incident particle produce in the total cross section. They do this by means of an impact parameter formulation in which they then insert appropriate deflection corrections. Without the corrections, their result is identical to the Born result. The major effects are due to the change in the path of the incident particle, which is almost always negligible for heavy particles, and the decrease in kinetic energy of the incident particle, which becomes important near threshold. The resulting changes are negligible for large η, and the cross section is lowered for small η. Figure 2.1 depicts both the first Born approximation and the Bang and Hansteen modification. Further work along these lines has been reported by Hansteen and Mosebekk (1970).

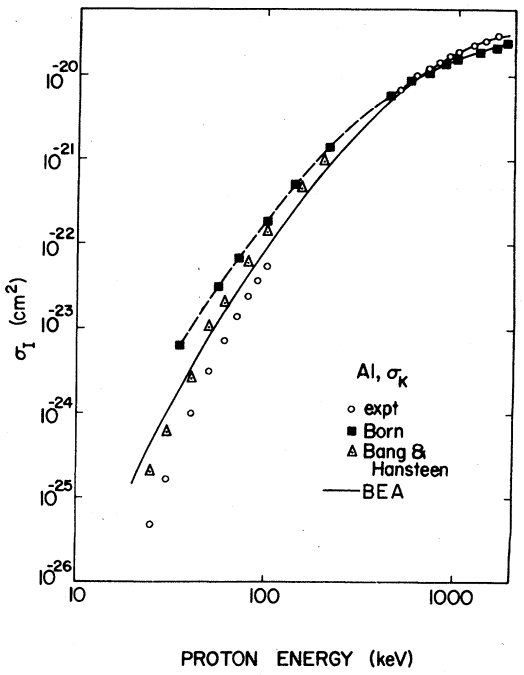

FIG. 2.1. Al K-shell cross sections, displaying comparisons among theoretical estimates (after Garcia, 1970): squares, Born approximation; triangles, Bang and Hansteen model; solid curve, impulse approximation (BEA); circles, experimental points (Khan *et al.*, 1966).

In the impulse approximation, the viewpoint taken is that the dominant interaction producing the transition is a direct energy exchange between the incident charged particle and the bound electron. The role of the nucleus of the target atom is then simply that of establishing the momentum distribution for the electron. The collision is thus viewed as the collision of the incident particle, momentum $\mathbf{k}_1$, with a *free* electron of momentum $\mathbf{k}_2$. The term Binary Encounter Approximation (BEA) arises from this step. The cross section is then summed over all momentum exchange $\mathbf{k}$ compatible with an energy exchange ΔE. This result is integrated over all allowed energy exchanges, and finally weighted by the distribution of electron momenta associated with the bound state. The validity and justification of the impulse approximation are discussed in various recent articles (Coleman, 1969; Vriens, 1969). The form of the impulse approximation which has been

applied actually corresponds to a "restricted" impulse approximation, since momentum and energy conservation have been required in the binary encounter between the incident particle and the electron.

If we recall that the exact quantum mechanical expression for the cross section for the collision of two free charged particles is identical to the classical result, we recognize that all steps in the above procedure, except the determination of the distribution of the initial bound electron momenta, can be carried out classically. We should note that quantum mechanically we should add amplitudes rather than cross sections as stated above. However, for large electronic momentum changes, only one final amplitude is important for each initial state and the sum of the squares of the amplitudes becomes equal to the square of the sums (Vriens, 1969).

We can thus take advantage of the existing classical binary encounter results, which are exactly the required expressions. Equations (1) and (2) from Garcia (1970a) are the appropriate expressions:

$$\sigma_I(v_1) = N_i \int_0^\infty \sigma_i(v_1, v_2) f(v_2)\, dv_2, \tag{2.6}$$

where $f(v_2)$ is the speed (momentum) distribution of the bound electrons, N_i is the number of equivalent electrons having binding energy u, and

$$\sigma_i = \int_u^{E_1} \frac{d\sigma}{d\Delta E}\, d\Delta E.$$

The last integration can be done in closed form, i.e.,

$$\int^{\Delta E} \frac{d\sigma}{d\Delta E}\, d\Delta E = \tfrac{1}{3}\pi \frac{(z_1e^2)^2}{v_1^2 v_2}\left(-\frac{2v_2^3}{(\Delta E)^2} - \frac{6v_2/m_e}{\Delta E}\right) \qquad 0<\Delta E<b$$

$$= \tfrac{1}{3}\pi \frac{(z_1e^2)^2}{v_1^2 v_2}\left(3\frac{[(v_1/m_1)-(v_2/m_e)]}{\Delta E} + \frac{(v_2'^3-v_2^3)-(v_1^3+v_1'^3)}{(\Delta E)^2}\right) \qquad b<\Delta E<a$$

$$= \tfrac{1}{3}\pi \frac{(z_1e^2)^2}{v_1^2 v_2}\left(-\frac{2v_1'^3}{(\Delta E)^2}\right) \qquad \Delta E>a \text{ and } 2m_e v_2>(m_1-m_e)v_1$$

$$= 0 \qquad \Delta E>a \text{ and } 2m_e v_2<(m_1-m_e)v_1 \tag{2.7}$$

where a, b, and v_1' are defined by Garcia (1970a). In this expression, particle 1 is the incident particle of charge z_1, mass m_1, and particle 2 is the bound electron. This model has also been modified to approximate the effects of the nuclear repulsion on the incident particle (Thomas and Garcia, 1969; Garcia, 1970a).

If hydrogenic velocity distributions are used in Eq. (2.6), these impulse approximation results for a given subshell have been shown to obey a scaling law, which states that the product of the binding energy squared and the cross section is a universal function of the incident energy expressed in units of the binding energy, i.e.,

$$u^2\sigma_I = z_1^2 f[E_1/\lambda u, \lambda], \tag{2.8}$$

where z_1 and λ are the charge and mass (in electron mass units) of the projectile. Thus a plot of $u^2\sigma_I/z_1^2$ vs $E_1/\lambda u$ should yield the same results for all target atoms. These are to be compared to the Born scaling factors η and θ defined above. Actually, the separate dependence on λ in the above expression is very weak when $\lambda \equiv m_1/m_e \gg 1$, and f is very nearly independent of λ. [This weak dependence is analogous to the dependence on projectile mass which enters in the Born expressions when the exact integration limits are used in Eq. (2.5).] This universal function for the impulse approximation is analogous to the function $f_s(\theta_s, \eta_s)$ of the Born approximation from Eq. (2.4). In fact, what is usually plotted is $Z_K^4\sigma_K/z_1^2$ vs η_K for K shells, when comparisons between Born and experiment are made. We note that

$$\theta_K^2(Z_K^4\sigma_K/z_1^2) \equiv u_K^2\sigma_K/z_1^2 \tag{2.9}$$

and

$$\eta_K/\theta_K \equiv (m_e/m_1)(E/u_K) \equiv E/\lambda u_K. \tag{2.10}$$

Figure 2.2 shows a comparison of the impulse and Born approximations. The relationships Eqs. (2.9) and (2.10) have been noted in Fig. 2.2 in that $\theta_K^2(Z_K^4\sigma_K/z_1^2)$ is plotted as a function of η_K/θ_K.

The basic difference between the Born and impulse approximations can be illustrated as follows: in the Born approximation the assumption is that the interaction between the incident particle and the atom is weak and can be treated as a perturbation. The probability is thus proportional to the square of the matrix element

$$d\sigma \sim |\, V_{fi}\,|^2,$$

where

$$V_{fi} = \langle \phi_{k'}(r_1)\Psi_f(r_2) \mid 1/r_{1,2} \mid \phi_k(r_1)\Psi_i(r_2)\rangle, \tag{2.11}$$

and Ψ_f, Ψ_i are wave functions appropriate to an electron centered at the nucleus, describing continuum and bound particles, respectively. The interaction

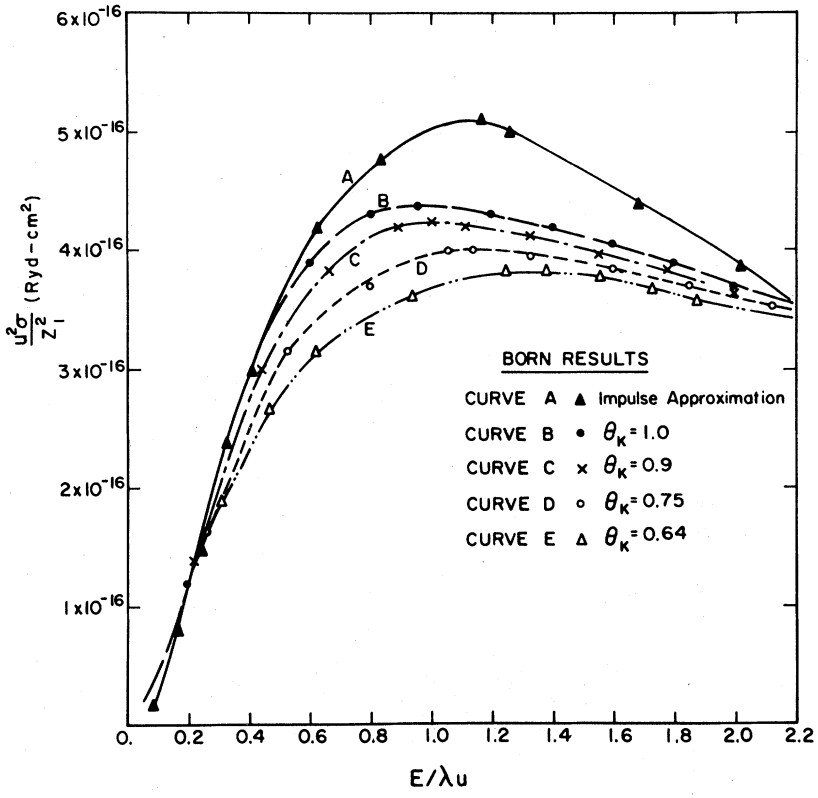

FIG. 2.2. Comparison of Born and impulse approximation (BEA) vacancy production cross sections. Scaled cross sections $u^2\sigma/Z_1^2$ are plotted as functions of scaled energies $E/\lambda u$.

between the incident particle and the electron is thus not exact, since these are not described in terms of Coulomb wave functions relative to one another, but is viewed as a perturbation between atomic states. Exact energy conservation for the problem is assumed. The impulse approximation, on the other hand, treats this interaction exactly, in the sense that the bound electron is viewed as a free particle of definite momentum, scattering with the incident particle. A sum of contributions from the various momenta present in the initial wave function is then made:

$$d\sigma \sim \int f(v_2)\, dv_2 [d\sigma(v_1, v_2)], \qquad (2.12)$$

where $[d\sigma(v_1, v_2)]$ is the *exact* expression for the scattering of two moving charged particles. The electron's final state description thus ignores the presence of the nucleus. Furthermore, in the present use of the restricted impulse approximation, exact momentum and energy balance are required between the incident particle and the electron only, ignoring recoil effects. The reader is referred to Vriens (1969) for further details on the relationship between these approximations.

In view of the previously stated assumptions and approximations, it is perhaps surprising that these models agree as well as they do with experiment. Additional implicit assumptions have been made. For example, the final state in the vacancy production process can be described properly only as a very high lying resonance state. In the Born approximation, however, the description has been simply that of the initial state, but with one inner-shell electron in a continuum state. To the extent that adiabatic "relaxation" and polarization of the remaining electrons occur during the ionization process, this description is inaccurate even within its own framework. For high incident particle velocities and high-Z target atoms, this relaxation is likely to be unimportant for K-shell ionization, but may not be for L shells.

The correct theoretical description of inner-shell ionization is a rather formidable task, and it is not expected that progress in this area will be rapid. As will be seen in Sec. 2.3.1(b), the above simple approximations may suffice for gross descriptions of experimental results to date, but as the experimental techniques become more sophisticated, the theoretical framework will have to be improved.

Neither of the above models is expected to be valid as the incident particle energy approaches threshold. In this connection, Brandt, Laubert, and Sellin (1966) have used the formulation of Bang and Hansteen in an attempt to correct for the adiabatic changes in the energy of the electron due to the presence of the incident charged particle. Their results improve the agreement with experiment—the effect depresses the cross section

at lower energies, since it increases the effective charge seen by the electron at the target nucleus and therefore decreases its average radius. While their correction is not formally consistent, since it uses the full electron–incident particle interaction both as part of the unperturbed Hamiltonian and as the interaction responsible for the transition, it appears that their basic assumption is correct: adiabatic effects must be taken into account in the vicinity of threshold, and will change the predicted cross sections in the direction of better agreement with experiment. A proper theoretical framework for these adiabatic changes could be obtained by starting with a perturbed stationary state method [see Sec. 3.1.4 and Mott and Massey (1965)], and observing carefully the various orders of perturbation theory involved. Brandt *et al.* (1966) have in effect, by using approximate first-order corrected energies, included some second-order terms. However no careful formulation has been carried out to determine whether these are in fact the dominant terms.

2.3 Total Cross Section Measurements

The evolution of an atomic system after the production of an inner-shell vacancy can proceed to a large variety of final states. These all have in common the transition of an electron from a higher orbital into the vacant inner-shell orbital, accompanied by the emission of either radiation or electrons. Many details of the atomic excitation accompanying the vacancy production can be studied by examining the spectral distributions of the x rays and Auger electrons, which we discuss in the next section and in Sec. 3.4. By *summing* over all modes of de-excitation, we obtain a number which is proportional to the probability of producing the original vacancy. The total x-ray and Auger cross sections are the subject of this section.

The x-ray emission is almost completely dominated by one-photon electric dipole radiation, so that the accessible final states are severely restricted by the usual dipole selection rules. Auger emission, on the other hand, proceeds via e^2/r_{ij} (scalar) interelectronic repulsion, so that for the entire system (atom+electron) the selection rules are

$$\Delta L=\Delta J=\Delta S=\Delta(\text{parity})=0.$$

Since the ejected electron may, in principle, have any angular momentum, the number of states accessible to the residual atomic system is unrestricted. These remarks lead to the correct conclusion that the x-ray spectrum should be relatively simple, with the Auger spectrum perhaps richer in information.

By far the bulk of the data on inner-shell vacancy production is in the form of total x-ray production cross sections. The reason for this is inherent in the relative simplicity of the x-ray measurements: x-ray detector systems are less complex, and Auger measurements require gas targets.

We have attempted in this review to discuss experimental data in some detail, with extensive presentation of results in graphical form. For total x-ray production cross sections by point charge projectiles, however, we have deviated somewhat. Because of the large volume of data, and because, to first order, they agree with theory, the experiments are only summarized. They are listed in tabular form in Appendix 1, and the data are compared with theory in a collective manner in Sec. 2.3.1(b).

2.3.1 Total X-Ray Cross Sections

2.3.1(a) Experimental Technique

Many of the investigations since 1958 have employed basically the same experimental techniques described by Merzbacher and Lewis (1958) in their review. Briefly, an ion beam impinges on (and is stopped in) a thick target and the number of x rays produced per incident ion is deduced from the total count rate in an appropriate x-ray detector, which is at 90° with respect to the beam direction. The x-ray detection systems commonly in current use are flow mode proportional counters for low-energy ($h\nu<$a few keV) x-rays and lithium-drifted silicon detectors. This latter type detector has gradually replaced the NaI(Tl) scintillator detector used earlier. If the target surface is oriented at 45° with respect to both the beam and detector so that particle and photon path lengths are equal, the x-ray yield I is given by

$$I[E(R_0)]=n\int_0^{R_0}\exp[+\mu(R-R_0)]\times\sigma_x[E(R)]dR, \quad (2.13)$$

where I is the number of x rays per incident ion, n is the target atom density (atoms/gm), μ is the x-ray mass absorption coefficient (cm²/gm), R_0 is the total range (gm/cm²), R is the residual range, and σ_x is the x-ray production cross section (cm²/atom) at projectile energy E. Since we are interested in the cross section, the above expression is differentiated with respect to range to obtain

$$\sigma_x(E)=-n^{-1}[dI(E)/dE](dE/dR)+(\mu/n)I(E), \quad (2.14)$$

where dE/dR is simply the stopping power (keV cm²/gm) for the projectile in the target material. [Note that $-n^{-1}(dE/dR)$ is often designated as the "stopping cross section," represented as $S(E)$.]

A comprehensive tabulation of stopping power data has recently been provided by Northcliffe and Schilling (1970). This paper contains a useful bibliography of experimental data and theory. The Tables themselves provide interpolations and extrapolations, based on theoretical models, into areas where no experimental data exist. Data for heavy ions, as discussed in Sec. 3, are included. (Much of the experimental stopping power data are of good accuracy—±5% or better—but

in many cases, particularly at lower bombarding energies, it is necessary to rely on interpolations and extrapolations. It is extremely difficult to estimate the uncertainties in stopping power values so obtained.)

The thick target data at different beam energies must be differentiated to obtain the x-ray production cross section. Inaccuracies introduced by this procedure, as well as those introduced through stopping-power data, can be often circumvented by using thin foils as targets, at least for higher projectile energies. In such cases, the energy loss in the foil is small and the x-ray production cross section is then directly proportional to the x-ray yield. Gas targets have also been used recently; they too avoid the difficulties mentioned above, but may introduce fluorescence yield difficulties (see Sec. 3.3.5).

2.3.1(b) Results and Discussion

In order to compare σ_x with models for vacancy production, a knowledge of the fluorescence yield ω is required. This quantity is simply the fraction of vacancies in a given shell which lead to x-ray emission, i.e.,

$$\sigma_x=\omega\sigma_I=[\omega/(1-\omega)]\sigma_A, \qquad (2.15)$$

where σ_x, σ_A are the x-ray and Auger electron production cross sections, respectively, and σ_I is the vacancy production cross section. The direct experimental determination of ω has been the subject of many investigations (Bambynek *et al.*, 1972), but large uncertainties and discrepancies arise. Recently, improved theoretical estimates (McGuire, 1969; Kostroun, Chen, and Crasemann, 1971; Walters and Bhalla, 1971) have been reported.

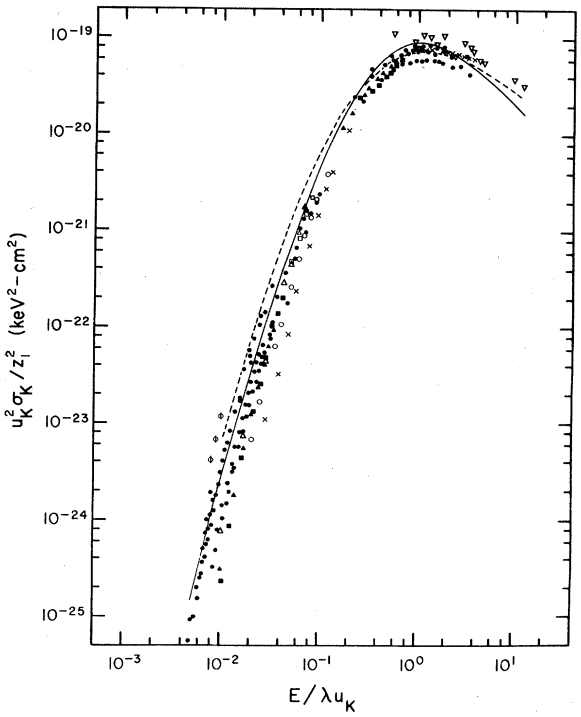

FIG. 2.3. General comparison of Born and binary encounter approximations with experimental K-shell x-ray cross sections by proton impact: dashed curve, Born approximation; solid curve, binary encounter estimate; solid circles, data for elements with $15\leq Z\leq 70$; inverted triangles, 160-MeV protons; open circles with vertical bar, Ta measurements; open and solid triangles, Al measurements; open and solid squares, experimental Mg points; open circles, O data; crosses, C data.

TABLE 2.1. Fluorescence yields.

Element	ω_k
C	2.4×10^{-3}
O	7.7×10^{-3}
Mg	3.01×10^{-2}
Al	3.98×10^{-2}
Ca	0.171
Ti	0.227
Fe	0.362
Ni	0.433
Cu	0.468
Zr	0.761
Mo	0.795
Rh	0.837
Ag	0.860
Sn	0.889
Ba	0.92
Sm	0.94
Tb	0.95
Ta	0.97
Pt	0.97
Au	0.97
Pb	0.97
U	0.98

In order to facilitate comparisons, we present the measured total x-ray production cross sections using theoretically determined fluorescence yields. This provides more direct comparison of the experimentally determined quantity with theory, avoiding the larger uncertainties associated with experimentally determined ω's.

K-shell measurements. The available x-ray measurements are summarized in Appendix 1. These investigations have been extensive, with proton energies ranging from 15 keV to 160 MeV, and targets from $Z=4$ to $Z=92$. Rather than present a plethora of graphical or tabular data, we have chosen to display the data in terms of a "universal" curve, plotting $u^2\sigma_I/z_1^2$ vs $E/\lambda u$, where, as above, u is the binding energy of the shell in question whose cross section is σ_I, z_1 is the projectile charge, E is the projectile energy, and $\lambda=m_1/m_e$ is the projectile mass in electron mass units.

Figure 2.3 shows such a plot for the proton data. The fluorescence yields used for plotting the data in that Figure are given in Table 2.1. Because of the range of target elements involved, it is impractical to assign

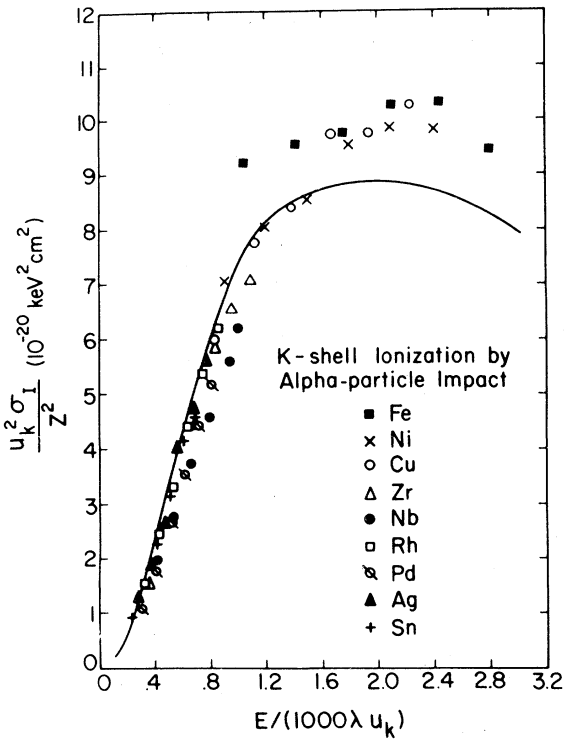

FIG. 2.4. K-shell vacancy production by alpha-particle impact (after Garcia, 1971). The ordinate is the scaled cross section $u^2\sigma_K/Z_1^2$, the abscissa is the alpha-particle energy divided by the K-shell binding energy and the ratio of projectile mass to proton mass, in units of 10^3. (Note, this is not the λ used in the present text.) The data are from Watson (1970); the solid curve is the binary encounter approximation.

each element a new symbol, and we have therefore selected only a few cases for special designation. Not all of the K-shell data referred to in the Table in Appendix 1 have been plotted. Some of those references give ambiguous values of the fluorescence yields. Some are superceded by later works by the same authors [for example, Hansteen and Messelt (1956) by Messelt (1958)]. The data in which thin foils were used all lie above $E/\lambda u > 2\times10^{-1}$. All data for target $Z<15$ are thick target data.

As can be seen from Fig. 2.3, all the data, except for the 160-MeV points, form a reasonably compact curve above $E/\lambda u \gtrsim 10^{-1}$. Below $E/\lambda u \approx 10^{-1}$, the data for targets with $15<Z<70$ continue to define a universal function, but the data for the low-Z elements begin to spread in the direction of smaller cross sections. The theoretical estimates follow closely the behavior of the main group of the data, the Born approximation being closer for $E/\lambda u \gtrsim 3\times10^{-1}$, and the binary encounter estimate being closer below that.

The Ta points may be showing relativistic effects. Jarvis *et al.* (1972) suggest that their measured cross sections should be reduced by a factor of 1.26 to account for the relativistic velocity of the proton. If so, then they should also be plotted at $E/\lambda u$ values reduced by the same factor, since the abscissa also contains v^2. It is apparent that the problem must be reformulated within a relativistic framework in order to properly compare theory with experiment.

It should be observed that data from low-Z targets form a sequence which deviates further from the main group the lower the target nuclear charge. Thus, C, O, Mg, and Al have decreasingly smaller cross sections, vis à vis the main group, as energy is decreased. This trend is evident despite the spread in measurements from different laboratories (the closed symbols are from Khan *et al.* 1965, and the open symbols are due to Brandt *et al.*, 1966) and is probably due to adiabatic effects as proposed by Brandt, Laubert, and Sellin (1966). It has been recently suggested (Basbas, Brandt, and Laubert, 1971) that a power series expansion in the ratio, z_1/Z, of projectile z_1 to target nuclear Z might provide a useful representation; such an approach would accentuate the decrement in the lower Z targets as seen in the data. That an adiabatic adjustment correction is important here provides the first indication of "compound atom" formation, which will be seen to play an important role in heavier ion–atom collisions, as discussed in Sec. 3. (Even for the data from $15<Z<50$, a definite, but less obvious, trend for the higher Z data to lie slightly higher can be observed. For these targets, however, the effect is much smaller and they still form a fairly compact group.)

Comparison of the Bang–Hansteen and Born curves in Fig. 2.1 shows that the Coulomb deflection of the projectile by the nucleus has effects which are important only for $E/\lambda u \lesssim 10^{-1}$. The difference between the two theoretical curves in Fig. 2.3 for these lower energies probably reflects chiefly this effect. For higher energies, the primary difference is probably the neglect of target recoil in the restricted impulse approximation used. At energies higher than those shown, the Born curve approaches a $\ln E/E$ behavior, while the binary encounter curve approaches a $1/E$ behavior; this difference can be attributed to recoil neglect. As can be seen, the results of these two formulations are very similar and similar to the bulk of the data. Appendix 2 contains a table of scaled binary encounter values for further comparisons. We note, finally, that the data in Fig. 2.3 comprise four orders of magnitude in scaled energy and seven orders of magnitude in cross section.

The alpha-particle data have behavior similar to that shown in Fig. 2.3 for protons, and most of the comments made above about proton results apply equally well to alpha-induced x rays. In general, the alpha-particle data have been taken at higher energies and for higher Z targets, so that the grouping is much more compact. Instead of reproducing another general curve, we have selected only the thin-foil measurements of Watson *et al.* (1970) for our discussion. These are shown in Fig. 2.4 taken from Garcia (1971). Unlike Fig. 2.3, the

scales in Fig. 2.4 are linear scales. We wish to make only two points with these data. The first is that the projectile mass dependence predicted by theory is not at wide variance with experiment: the data group very well in terms of these reduced parameters. Second, we note that near the peak of the curve the alpha-particle data tend to lie above the BEA prediction, whereas the proton data tended to be below this curve. This trend will be discussed further in Sec. 2.5. These data lie within 20% of the theory and much closer to a curve defined by the experimental points themselves.

The Born approximation provides the best simple theoretical framework for describing these events. This is true not only because of the agreement noted above, but because it can in principle and in practice be improved. The binary encounter approximation is a simpler model and provides simple expressions and scaling laws, but is less flexible as a general framework. Nevertheless, because of the simplicity of comparison and the agreement with experiment, we will in the following comparisons for *total* cross sections use the binary encounter approximation. The relation to first Born and Bang–Hansteen calculations can be easily gleaned from Figs. 2.1, 2.2, and 2.3.

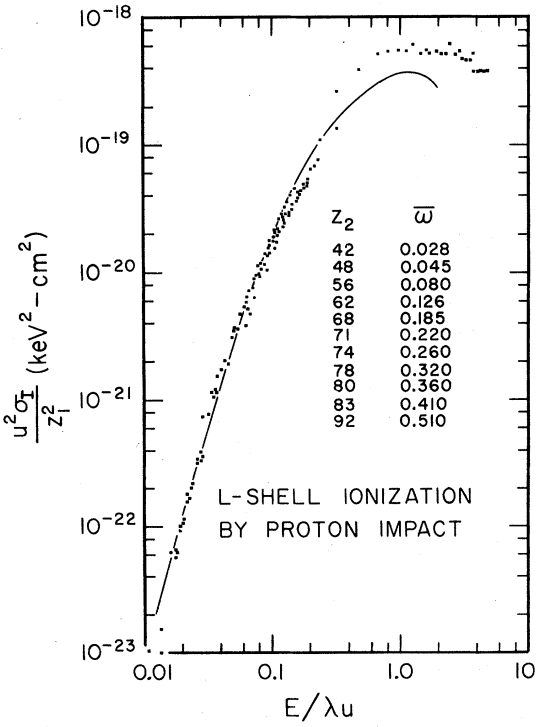

FIG. 2.5. Comparison of x-ray data on L-shell vacancy production by protons with binary encounter theory. The parameters are scaled cross section and particle energy as discussed in the text in connection with the BEA, and data are for target atomic numbers from 40 to 92. The fluorescence yield values used (representative values are listed in the figure) were theoretical values after Walters and Bhalla (1971b). The curve represents the BEA computed for eight equivalent electrons.

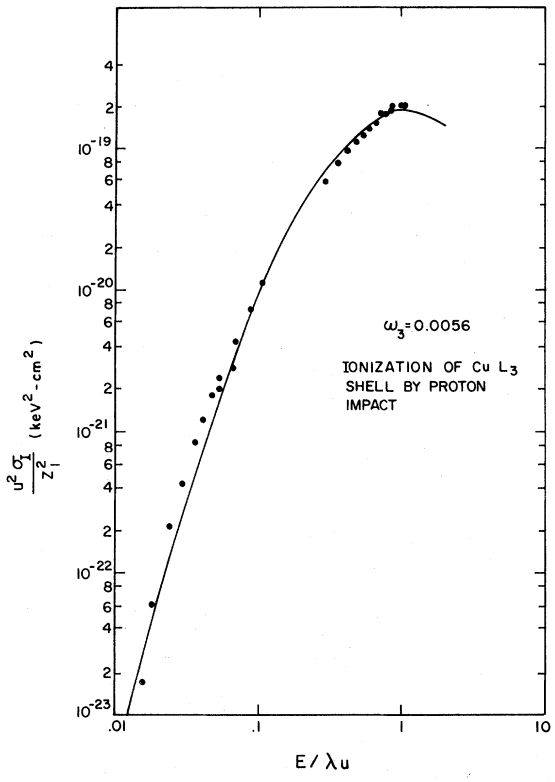

FIG. 2.6. Comparison of x-ray data on Cu L_3 subshell vacancy production by protons with binary encounter theory. The scaled parameters are those discussed in the text, and the fluorescence yield value shown is a theoretical one from Walters and Bhalla (1971b). The BEA curve shown is for four equivalent electrons.

L-shell measurements. The more complicated structure (three subshells) of the L shell as compared to the K shell makes comparison with theory slightly more difficult. We have assumed in our comparison that, since most of the data available are for $Z \geq 29$, the Koster–Cronig rates are sufficiently large to transfer all L_1 vacancies to the $L_{2,3}$ shell with essentially unit probability. Further, with the exception of Cu, the energy resolution of the measurements has been low, so the L_2 x rays and L_3 x rays have not been distinguished from each other.

We make our comparisons again in terms of the reduced parameters $u^2\sigma_I/z_1^2$ vs $E/\lambda u$. Figure 2.5 shows the data from a number of elements. The behavior here is similar to that of the K-shell data. The BEA curve is identical to that in Fig. 2.3, but multiplied by the ratio $N_L/N_K=4$ (the number of equivalent electrons in the total L shell to the number of equivalent electrons in the K shell). [Because of uncertainties in target self-absorption for lower energy photons (Swift, 1972), the data of Jopson, Mark, and Swift (1962) are used only for target Z values ≥ 64.] In Fig. 2.6 we present the existing data for the Cu L_3 subshell. Here the data of Khan *et al.* (1964a, 1966) have been aug-

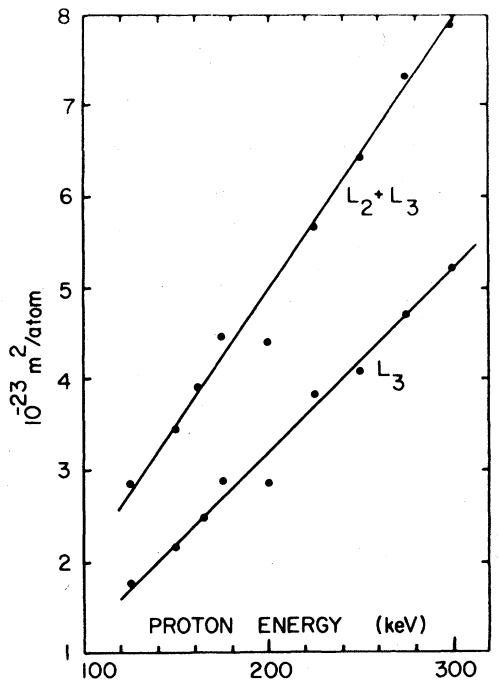

FIG. 2.7. Cross sections determined from Auger-electron measurements for the production of L-shell vacancies in Ar, plotted as a function of incident proton energy. The upper curve is for the sum of the cross sections for producing L_2 and L_3 vacancies. [After Volz and Rudd (1970)].

mented by the data of Shima *et al.* (1971) appropriately scaled down in accordance with the discussion of Khan *et al.* (1966).

It may be fortuitous that the agreement between theory and experiment is as good as it is. The theoretical energy dependence of the total cross section depends, if only weakly, on the electronic velocity distribution, which is not the same for s states as for p states. While it is true that in a hydrogenic model the velocity distribution, averaged over all angular momenta for a given principal quantum number, is identical in form to that for the $1s$ state, this is not so for an individual subshell.

The reader is referred to Khandelwal and Merzbacher (1966) and Choi and Merzbacher (1969) for detailed Born approximation calculations for individual L-subshell cross sections. Similar comparisons with binary encounter estimates could be obtained by using velocity distributions appropriate to those subshells. It is nevertheless fortunate that the scaling parameters used group the data as well as they do. This provides a framework within which to cast future comparisons.

M-shell measurements. The available M-shell data are also summarized in the Table in Appendix 1. The energy range is however quite limited, and knowledge of M-shell fluorescence yields is very meager and unsatisfactory; it is not feasible at this time to do meaningful comparisons of these data with theoretical models. The comment concerning the data of Jopson *et al.* (1962) made above in the L shell part of this section should be noted in this context.

2.3.2 Total Auger-Electron Cross Sections

While x rays constitute the most investigated of the possible decay modes, for low-Z targets this branch is by far the least probable. The emission of an Auger electron subsequent to K-shell vacancy production is more probable for all target Z values less than about 30, and several orders of magnitude more probable for $Z \leq 15$ [see Walters and Bhalla (1971)]. For higher shells, the range of Z over which Auger emission predominates becomes even larger.

Electron data specific to inner-shell cross sections are obtained by direct numerical integration of measured angular and energy distributions, for electrons emitted from a gas target. The numerical integration is made necessary by a strong electron background produced by direct removal of a bound electron by the charged particle impact; the ejected-electron spectrum is continuous, and is peaked at zero electron energy. It decreases monotonically, but is still strong even at relatively high energies. An Auger transition produces an electron spectrum whose peak energy is given by the difference in energy between the initial state and the final state of the residual atomic system, and whose width depends on the lifetime of the inner-shell vacancy state. Thus, it is easily distinguished as a peak in an otherwise monotonic background. The angular distribution associated with Auger electrons is nearly isotropic, at least for closed, deep-lying shells. (See Sec. 2.4.1.)

Early measurements of Auger cross sections were made by Volz and Rudd (1970), for vacancy production made by 125–300 keV protons in the L_2 and L_3 subshells of argon (see Fig. 2.7). Additional total cross section measurements of this type have been reported by Toburen (1971) for the nitrogen K shell (using an N_2 gas target), and Toburen (1972) for the carbon K shell (using a CO gas target) for protons with energies between 0.3 and 1.7 MeV. Toburen reports agreement of his absolute cross section measurements and BEA to within $\pm 25\%$. Since the probability for electron emission is orders of magnitude larger than that for x ray emission for these atoms, the Auger cross section and the vacancy production cross section are essentially equal. Stolterfoht (1972) has also measured absolute cross sections for production of C, N, and O K-shell Auger electrons by incident protons with energies between 50 and 500 keV. A comparison of his results with the BEA prediction is shown in Fig. 2.8.

The absolute measurements of σ_A make possible the direct determination of the fluorescence yield appropriate to proton impact. Toburen (1972) makes such a determination for carbon, using the *thick target*

x-ray data of Khan *et al.* (1966). He obtains a mean value of $\omega_K = 0.0021$ for carbon, in the energy range investigated, showing only a weak variation with proton energy. The average value obtained in this manner agrees satisfactorily with the value 0.0024 calculated by Walters and Bhalla (1971), but is considerably higher than the value 0.00113 measured by Dick and Lucas (1970). No definitive conclusions can be drawn from this because: (a) the x-ray production cross sections involved thick solid carbon; (b) the Auger measurements were for gaseous CO; and (c) the theoretical calculation was for a neutral ground state carbon atom with one K-shell vacancy. One may argue, however, that since σ_A is essentially equal to the vacancy production cross section in this case, it will depend only weakly on the chemical state. Then the experimentally determined fluorescence yield is, in principle, an accurate measure of that for solid carbon, for proton impact excitation. Measurements at lower proton energies of both x-ray and Auger cross sections would be useful in resolving questions concerning possible energy dependence of the fluorescence yield (see Sec. 3.3.5).

2.4 Characteristic Spectra

Investigations of characteristic emission spectra (electrons or photons) resulting from the filling of an inner-shell vacancy indicate some important differences between electron, photon, light-ion, and heavy-ion excitation. Spectral measurements for light ion bombardment indicate that additional outer-shell excitation

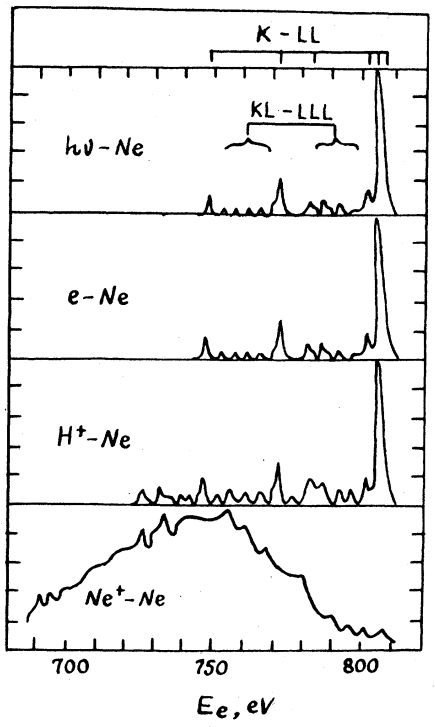

FIG. 2.9. Comparison of Ne K-shell Auger-electron spectra produced by various types of excitation: (a) 1.5-keV photons, (b) 3.2-KeV electrons, (c) 300-keV protons, and (d) 200-keV Ne^+ ions. [After Ogurtsov (1972).]

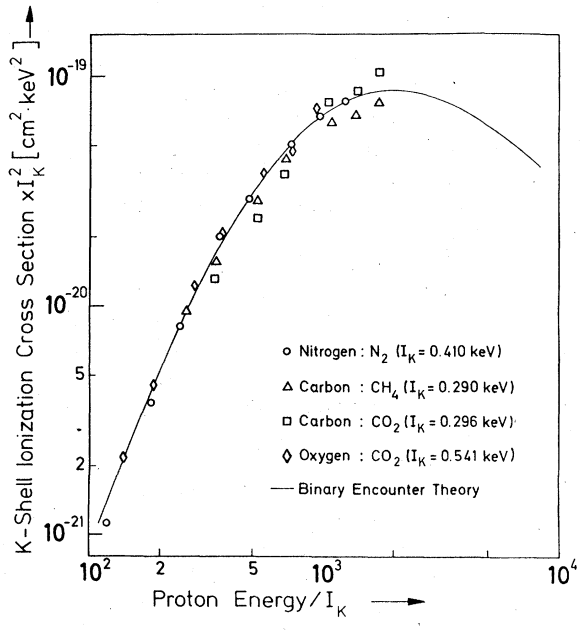

FIG. 2.8. Scaled K-shell ionization cross sections for proton impact on N_2, CO_2, and CH_4 obtained by integration of Auger electron spectra; I_K is the K-shell ionization energy. [After Stolterhoft (1972).]

is associated with the production of an inner-shell vacancy. This outer-shell excitation is distinguished from "shakeoff" which results as the atom adjusts to the inner-shell vacancy. Since these data have only recently become available, this subject has been given little theoretical attention (McGuire and Mittleman, 1972).

In the case of excitation by light ions, much more data exists for nonradiative decay, that is, for Auger and Coster-Kronig transitions. For a recent review of electron spectra from ion–atom collisions see Ogurtsov (1972). Investigations of radiative decay have only recently been of sufficiently high resolution to resolve any structure, and relatively few measurements have been made.

The selection rules for dipole radiation severely restrict the class of state which can be observed in x-ray emission studies. This makes x-ray spectra easier to interpret than Auger spectra. On the other hand, x-ray energies are much less sensitive to outer shell configurations than are Auger electron energies. This can be qualitatively appreciated by noting that in an x-ray transition, both the initial and the final orbitals are affected by the outer shell changes. Thus, in the x-ray energy, which to first order is simply the difference of the two orbital energies, there is some cancellation and the net change is small. First-order Auger electron

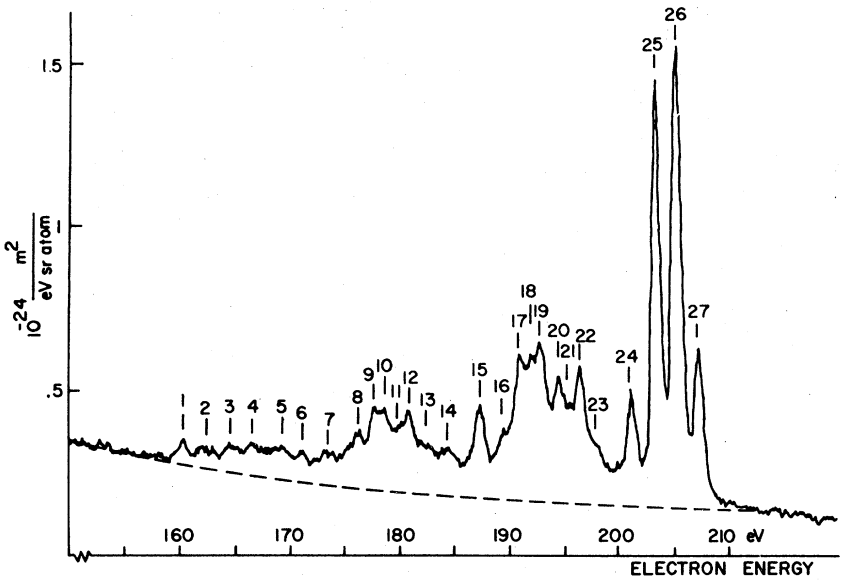

FIG. 2.10. The Ar L-shell Auger electron energy spectrum produced by 300-keV H^+–Ar collisions (from Volz and Rudd, 1970). The peaks are numbered arbitrarily for identification. The peaks numbered 9, 11, 15–17, 19, 24–27 are the "diagram" Auger transitions, designated $L_{2,3}$–MM (see Table 2.2). The analyzer resolution was 0.9 eV; for higher resolution measurements see the original paper. The dashed line represents an extrapolated background continuum.

energies, on the other hand, contain one additional orbital energy and its changes are not compensated, so that the net ejection energy changes. These changes are in opposite directions: X-ray energies increase with increasing outer shell ionization, while Auger electron energies decrease. Section 3.4.4 contains a short discussion of x-ray and Auger energy calculations within a Hartree–Fock framework.

2.4.1 Auger-Electron Spectra

Most measurements of characteristic electron spectra have been restricted to gas targets. Solid targets require ultraclean surfaces due to the short range, typically 10 Å, of Auger electrons in solids, and even with clean targets self-absorption effects can cause spectral distortion. Electron spectroscopy involves the use of a dispersive analyzer; the most commonly used are the parallel plate condensor, the 127° cylindrical analyzer, and the cylindrical electrostatic mirror. Resolutions of 0.3% are obtained under typical operating conditions; a retarding potential can also be used to improve the resolution. For detailed discussions of the experimental techniques, the reader is referred to Rudd and Jorgensen (1963), Rudd (1966), and Ogurtsov, Flaks, and Avakyan (1969c).

In Fig. 2.9 Auger-electron spectra corresponding to transitions involving an initial K-shell vacancy in neon are presented for four modes of excitation: photon, electron, proton, and neon-ion bombardment. In this section we are concerned primarily with light-ion (e.g., proton) bombardment and how the resultant electron spectra differ from, for example, those of photon and electron bombardment. In Sec. 3.4.2 we will extend our discussion to include the heavier ions.

The data in Figs. 2.9(a) and 2.9(b) are for photon and electron bombardment (Krause *et al.*, 1970). These spectra are identical to within experimental uncertainties—i.e., the energies and relative intensities of the lines are the same. The identifications of the lines are indicated in the Figures. The line labeled K–LL refer to Auger transitions where an initial vacancy is in the K shell of the neon atom, and two final vacancies remain in the L shell after the transition. The three highest energy lines of this type are the K–$L_{2,3}$, $L_{2,3}$ transitions, the next two higher energy lines are the K–L_1, $L_{2,3}$ transitions, and the lowest energy line is the K–L_1L_1 transition. In addition to these lines, two other groups of lower intensity satellite lines appear, designated as KL–LLL transitions. This indicates that two initial and three final vacancies occur in the designated shells. The initial vacancy in the L shell is created by a "shakeoff electron," emitted because of the inability of the electron cloud to relax smoothly to the sudden change in screening caused by the primary K-shell ionization. According to the shakeoff theory (sudden approximation), such multiple-electron effects should be independent of the means of primary excitation (Aberg, 1967; Krause, Carlson, and Dismukes, 1968). Indeed, the data in Figs. 2.9(a) and 2.9(b) seem consistent with this. The two groups of satellite lines can be designated as $KL_{2,3}$–$L_{2,3}L_{2,3}L_{2,3}$ for the higher energy group and $KL_{2,3}$–$L_1L_{2,3}L_{2,3}$ for the lower energy group. (The intensity of initial L_1 vacancies is small due to a faster Coster–Kronig transition.)

In Fig. 2.9(c) the spectrum for bombardment by 300-keV protons (Edwards and Rudd, 1968) is included. For protons, the same transitions occur as for electron and photon excitation and there is little change in the relative intensities of those lines; however, several additional lines appear. It is reasonable to assume that these additional excitations, which are not seen in the

TABLE 2.2. A partial list of measured transition energies and linewidths of designated Ar L Auger electrons produced by bombardment by 300-keV protons (Volz and Rudd, 1970). For comparison the transition energies for bombardment by electrons (Mehlhorn and Stalherm, 1968) are also included. The measured linewidths for bombardment by electrons (not listed) were generally 0.16±0.02 eV. The "peak number" refers to Fig. 2.10.

Final vacancy state	Peak no.	Measured energy (eV) for proton bombardment ±0.07 eV	Measured energy (eV) for electron bombardment ±0.25 eV	Linewidth eV for proton bombardment ±0.05 eV
		$L_2(^2P_{1/2})$ Initial vacancy state		
$M_1^2(^1S)$	11	179.88	179.93	0.35
$M_1M_{2,3}(^1P)$	16	189.35	189.30	0.33
(^3P)	19	192.93	192.88	...
$M_{2,3}^2(^1S)$	24.9	203.03	203.01	...
(^1D)	26.5	205.46	205.40	0.25
(^3P)	27	207.16	207.03	0.26
		$L_3(^2P_{3/2})$ Initial vacancy state		
$M_1^2(^1S)$	9	177.68	177.79	0.25
$M_1M_{2,3}(^1P)$	15	187.13	187.16	0.24
(^3P)	17	190.98	190.88	0.40
$M_{2,3}^2(^1S)$	24	200.92	200.87	0.24
(^1D)	25	203.31	203.26	0.24
(^3P)	26	205.05	204.96	0.33

electron and photon cases, are not due to shakeoff processes but are instead due to additional excitation in the neon atom produced as a result of the proton interaction.

Although specific identification of each Auger transition resulting from proton-induced K-shell vacancies in neon is difficult, some general comments can be made. Besides the normal or "diagram" transitions (K–LL) and satellite transitions (KL–LLL) which have already been discussed, two additional types of initial states are possible: First, states corresponding to the removal of additional L-shell electrons, and second, initial states in which electrons have been "promoted" into the M or other less energetic shells. In the first case (removal of additional L-shell electrons), one finds that the Auger lines are shifted to lower energies for increasing numbers of L-shell vacancies. In the second case, one finds that the effect of electron promotion is to shift the Auger transition to higher energies; this is true regardless of whether the promoted electron participates in the transition or simply acts as a "spectator." An additional type of initial state which we have not considered involves initial double inner-shell vacancies, the so-called hyper-satellites (Briand *et al.*, 1971). Although transitions corresponding to these states have not been reported for proton excitation, such transitions have been seen for heavy ion-atom collisions and will be discussed in Sec. 3.4.2.

Studies similar to those for the neon K shell have also been reported for the argon L shell (Ogurtsov, Flaks, and Avakyan, 1969b; Volz and Rudd, 1970). In Fig. 2.10 the L-shell Auger electron spectrum produced by 300-keV protons is presented. In Table 2.2 the normal ("diagram") lines from the Figure are listed along with the measured energies and line widths. For comparison, the measured energies for electron bombardment (Mehlhorn and Stalherm, 1968) are also included. In addition to the lines listed in Table 2.2, several other lines are seen for both electron and proton bombardment. A comparison of the electron and proton produced spectra for argon indicate that, as in the neon case, many more transitions are produced as a result of proton bombardment. The measured line widths presented in Table 2.2 vary from 0.24 to 0.40 eV. These values are considerably larger than the 0.16±0.02 eV widths obtained from electron bombardment. One possible cause for the increased linewidths is Doppler broadening due to target atom recoil (see Sec. 3.4.2).

In addition to the L-shell Auger electron spectrum, Ogurtsov, Flaks, and Avakyan (1969b) have also studied the L-shell Coster–Kronig spectra; the results of their measurements are presented in Fig. 2.11. The normal Coster–Kronig transitions, designated L_1–$L_{2,3}M_{2,3}$ are indicated in the Figure. The additional peaks in the energy range 35–38 eV are satellites, corresponding to initial vacancies with L_1M designations. The additional peaks in the energy range 52–55 eV involve transitions from atoms in which an electron has been removed from the L_1 shell but has remained bound to the atom.

Angular distributions of Auger electrons and x rays are usually assumed to be isotropic. Melhorn (1968)

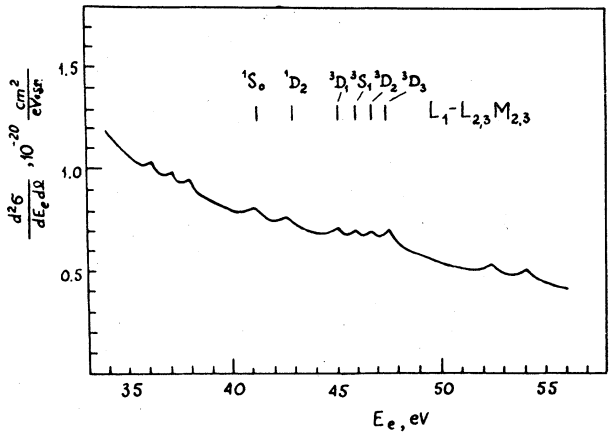

FIG. 2.11. Argon L-shell Coster-Kronig transitions produced in 20-keV H^+–Ar collisions. The energies of the normal transitions, designated $L_1-L_{2,3}M_{2,3}$ are indcated in the figure. The additional transitions are described in the text. The resolution was 0.3 eV. [After Ogurtsov (1972).]

has shown, however, that inner-shell ionization of an electron with quantum numbers n, $l>0$, $j>1/2$ can have a nonisotropic angular distribution. Cleff and Melhorn (1971) have observed this nonisotropic behavior for the $L_3M_{2,3}M_{2,3}(^1S_0)$ Auger transition for electron excitation in argon. Volz and Rudd (1970) have measured angular distributions for four different Auger electron peaks (numbers 15, 24, 25, and 27 in Fig. 2.10) for proton excitation, and the results of the measurements are presented in Fig. 2.12. The four transitions exhibit no significant deviations from isotropy. The cross section for producing continuum

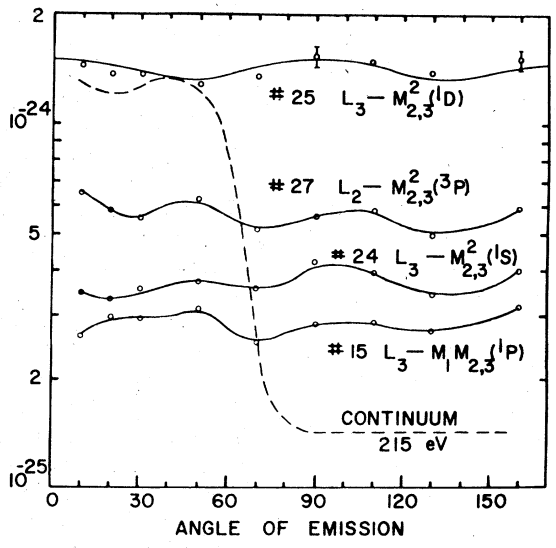

FIG. 2.12. Angular distribution of electrons from 300-keV H^+–Ar collisions for four Auger transitions and for continuum electrons at 215 eV. [After Volz and Rudd (1970).]

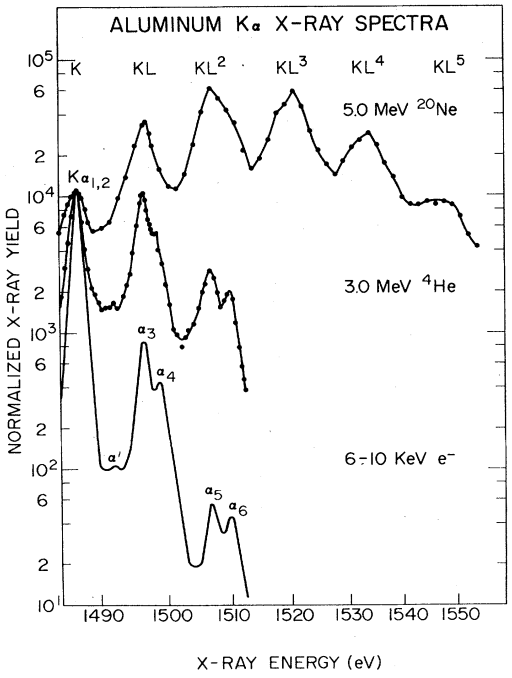

FIG. 2.13. Aluminum K_α x-ray spectra excited by 5.0-MeV Ne ions and 3.0-MeV He ions (Knudson, Burkhalter, and Nagel, 1972). Also included is the spectrum excited by electrons in the energy range 6–10 keV (Fisher and Baun, 1965). All spectra have been normalized to the same peak intensity for the $K_{\alpha 1,2}$ line. The initial vacancy configurations giving rise to the observed satellite groups are indicated at the top of the figure. [After Knudson, Burkhalter, and Nagel (1972).]

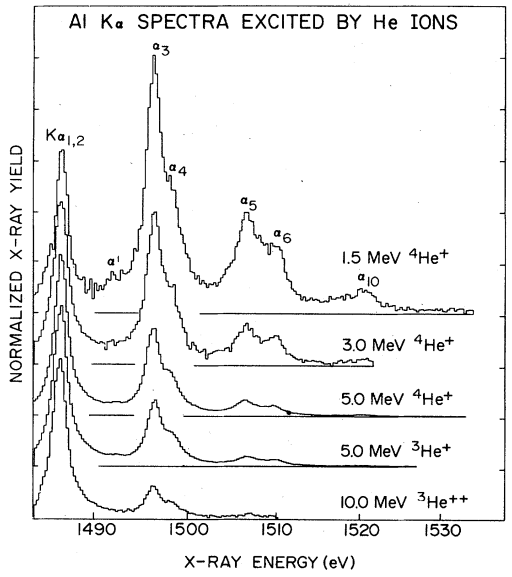

FIG. 2.14. Aluminum K_α spectra excited by He ions. All spectra are normalized to the same height at the $K_{\alpha 1,2}$ line. The base line for each spectrum is displaced by a constant amount for clarity. [After Knudson, Burkhalter, and Nagel (1972).]

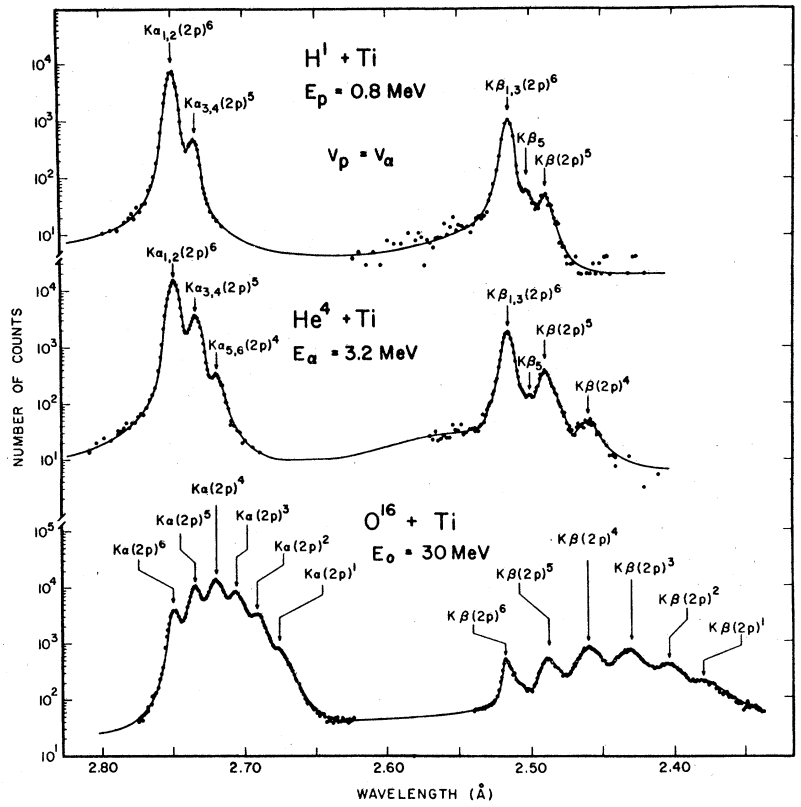

FIG. 2.15. Spectra of K-x rays from thick Ti targets bombarded by protons, alpha particles, and O ions. [After Richard (1972).]

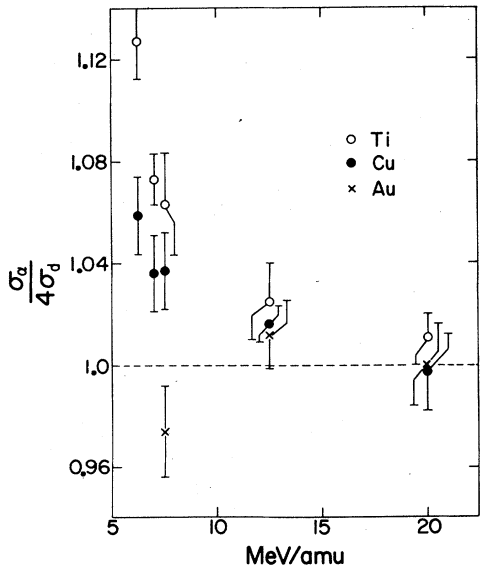

FIG. 2.16. Comparison of alpha-particle and deuteron cross sections at equal velocities (after Lewis, Natowitz, and Watson, 1971). The Ti and Cu data are for K shells, and the Au points are for L shells. The dashed line shows Born and binary encounter prediction.

electrons at 215 eV was also measured; a sharp drop is observed at angles above 90°. Similar measurements have also been reported by Cacak and Jorgensen (1970). Stolterfoht (1972) has measured the angular distribution for K-shell electrons and, as is expected, no deviation from isotropy was found.

2.4.2 X-Ray Spectra

Most measurements of x-ray spectra produced by light ion bombardment (protons, alpha particles, etc.) have indicated no differences between these spectra and spectra produced by electrons or photons (see, for example, Watson and Li, 1971). However, most of these measurements involved the use of solid state detectors with moderate energy resolution.

Recent measurements (Knudson, Burkhalter, and Nagel, 1972; Richard, 1972) using high resolution crystal spectrometers have indicated considerable enhancement of multiple-vacancy phenomena in the x-ray spectra produced by light-ion bombardment. In Fig. 2.13, three aluminum K_α x-ray spectra obtained by electron bombardment, helium-ion bombardment, and neon-ion bombardment are presented (Knudson, Burkhalter, and Nagel, 1972). The normal x-ray

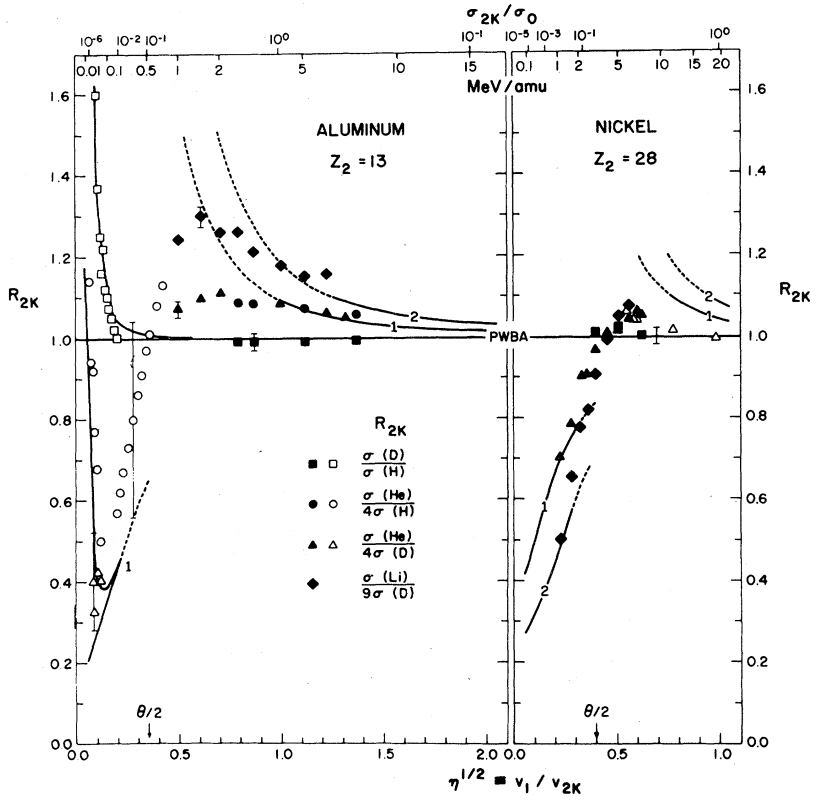

FIG. 2.17. Illustration of projectile charge dependence effects taken from Basbas *et al.* (1971). The vertical scale represents K-shell ionization cross section *ratios* for Al and Ni for the different projectile pairs indicated in the legend. The lower horizontal scale represents the ratio of ion velocity to the K electron velocity and the upper horizontal scale gives the particle kinetic energy in MeV/amu and a nomograph of the ionization cross section, where σ_0 equals 27 kb and 1.2 kb, respectively, for the Al and Ni targets. Copper data from Lewis, Natowitz, and Watson (1971) are shown on the Ni plot as open triangles. The curves shown depict theoretical Z_1 dependences discussed by Basbas *et al.*

satellite designations are indicated on the electron-produced spectrum, and thus the satellite group designated α', α_3, and α_4 corresponds to transitions where an initial vacancy exists in both the K and L shells. It is clear from the figure that the probability of simultaneous K- and L-shell vacancies greatly increases as one goes from electrons to helium ions and finally to neon ions. (We defer discussion of data for heavier ions such as Ne^+ until Sec. 3.4.3.)

In Fig. 2.14 we show x-ray spectra produced by helium-ion bombardment for a variety of ion energies (Knudson, Burkhalter, and Nagel, 1972). The data indicate that the intensities of the satellite groups decrease as the ion energy increases. This is consistent with a decreasing cross section for L-shell vacancy production ($E/\lambda u \approx 2.5$ for 1.5-MeV alpha particles). In particular, the $K_{\alpha'\alpha_3\alpha_4}$ satellite group decreases from 220% of the $K_{\alpha_{1,2}}$ intensity to 30% as one goes from 1.5-MeV ^{4}He ions to 10-MeV ^{3}He ions. Knudson, Burkhalter, and Nagel (1972) also report similar studies with protons; in this case the intensity ratio varies from 26% at 0.75 MeV to 14% at 5.0 MeV.

In Fig. 2.15, three titanium K_α, K_β x-ray spectra obtained by proton, alpha-particle, and oxygen-ion bombardment are presented (Richard, 1972). Indicated in the Figure are the number of $2p$ electrons remaining in the atom at the time of x-ray emission From a comparison of the proton and alpha-particle data, which were taken at the same velocity, we see that heavier projectiles produce a greater abundance of simultaneous $2p$ vacancies. (The data for heavier ions such as oxygen are discussed in Sec. 3.4.3.)

2.5 Extensions and Deviations

The proton and alpha-particle data show that while the gross structure of inner-shell vacancy production is understood, there are areas in which both experimental and theoretical efforts are required. One involves the systematic investigation of high Z ($Z > 50$) elements at moderate projectile energies to determine the effects associated with relativistic bound electrons. Another is the use of high-energy projectiles, where relativistic effects are associated with the projectile. Some attempt has been made (Jamnik and Zupancic, 1957; Choi, 1971) at a theoretical formulation of the effects of special relativity associated with the bound electron. To our knowledge, no such efforts are available for relativistic heavy projectiles.

Perhaps more interesting is the projectile charge dependence of the total cross section. The depression of the cross section at low energies for small Z targets has already been discussed. In addition, we observe that

in the vicinity of the peak of the total cross section, $E/\lambda u \sim 1$, the proton data tend to lie on or below the theoretical curves, while the alpha-particle data lie above. In Sec. 3.3.2 we will discuss x-ray production by 7–40 MeV oxygen ions. There (see Fig. 3.26) we will see that, if those projectiles can be considered as point charged particles for K-shell vacancy production purposes, these trends are continued and accentuated. Those cross sections rise by a factor of about 2 above the predicted values at the peak, and also show marked decreases at lower $E/\lambda u$. A theoretical understanding of both the increase and the depression of the cross section should emerge from an appropriate reformulation of the problem.

Direct comparisons of this z_1-dependent effect for various light ions have been made by Basbas *et al.* (1971) and Lewis, Natowitz, and Watson (1971, 1972). These authors compare directly the ratios of cross sections at the same velocity, which can be more precisely determined than individual cross sections. Figure 2.16 shows such a comparison for protons and alpha particles. These data indicate that these effects vanish for very high energy, and increase the cross section for increasing z_1 at energies near the peak. The comparison by Basbas *et al.* is reproduced in Fig. 2.17.

Further work is also required in the measurement of Auger cross sections. As we saw in Sec. 2.3.2 the Auger total cross section measurements permitted a determination of the fluorescence yield for carbon. We will see in Sec. 3 that this becomes an extremely important problem for heavier projectiles; its role for the light ions has not been assessed. It is quite possible, in fact, that some of the observed z_1-dependence of the total cross sections is due to changes in fluorescence yield (see McGuire and Mittleman, 1972). These changes would arise from excitation of the shells from which the vacancies are filled, simultaneous with vacancy production in the inner shell being investigated. One additional method, therefore, of investigating this question, is a careful determination of the strength and nature of the satellites in x-ray and Auger electron spectra.

A related question which has not been examined is the solid vs gas target difference in the mode of filling of the produced vacancy. Most fluorescence yield calculations are based on ground state neutral atom configurations, whereas most applications of these results are for solid-state targets. For K shells of high-Z targets, this effect is expected to be small; for low-Z targets, however, some differences are expected.

Another area in which rapid progress can be expected is in comparisons with differential cross section measurements. Preliminary measurements of this type of the impact parameter dependence of inner shell excitation by protons have been reported (Laegsgaard, Feldmann, and Andersen, 1971) and are in qualitative agreement with the calculations of Bang and Hansteen (1959) and Hansteen and Mosebekk (1970).

3. HEAVIER IONS

3.1 Theoretical Models

3.1.1 Introduction

We have seen from Sec. 2 that even for protons and alpha particles, direct interaction models become increasingly less satisfactory for lighter targets and at lower energies. The physical phenomena associated with these deviations acquire the dominant role for heavier ions, and the simpler models cease to be relevant at low velocities. This section is devoted to establishing a framework for discussion of the production of inner-shell vacancies in *heavier* ion–atom collisions. Qualitative criteria are developed for guiding our interpretation of the observed events. While such a presentation is no substitute for the much needed rigorous theoretical developments, it does serve to provide a basis for classification of a wide variety of phenomena.

3.1.2 General Considerations

The Hamiltonian for an atom–atom system is

$$H=T_{\mathrm{A}}+T_{\mathrm{B}}+T_e+V_{\mathrm{A},e}+V_{\mathrm{B},e}+V_{\mathrm{A,B}}+V_{e,e}, \quad (3.1)$$

where the T's are kinetic energies, the subscripts A, B, and e refer to nuclei A and B, and all electrons, respectively, and the V's are sums of Coulomb interactions. In a time-dependent description, the wave function, in the center of mass (CM) frame, at a time such that the approaching atoms are still separated by a distance R_I very large compared to atomic dimensions, might be written as[1]

$$\Psi(t_0)=\mathfrak{A}\{\exp(i\mathbf{k}\cdot\mathbf{r}_{\mathrm{A}})\phi_\alpha(\mathbf{r}_{i\mathrm{A}}) \times\exp(-i\mathbf{k}\cdot\mathbf{r}_{\mathrm{B}})\phi_\beta(r_{j\mathrm{B}})\}G_\Delta(\mathbf{R}-\mathbf{R}_I), \quad (3.2)$$

where $\hbar\mathbf{k}=\mu\mathbf{v}_0$ is the CM momentum of atom A, μ is the reduced mass, α and β are sets of quantum numbers specifying the initial states of atoms A and B, and ϕ_α and ϕ_β are the corresponding antisymmetrized wave functions for the electrons. Here $r_{i\mathrm{A}}$ symbolizes the positions of all electrons initially on atom A relative to that nucleus, and similarly for $r_{j\mathrm{B}}$. The symbol $\mathfrak{A}$ to the left of the bracket is the antisymmetrization operator, indicating that the expression in the brackets must be properly antisymmetrized. [We are here neglecting mass polarization effects, relativistic corrections, etc., as they are not germane to our immediate development. We will also presume that Eq. (3.2) also correctly describes an ion–atom initial state even though in that case changes in form would be expected because of the long range nature of the Coulomb force. Such

[1] In this theoretical section nuclear coordinates are represented by an upper-case R, in order to distinguish them from electronic coordinates. In subsequent sections we follow the convention dominant in the experimental literature, and represent internuclear distances with a lower-case r.

omissions and changes, although they might be important, would not qualitatively change our subsequent discussion.] The functions ϕ_α, ϕ_β are appropriate solutions of

$$H_A\phi_\alpha=(T_{ei}+V_{A,ei}+V_{ei,ei})\phi_\alpha=E_\alpha\phi_\alpha,$$

and

$$H_B\phi_\beta=(T_{ej}+V_{B,ej}+V_{ej,ej})\phi_\beta=E_\beta\phi_\beta, \quad (3.3)$$

and

$$H=T_A+H_A+T_B+H_B+V_{ei,ej}+V_{A,B}.$$

The factor $G_\Delta(\mathbf{R}-\mathbf{R}_I)$ describes a wave packet for $\mathbf{R}=\mathbf{r}_A-\mathbf{r}_B$ centered at position $\mathbf{R}_I$ having an initial width Δ which is large compared to the de Broglie wavelength of relative motion, $L=1/k=\hbar/\mu v_0$. For incident energies of interest here, L will be small compared to atomic dimensions.

The wave function for the system will develop in time from its initial form Eq. (3.2) according to the Schroedinger equation $H\Psi=i\hbar\dot{\Psi}$, and the center of the wave packet G will move inward, initially with velocity $\mathbf{v}_0$, without spreading appreciably since it is broad compared to L. Eventually the center of this wave packet will reach a radial distance R_0, the distance of closest approach, and begin to recede again, there being several possible angles of emergence of the broadened wave packets depending on the number and kind of energetically possible reactions which can occur. These packets then move to larger and larger distances at velocities appropriate to the conservation of energy and momentum separately for each possibility. The electronic wave functions, which were initially described by atomic functions centered on the atoms and thus moved with an average velocity described by the incident packet, continue with the above packet after R_0 is reached, but separate waves (corresponding to "shakeoff") will also be formed in the vicinity of R_0. In addition, the receding packets of electron waves may develop some spreading waves from the centers of these moving packets (corresponding to Auger processes) and there will be changes in the shapes of packets as they recede.

We are concerned here with inner-shell excitations. These excitations involve transfers of energy $\Delta E\gtrsim 100$ eV, necessitating collisions of electrons and Coulomb particles with distances $d\lesssim(z_1e^2/\Delta E)\sim\frac{1}{8}z_1\times10^{-8}$ cm. Until the wave functions of the electrons on atoms A and B overlap sufficiently, the probability of such a transfer will be negligible. Thus we can define a collision time t_c in the usual way, $t_c\simeq a/v_0$, where a is some dimension associated with the inner shell in question.

We see from the form of the initial wave packet Eq. (3.2) that various existing approaches might be applicable in different energy ranges. For example, if the relative velocity $\hbar k/\mu$ remains large throughout the collision, the effects of the over-all antisymmetrization will be small. In electron–atom collisions, the "exchange" terms resulting from antisymmetrization can be shown to be rapidly decreasing functions as the incident momentum becomes large compared to the average bound electron momentum. Similar considerations will apply here. Thus, in momentum space, the electronic wave functions associated with atom A will have as their origin the momentum $(m_e/\mu)\hbar\mathbf{k}$, and those associated with atom B will be centered at $-(m/\mu)\hbar\mathbf{k}$. If $|(m_e/\mu)\hbar\mathbf{k}|$ is always much larger than the bound state average value for each and every electron state involved, antisymmetrization will produce only small exchange terms. Of course, for head-on collisions, $\hbar k$ approaches 0, and the above argument breaks down, but only for a very small range of impact parameters. These must be examined separately.

Many of the collisions maintaining large nuclear momenta throughout may still involve substantial electronic overlap in position space. Within a classical framework, at the distance of closest approach the momentum is smallest. If we ask for the distances of closest approach for which the nuclear velocity is greater than the average velocity of the *tightest* bound electron, we obtain (at high energies and small impact parameters, the Coulomb repulsion between the nuclei suffices to provide an estimate)

$$R_0\gtrsim\frac{Z_AZ_Be^2}{E-\lambda u_K}=\frac{Z_AZ_Be^2}{E}\Big/\left(1-\frac{\lambda u_K}{E}\right), \quad (3.4)$$

where $E=\mu v_0^2/2$ and $\lambda=\mu/m_e$. Here u_K is the binding energy of the K-shell electrons on the larger atom. Approximating u_K by $Z_A^2e^2/2a_0$, where a_0 is the Bohr radius, we have

$$R_0\gtrsim 2a_0(Z_B/\lambda Z_A)/(E/\lambda u_K-1). \quad (3.5)$$

Thus, if $E/\lambda u_K\geq(1+2Z_B/\lambda)$, the "equal velocity" distance of closest approach will be smaller than the average K-shell radius. For $Z_A=Z_B=18$ and $\lambda=4\times10^4$ the center of mass energy required is about 120 MeV.

Thus, for $E/\lambda u_K<1$, *all* collisions are such that the momentum space electronic wave functions may have strong overlaps and attention must be given to the effects of the exclusion principle. For slow collisions, $E/\lambda u_K\equiv(v_0/v_K)^2\ll1$, the K-shell electrons on one atom can adjust adiabatically to the second force center (whose position is then a slowly varying function of time).

Using the K shell in this discussion provides a limit which is not appropriate for all energy levels in the atoms. When we consider the least bound energy levels, the above suggests that we examine $E/\lambda u_I$, where u_I is the first ionization energy of the atom. If $E/\lambda u_I<1$, then all electrons may adjust adiabatically and molecular considerations are appropriate. For $Z_A=Z_B=18$, the corresponding energy is about 500 keV.

These rough qualitative arguments suggest the following division: For $E<\lambda u_I$, the collision may be amenable to being viewed as a slowly time-varying molecule. For $\lambda u_I<E<\lambda u_K$, only partial relaxation is

expected and complications may arise in a molecular description, but such a framework probably still provides the most reasonable basis for understanding inner-shell results. On the other hand, for $E>\lambda u_K$, almost all initial conditions lead to collisions in which antisymmetrization is unimportant and a Born-type description provides the best simple framework for understanding the attendant events. There remains, however, even in this limit, a range of small impact parameters where exchange effects may be important. Such nearly head-on collisions may produce effects, such as enhanced multiple-vacancy production and inner-shell charge exchange, which are qualitatively different from those given in a Born description.

3.1.3 High Energy Limit

The Born description being discussed here should be specified to avoid ambiguity. Here we mean that the initial and final states be specified as in the curly brackets in Eq. (3.2), without overall antisymmetrization. This results in a probability for producing the final atomic states $\phi_{\alpha'}$, $\phi_{\beta'}$ given, for example, by Bates (1962)

$$\omega_{\mathrm{fi}}=(2\pi/\hbar)\mid\langle\Psi_f\mid V_I\mid\Psi_i\rangle\mid^2\rho(E), \qquad (3.6)$$

where $V_I=H-T_{\mathrm{A}}-H_{\mathrm{A}}-T_{\mathrm{B}}-H_{\mathrm{B}}$, $\rho(E)$ is the density of final states, and

$$\Psi_f=\exp(i\mathbf{k}'\cdot\mathbf{r}_{\mathrm{A}})\phi_{\alpha'}(\mathbf{r}_{i\alpha})\exp(-i\mathbf{k}'\cdot\mathbf{r}_{\mathrm{B}})\phi_{\beta'}(\mathbf{r}_{j\mathrm{B}}),$$

$$\Psi_i=\exp(i\mathbf{k}\cdot\mathbf{r}_{\mathrm{A}})\phi_{\alpha}(\mathbf{r}_{i\mathrm{A}})\exp(-i\mathbf{k}\cdot\mathbf{r}_{\mathrm{B}})\phi_{\beta}(\mathbf{r}_{j\mathrm{B}}). \quad (3.7)$$

This differs from the Born description for point charged particle inner-shell vacancy production in several ways. Here V_I contains, in addition to the nucleus–electron interactions, electron–electron interactions. Furthermore, there will occur energy-dependent overlap integrals multiplying the one-particle matrix elements for excitation of a given electronic orbital. Calculations of this type have been carried out for small systems only (Bates, 1962), and primarily for outer-shell excitations. Because of the paucity of Born calculations specifically for inner-shell excitation, we will not discuss this topic further, but turn instead to the low-energy limit, which also coincides with the majority of the available experimental data.

3.1.4 The Quasiadiabatic Approach

For slow collisions, R is a slowly varying function of time. It thus is appropriate to break up the Hamiltonian (3.1) into $H_{\mathrm{nuc}}=T_{\mathrm{A}}+T_{\mathrm{B}}$, and $H_e=H-H_{\mathrm{nuc}}$, and obtain solutions within the framework of the Born–Oppenheimer (B–O) approximation, in which the wave function Ψ for the system is a product of nuclear and electronic parts, i.e.,

$$\Psi=\chi_N(\mathbf{R})\Psi_e(\mathbf{r},\mathbf{R}), \qquad (3.8)$$

where r represents electronic coordinates. If R were considered completely fixed, the electronic part Ψ_e would obey the equation

$$H_e\Psi_e(\mathbf{r},\mathbf{R})=E_e(R)\Psi_e(\mathbf{r},\mathbf{R}). \qquad (3.9)$$

The B–O approximation consists of using the Ψ_e from Eq. (3.9) in Eq. (3.8), χ_N being determined by

$$[H_{\mathrm{nuc}}+E_e(R)]\chi_N(R)=i\hbar(\partial\chi_N/\partial t). \qquad (3.10)$$

The action of H_{nuc} on $\Psi_e(\mathbf{r},\mathbf{R})$ has been neglected. This treatment, called the perturbed stationary state or quasiadiabatic method, has been widely used in ion–atom collisions involving outer-shell excitation (see, for example, Mott and Massey, 1966). The stationary states defined by Eq. (3.9) are then considered to be perturbed by H_{nuc}, causing electronic transitions.

Let us first consider the symmetric case, i.e., the homonuclear diatomic molecule case, for Eq. (3.9). The presence of two force centers for the electrons implies that each atomic state for the isolated atom will give rise to two molecular states, one symmetric and the other antisymmetric with respect to inversion of electronic coordinates through the center of charge. These are labeled even (g) and odd (u), respectively, and for K shells at least the energy of the u state lies higher than that of the g state for all values of the internuclear separation (except $R=\infty$, where they are of course degenerate). The molecular orbitals corresponding to these states can be classified by their parity and angular momentum projection on the internuclear axis, as well as by other quantum numbers which are less important in the present context.

Within the B–O approximation, each orbital of the ion–atom system has an energy associated with it which will vary as a function of internuclear separation. It may happen that the energies of two such orbitals having the same symmetries will approach each other at some internuclear separation R_x. When two adiabatic levels having the same symmetry approach each other, they repel. This leads to the concept of "avoided crossings" and to sharp bends in the orbital energies as functions of internuclear separation. Fano and Lichten (1965) and Lichten (1967) have proposed, however, that a better understanding of collisions involving inner-shell vacancies is obtained by defining a set of states which run smoothly through the crossings. Such states, which Lichten terms "diabatic," can be well defined in terms of hydrogenic one-electron orbitals at all values of internuclear separation. The use of such states precludes inclusion of configuration interaction [see Lichten (1967)]; nevertheless, this picture is a very valuable one for semiquantitative arguments.

At these crossings there is a probability that an electron occupying the original level will make a transition—i.e., be promoted—to the other level, if it is not fully occupied. This transition probability, considered as a function of internuclear separation, will be highly peaked at the "crossing radius" R_x, because there the

true energy difference reaches its smallest value. The probability is governed by the interactions coupling the two levels. The strongest coupling arises from nuclear motion, both radial and rotational, with much weaker couplings being due to fine structure splittings and configuration interaction. The selection rules for the radial motion coupling are $\Delta m_l = 0$ and no change in parity, where m_l denotes the projection of the orbital's angular momentum onto the nuclear axis. The molecular axis also rotates during the collision, and this nuclear motion effect produces transitions with selection rules $\Delta m_l = \pm 1$ and no change in parity of the molecular orbital.

In this model, as the collision partners approach each other, the various atomic states go over adiabatically into the corresponding molecular states, and some atomic levels may "split" into two or more molecular levels. The time sequence of the collision can then be traced along the curves of orbital energies as functions of R because the nuclei can be considered to be fairly well localized. The point representing the actual energy for a given electronic orbital will move in from $R = \infty$, reach a distance of closest approach R_0, and then recede. For those filled orbitals which have no crossings, or which cross only with other filled orbitals, the electrons involved will simply adiabatically adjust, and finally return to the states they were in initially, as the nuclei recede. On the other hand, for those initially filled orbitals which cross at a separation R_x with an unfilled orbital, the model predicts a finite probability for the electrons in question to make the transition to the unfilled orbital, thus leaving a vacancy in the initial orbital as the two atoms recede, for $R_0 < R_x$. Again, if $R_0 > R_x$, the crossing is not reached by the representative system point and the transition probability will be quite small. The detailed motion of the "representative" point is found from Eq. (3.10).

In order to make use of the above picture, knowledge of the orbital energies as functions of internuclear separation is required. These can be obtained by direct calculation (Slater, 1963). The most convenient display is given in terms of the orbital energies with the nuclear repulsion, $V_{AB} = Z_A Z_B e^2/R$, removed. The resultant plots of the molecular orbital energy levels (MO's), for all orbitals, versus internuclear separation are called correlation diagrams. In such a plot, the values at $R = 0$ correspond to the united atom electronic energies, and the values at very large R are the separated atom energies, i.e., the binding energies of the electrons in the atoms with $Z = Z_A + Z_B$ and $Z = Z_A$ or Z_B, respectively.

The rules that govern which orbitals in the separated atoms go over into a given orbital in the united atom at $R = 0$ can be deduced even without explicit calculation by considering the effects of the electric field produced by the presence of one atom on the orbital energies of the other atom, and observing the quantum numbers which are conserved. In the homonuclear case, aside from spin considerations, these are the projection of orbital angular momentum on the internuclear axis (labeled σ, π, δ, etc.) and parity with respect to the center of charge. An additional consideration is introduced by the approximate two center symmetry of the Hamiltonian. The results can be summarized by the following rules: Separated atom states with a given orbital angular momentum projection connect in a correlation diagram with united atom states having the same projection, and the same number of radial nodes [i.e. equal $(n-l-1)$]. In this correlation, the states are to be connected sequentially, starting with the lowest in energy. Thus, in the homonuclear case, the four $1s$ electrons in the separated atoms will go into the $1s$ and $2p$, $m=0$ united atom states via $1s\sigma_g$ and $2p\sigma_u$ molecular orbitals, respectively. (Molecular orbitals are labeled with the n and m_l of the united atom states and the orbital angular momentum projection.) Similarly, the $2s$ electrons go to $2s$ and $3p$, $m=0$ united atom states via $2s\sigma_g$ and $3p\sigma_u$ molecular orbitals. This is illustrated for the Ar–Ar collision in Fig. 3.1, taken from Fano and Lichten (1965).

In heteronuclear collisions, inversion symmetry is no longer applicable, but the above rules still produce the correct correlation between separated atom states and united atom states (Barat and Lichten, 1972). Unlike the homonuclear case, where every pair of atoms independent of Z has the same correlations, the hetero-

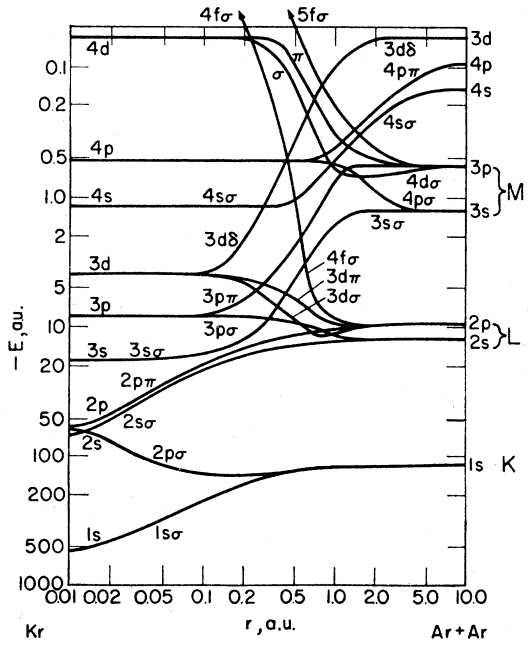

FIG. 3.1. Molecular-level diagram for the Ar–Ar system, as presented by Fano and Lichten (1965). The energies for large internuclear distance r are the atomic levels of Ar and for small r the energy levels are the atomic levels of the combined atom, Kr.

nuclear case correlations depend on the atoms involved. This is because the sequential ordering of states with a given number of radial nodes in the separated atom limit now depends on the relative binding energies of the atoms involved. Specific examples, relevant to later discussions, are represented in Fig. 3.2.

It should be noted that certain of the diabatic orbital energies shown, such as the $4f\sigma$ level in Figs. 3.1 and 3.2(c) and (d), exhibit very rapid increases in a small range of values of internuclear separation. Even when the criteria discussed in Sec. 3.1.2 for the separated atom binding energies are met, such rapidly changing levels cannot generally be considered quasiadiabatic. Electrons initially in such orbitals may not be able to adjust adiabatically, because the orbital energy undergoes large changes in times which are short compared to the initial electronic periods, i.e. to the "relaxation" time. That is, such orbitals can exhibit strong nonadiabatic mixing with many orbitals at those distances of closest approach corresponding to the rapid rise. (See Secs. 3.2.3 and 3.3.4.)

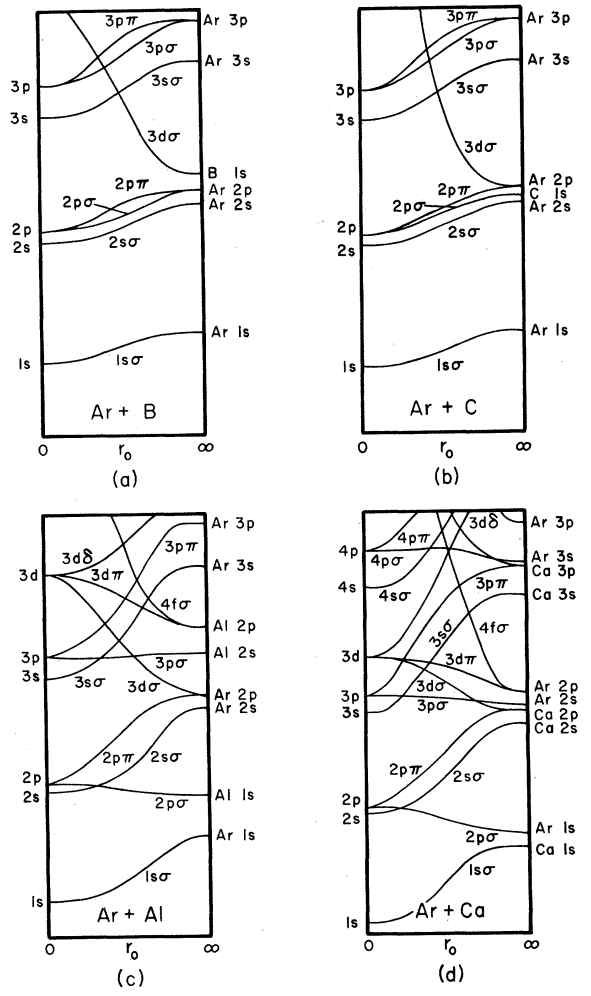

FIG. 3.2. Molecular-level diagrams for asymmetric (heteronuclear) collisions of Ar with several different collision partners. As in Fig. 3.1, the horizontal scale represents internuclear distance.

3.1.5 Other Theoretical Developments

3.1.5(a) Adiabatic Calculations

The orbital energies as functions of internuclear separation have been calculated *ab initio* on the assumption of full adiabaticity for the Ne–Ne system (Thulstrup and Johansen, 1971) and the Ar–Ar and Ne–Ar systems (Larkins, 1972). Both of these investigators used the Hartree–Fock molecular orbital method. While yet other systems have been studied using Hartree–Fock techniques, these are the only examples known to us where the calculations have been carried to sufficiently small internuclear separations specifically for looking at inner-shell excitations. These explicit calculations are in agreement with the qualitative descriptions of correlation diagrams given above, except that crossings are avoided.

3.1.5(b) Diabatic Representations

The above description of the collision in terms of the diabatic one-electron orbitals indicates that such orbitals sometimes provide a better starting point for the collision problem than would a full adiabatic treatment which includes configuration interaction in the starting basis set. In the diabatic description, states which would have "avoided crossings" now have true crossings which can be identified with electron promoting transitions in a straightforward fashion. Smith (1969) discusses a formulation of the problem wherein this desirable feature would be incorporated directly into the definition of the basis states.

The adiabatic representation is defined by diagonalizing the electronic energy. When this is done, the off-diagonal terms in the *radial* momentum matrix become large in the vicinity of an avoided crossing—these are in fact the terms used to describe the transition probability. Smith suggests that we define the diabatic states as those which diagonalize the radial momentum matrix. If this is done, the electronic energy matrix will no longer be diagonal, and its off-diagonal terms will now provide the coupling between states in a transition. This scheme transfers the burden of coupling from the momentum operator to the electronic energy operator. In some situations, particularly those collisions which lead to nonadiabatic behavior, this may be a substantial advantage.

Sidis and Lefebvre–Brion (1971) have carried out an *ab initio* calculation of the He^+–Ne system based on Smith's definition of diabatic states. They too used Hartree–Fock techniques to obtain the orbital energies, and succeeded in diagonalizing the radial momentum matrix by appropriate choice of states to be considered.

They then used these orbital energies in the Landau–Zener approximation (described below) to obtain differential cross sections for inelastic scattering.

3.1.5(c) *Rotational Coupling*

As we will see below, most K-shell vacancy production involves coupling of the $2p\sigma$–$2p\pi$ molecular orbitals at very small internuclear distances. This coupling is provided, in a diabatic model, primarily by the angular part of the nuclear kinetic energy operator; that is, by the sudden rotation of the internuclear axis near the distance of closest approach. Briggs and Macek (1972) have examined the formulation of the corresponding problem for protons incident on hydrogen (Bates and Williams, 1964), and applied it in the calculation of K-shell vacancy production in Ne^+–Ne collisions. They used a two-state approximation, with $2p\sigma$ and $2p\pi$ orbital energies from Larkins (1972), and did a direct numerical integration of the resultant coupled differential equations. The Bates and Williams treatment assumes a classical path for the nuclei and Briggs and Macek used both straight line and Coulomb paths. They found that the deflected path calculation provides a marked apparent threshold effect, similar to that shown by the data. In Sec. 3.3.4 we show a comparison of their total cross section results with experiment. The results are very encouraging.

3.1.5(d) *Projection Operator Formulation*

An alternative description, known to be successful in atomic resonant state problems, has been proposed by O'Malley (1967). As in Smith's treatment the emphasis here is in making rigorous the ideas discussed in the first part of this section. This approach relies on projecting the wave functions onto a part of the Hilbert space, and also results in a nondiagonal electronic energy matrix, which provides the coupling for the inner-shell excitation in question. As outlined by O'Malley, the application of projection operator techniques (known as the Feshbach formalism) would be limited to slow collisions, because of the use of Born–Oppenheimer approximation. No calculations specifically on inner-shell excitation have been performed, but several electron-atom collision problems have been successfully approached by this method (Chen, 1964; Lipsky and Russek, 1966) and the process of dissociative attachment ($AB+e\rightarrow A^-+B$) has been formulated in this fashion (O'Malley, 1966).

3.2 Scattering Experiments

3.2.1 *Introduction*

Evidence for excitation of inner-shell electrons in heavy ion–atom collisions has been obtained in atomic scattering experiments. In these experiments one measures, as a function of the distance of closest approach, the inelastic energy loss

$$Q=T_0-(T_1+T_2), \tag{3.11}$$

where T_0, T_1, and T_2 are the kinetic energies of the incident, the scattered, and the recoil particles, respectively. Studies of Ar^+–Ar collisions produced the first indication of inner-shell vacancy phenomena. Morgan and Everhart (1962) measured the recoil energy and angle of the target atom and used these measurements to calculate the inelastic energy loss for the collision. They discovered an anomalous behavior for collisions whose distance of closest approach r_0 was approximately 0.23 Å. Near this value of r_0 a sharp increase in the inelastic energy loss was observed. In addition, it was found that in this region the inelastic energy loss was multivalued, having two and sometimes three values. The multivalued structure was at first found to be consistent with a model in which electrons were assumed to be ejected in pairs. In order to verify this idea it became desirable to observe the charge state of both ions after the collision. This led to a series of experiments in which the incident projectile and the recoil target atom were detected in coincidence after the collision. An advantage of these experiments is that in addition to determining the inelastic energy loss as a function of distance of closest approach one can also measure the final charge states of both ions. The first coincidence experiments showed that electrons were *not* ejected in pairs; however, three discrete peaks in the inelastic energy-loss spectrum were clearly observed. To explain these results Fano and Lichten (1965) reintroduced the idea of electron promotion by molecular orbitals and level crossings. According to these arguments, the inner-shell electron is promoted but still remains in the atom; thus, only one electron is ejected during the collision. Fano and Lichten proposed that the three peaks observed in the inelastic energy-loss measurements have the following explanation: The first peak, the lowest energy-loss measured, corresponds to collisions where no L-shell vacancies were produced, the second, intermediate, peak corresponds to collisions where one L-shell vacancy is produced and the third peak corresponds to collisions where two L-shell vacancies are produced. The prediction was made that fast Auger electrons would be emitted during these collisions. These predictions were later confirmed at several laboratories. Later experimental studies of Auger electrons in coincidence with scattered ions in Ar–Ar collisions have directly supported the Fano and Lichten interpretation.

In this section we will give a brief introduction to the experimental techniques used in such measurements, followed by discussion of the available data. Our emphasis in the discussion of data will be on the manifestations of *inner-shell* vacancies in the scattering experiments; we have included only those data in which the effects of inner-shell vacancies are clearly observed.

3.2.2 *Experimental Procedures*

The atomic scattering experiments have been performed in at least four different ways: the recoil-particle method, the scattered-particle method, the coincidence method, and the "improved coincidence method." In the first two techniques the energy and the angle of the respective particles are measured. By means of Eq. (3.11) and momentum conservation in the collision, in the recoil particle method, one can obtain

$$Q=2(T_0T_2/\gamma)^{1/2}\cos\phi-(1+\gamma^{-1})T_2, \quad (3.12)$$

where $\gamma=M_1/M_2$ is the mass ratio of the incident ion and the target atom, and ϕ is the recoil angle of the target atom with respect to the incident beam direction. For the scattered-particle method, the corresponding equation is

$$Q=2\gamma(T_0T_1)^{1/2}\cos\theta+(1-\gamma)T_0-(1+\gamma)T_1, \quad (3.13)$$

where θ is the scattering angle of the scattered, incident particle.

The experimental procedure is essentially the same in the first two methods. A scattering chamber containing the target gas is isolated by small collimating aperatures from the high vacuum region in which the scattered or recoiling particle is analyzed. The analyzing arm is capable of rotary motion around the scattering center. Energy and charge state analysis is accomplished by electrostatic or magnetic analysis, and the particles are detected using electron multipliers.

The third method is the coincidence method. A comprehensive review of these measurements, in which the scattered particle and the recoil particle are detected in coincidence, has been presented by Kessel (1969a). The first such experiments resulting in the observation of the triple peak region of inelastic energy losses were performed independently by the Leningrad Group (Afrosimov *et al.*, 1964, 1966) and the University of Connecticut Group (Everhart and Kessel, 1965, 1966; Kessel, Russek, and Everhart, 1965; Kessel and Everhart, 1966). While the experimental systems used by the two groups were mechanically quite different, they comprised the same basic features. Two analyzer arms capable of rotary motion around the scattering center are used and both particles are detected in coincidence for different well defined scattering and recoil angles. Knowledge of incident ion energy and the scattering and recoil angles allows the calculation of inelastic energy loss for a single collision. Again using conservation of momentum, one obtains

$$T_1=T_0\sin^2\phi/\sin^2(\theta+\phi) \quad (3.14)$$

and

$$T_2=T_0\gamma\sin^2\theta/\sin^2(\theta+\phi). \quad (3.15)$$

The inelastic energy loss is then calculated from Eq. (3.11). Charge state analysis for both particles was accomplished by magnetic analysis (Leningrad Group) or electrostatic analysis (University of Connecticut Group).

The fourth method, the improved coincidence technique, was developed by Afrosimov *et al.* (1969). In this work both particles are detected in coincidence, but in addition the energies of both particles are measured *directly*. The inelastic energy loss is then calculated directly from Eq. (3.11). By using high-resolution spectrometers Afrosimov *et al.* (1969) were able to measure the intrinsic width of the triple peaks for Ar^+–Ar collisions. To date this technique has provided the most accurate measurements of the inelastic energy loss.

The most important feature of all the scattering experiments is their ability, for a given collision, to relate the inelastic energy loss (Q) data to r_0, the distance of closest approach. The determination of r_0 involves the assumption of a screened Coulomb potential and a classical trajectory; Everhart, Carbone, and Stone (1955) tabulate r_0 values in terms of the center-of-mass scattering angle, which is readily calculated from θ and ϕ. In most combinations of θ and ϕ in atomic scattering experiments to date, the center-of-mass scattering angle depends so strongly on θ that variations of a few degrees in ϕ do not appreciably change r_0. Thus, in the coincidence techniques, by fixing θ and varying ϕ over a small range, the experimenter can measure a probability distribution of Q values at a fixed distance of closest approach.

The principal uncertainty introduced in the inelastic energy-loss spectra is due to thermal motion of the target. As a result, the improved coincidence technique provides the best resolution of all four methods since the energy of both particles is measured directly. Fastrup, Hermann, and Smith (1971) have discussed the relative merits of the three remaining techniques; they find the resolution of the scattered-particle technique to be superior to the other two.

Since high resolution is an essential ingredient when one is trying to observe the effects of inner-shell vacancies in the energy-loss spectra one concludes that the scattered-particle method of Fastrup, Hermann, and Smith (1971) and the improved coincidence measurements of Afrosimov *et al.* (1969) represent the best measurements of these effects. For this reason, in the discussion of the experimental results, we will refer to these measurements when several different measurements have been made.

3.2.3 *Experimental Results*

Generally, the experimental data have been of two types. The first category, which is typified by the Ar^+–Ar collision, involves the "triple peak" structure. This structure has usually been associated with production of L-shell vacancies and is characterized by a unit probability for producing two L-shell vacancies at small distances of closest approach. The second cate-

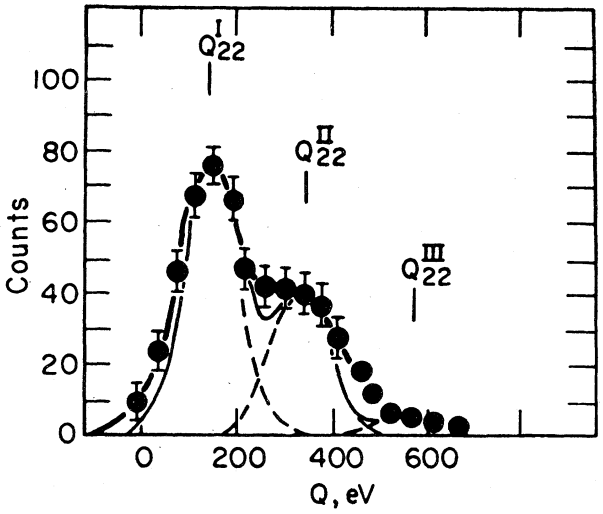

FIG. 3.3. Typical inelastic energy-loss spectrum. The number of coincidence counts is plotted as a function of the energy loss Q. The events correspond to 50-keV Ar^+–Ar collisions where the final charge states of both the projectile and the target are $+2e$ and the distance of closest approach is 0.27 Å. The data are from Afrosimov (1964) and the figure is from Kessel (1969).

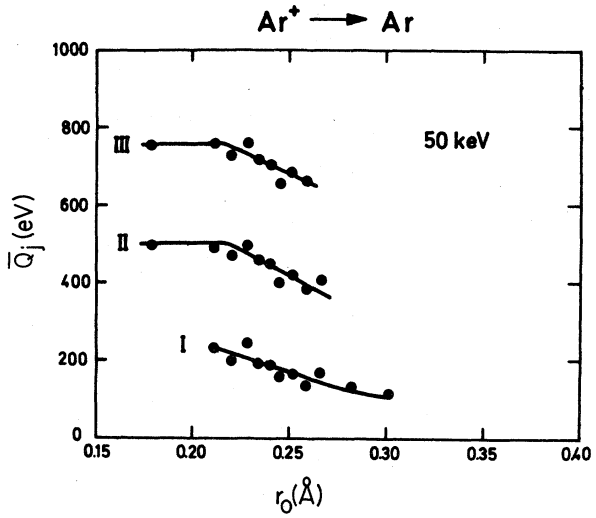

FIG. 3.5. The values of the average inelastic energy loss, $\bar{Q}^{I}$, $\bar{Q}^{II}$, and $\bar{Q}^{III}$ are plotted as a function of distance of closest approach r_0 for 50-keV Ar^+–Ar collisions. [After Fastrup, Hermann, and Smith (1971).]

gory, which is typified by the Ne^+–Ne collision, will be referred to as "double peak" observations. In these collisions, inner-shell vacancies (usually K shells) are observed as low probability events. Usually only two peaks (one inner-shell vacancy) are observed and the probability of producing the inner-shell vacancy is less than 0.5. In Sec. 3.2.4 we discuss the results of more energetic scattering experiments where inner-shell vacancies clearly must be present but for which no multiple peaks have been resolved.

3.2.3(a) *Triple Peak Observations*

(1) *Symmetric collisions*

Ar^+–Ar. The first clear observations of the triple peak structure were the coincidence measurements in the Ar^+–Ar scattering experiments (Afrosimov *et al.*, 1964, 1966; Kessel and Everhart, 1965, 1966a, b; Kessel, Russek, and Everhart, 1965). In Fig. 3.3 a typical spectrum obtained from the coincidence measurements is presented. The relative number of coincidence counts is plotted vs the energy loss Q. The spectrum indicates three separate peaks which are designated by the energy losses Q^{I}, Q^{II}, and Q^{III} at the peaks such that $Q^{I}<Q^{II}<Q^{III}$. An additional designation in Fig. 3.3 refers to the final charge states; for example Q_{mn} corresponds to measurements where $+me$ and $+ne$ were the final charge states of the scattered and recoiling particles, respectively. In referring to measurements where all charge states have been col-

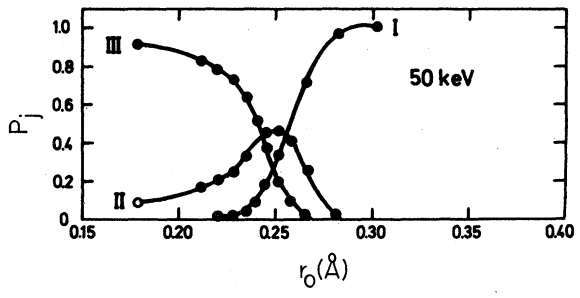

FIG. 3.4. The relative probabilities, P_j, for events in the $\bar{Q}^{I}$, $\bar{Q}^{II}$, and $\bar{Q}^{III}$ peaks are plotted as a function of distance of closest approach r_0 for 50-keV Ar^+–Ar collisions. [After Fastrup, Hermann, and Smith (1971).]

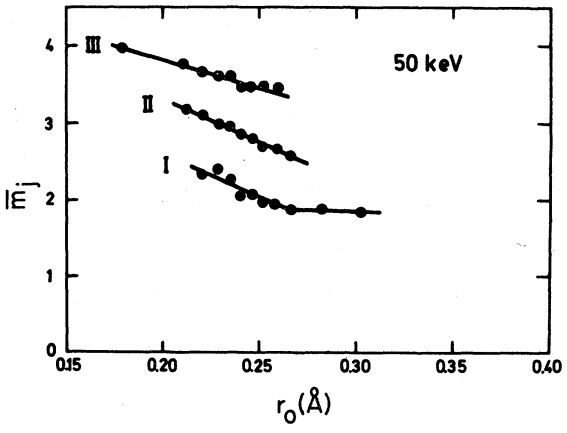

FIG. 3.6. The average final charge states of the scattered particle for events in the $\bar{Q}^{I}$, $\bar{Q}^{II}$, and $\bar{Q}^{III}$ peaks are plotted as a function of distance of closest approach r_0 for 50-keV Ar^+–Ar collisions. [After Fastrup, Hermann, and Smith (1971).]

lected, we designate the energy loss peak values as $\bar{Q}$. In Fig. 3.4 the relative probabilities for events in the $\bar{Q}^{I}$, $\bar{Q}^{II}$, and $\bar{Q}^{III}$ peaks are plotted as a function of distances of closest approach for the Ar^{+}–Ar collision at a fixed bombarding energy. For collisions involving large distances of closest approach (large impact parameters), only the $\bar{Q}^{I}$ peak is observed. However, for decreasing distances of closest approach, the $\bar{Q}^{II}$ peak increases until at 0.25 Å it dominates the spectra. At even smaller distances the $\bar{Q}^{III}$ peak increases until it reaches a probability of nearly 1.0. As previously discussed, the interpretation of the triple peak region in terms of inner-shell vacancies is quite simple: The first peak ($\bar{Q}^{I}$) corresponds to collisions where only outer-shell (M shell) excitation, and no L-shell vacancies have been produced. The intermediate peak ($\bar{Q}^{II}$) corresponds to collisions where *in addition* one L-shell vacancy is produced, and the third peak ($\bar{Q}^{III}$) corresponds to collisions where two L-shell vacancies are produced. In Fig. 3.5, $\bar{Q}^{I}$, $\bar{Q}^{II}$, and $\bar{Q}^{III}$ values are plotted as a function of the distance of closest approach. In Fig. 3.6 the average charge state of the scattered particle is presented as a function of the distance of closest approach for the three peaks. The same rise observed in the inelastic loss measurements is also observed in the average charge state of the scattered particle. Since this rise is seen in the Q^{I} peak where no inner-shell vacancies have been produced, it is reasonable to assume that the rise in all three peaks is due to additional outer-shell (M-shell) excitation at smaller distances of closest approach.

In the molecular-orbital description (Sec. 3.1), the L-shell vacancies in argon are assumed to be produced by level crossings of the rapidly rising $4f\sigma$ level in the quasimolecule formed during the collision (see Fig. 3.1). The $4f\sigma$ MO contains only two electrons and so it follows that it is completely depopulated at the smaller distances of cloest approach observed in Fig. 3.4 (i.e., events in the Q^{III} peak involve two L-shell vacancies); this is consistent with the general discussion of rapidly rising MO's in Sec. 3.1.4.

An experimental verification that the triple peaks correspond to inner-shell vacancy production is provided by the coincidence measurements of Thomson, Laudieri, and Everhart (1971). In this experiment, L-shell Auger electrons in the energy range 100–250 eV, created in the Ar^{+}–Ar collision, were measured in coincidence with incident particles scattered at a fixed scattering angle. By varying the incident energy of the argon projectile from 10 to 30 keV, they were able to measure the relative probability α of producing an Auger electron (typifying an L-shell vacancy) as a function of distance of closest approach. Everhart and Kessel (1966) have calculated a similar probability of producing the high-energy inelastic peaks (Using the assumption of two independent processes the probabilities P_I, P_{II}, P_{III} of producing Q^{I}, Q^{II}, Q^{III}, respectively, are, in terms of α, $P_I=(1-\alpha)^2$, $P_{II}=2\alpha(1-\alpha)$, and $P_{III}=\alpha^2$. Using data similar to Fig. 3.4, Everhart and Kessel obtained the probability α as a function of distance of closest approach.) In Fig. 3.7 the two probabilities are compared and found to be in good agreement, thus confirming the association of the "triple peaks" with L-shell vacancy production.

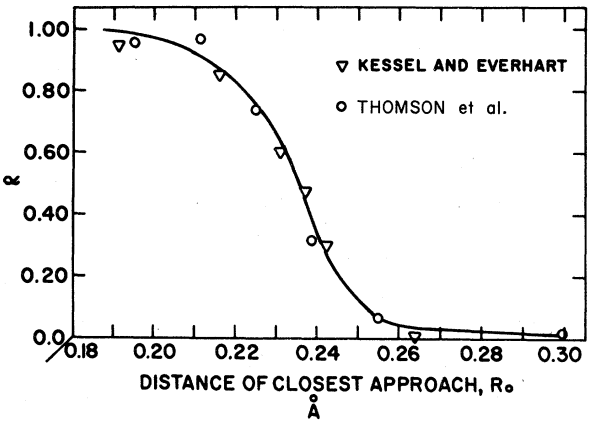

FIG. 3.7. The probability α of producing an inner-shell vacancy is plotted as a function of distance of closest approach R_0. The values of Kessel and Everhart (1966) were derived from the results of the scattering experiments using data similar to that in Fig. 3.4. The value of Thomson, Laudieri, and Everhart (1971) was measured by detecting L-shell Auger electrons in coincidence with scattered particles. [After Thomson *et al.* (1971).]

The energy separations between the peaks, $\bar{Q}^{II-I}$ and $\bar{Q}^{III-II}$, are the promotion energies of the first and second L-shell electrons, respectively. In Table 3.1 these energies are shown for all the collisions where the triple peak structures have been observed. In most of the cases in which more than one measurement has been made, the data with the highest resolution have been used.

The measured L-shell promotion energies, $\bar{Q}^{II-I}$ and $\bar{Q}^{III-II}$, for the Ar^{+}–Ar collision are 257 and 266 eV, respectively, for the improved coincidence technique, and a symmetric 254 and 254 eV for the scattered-particle method. Within the quoted experimental uncertainties, the two sets of numbers agree. These measurements are larger than the ground state $2p$ binding energies of argon (~245 eV). This presents an interesting question concerning these measurements. Lichten (1967) argued that the promotion energies should not exceed ground state binding energies and should be roughly independent of the state of ionization of the atom. Afrosimov *et al.* (1970) have measured the dependence of these energies on the total final charge state of the atomic particles and conclude that when the total final charge state $m+n$ varies between 2 and 6 the changes in the promotion energies Q^{II-I} and Q^{III-II} are not more than 23 eV and 7 eV, respectively. On the other hand, measured x-ray spectra from Ar^{+}–Ar collisions (see Sec. 3.4.3) show x-ray lines having energies greater than the argon ground state $2p$ binding

TABLE 3.1. A summary of the inelastic energy loss differences $\bar{Q}^{i-i'}$, average charge state differences $\bar{m}^{i-i'}$ and $\bar{n}^{i-i'}$, and intrinsic linewidths $\Delta\bar{Q}^{i-i'}$ for the various collisions where the "triple peak" region in the inelastic energy loss spectra has been observed. The collisions designated (A) are from Afrosimov *et al.* (1969, 1971) using the improved coincidence technique. The collisions designated (F) are from Fastrup, Hermann, and Smith (1971) using the scattered-particle method. T_0 is the incident energy of the projectile, and r_0 corresponds to the center of the triple peak Q region (P_{II} at maximum).

Collision partners	T_0 (keV)	r_0 (Å)	$\bar{Q}^{II-I}$ (eV)	$\bar{Q}^{III-II}$ (eV)	$\bar{m}^{II-I}$	$\bar{m}^{III-II}$	$\bar{n}^{II-I}$	$\bar{n}^{III-II}$	$\Delta\bar{Q}^{II-I}$ (eV)	$\Delta\bar{Q}^{III-II}$ (eV)
Ar^+–Ar (A)	25	0.24	257±10	266±8	0.70±0.10	0.70±0.10	0.7±0.1	0.7±0.1	65±15	65±15
Ar^+–Ar (F)	50	0.247	254±20	254±20	0.7	0.65				
Kr^+–Kr (A)	25	0.39	91±7	88±7	0.70±0.20	0.50±0.15			25±15	20±25
N^+–Ar (A)	48	0.10	250±10	294±10	0.05±0.15	0.10±0.15			75±30	110±25
Ne–Ar (A)	48	0.10	221±16	265±30	−0.30±0.10	−0.10±0.15				
Ne^+–Ar (A)	48	0.10	214±10	260±25	−0.30±0.10	−0.10±0.15	1.0±0.3	1.1±0.3	70±35	70±35
Al^+–Ar (F)	20/30	0.31	70±10	90±10		1.1				
P^+–Ar (F)	20/30/50	0.285	127±10	168±10	1.1	1.0	0	0		
S^+–Ar (F)	40	0.275	160±10	200±10	1.2	1.0				
Cl^+–Ar (F)	60	0.263	190±15	238±15	1.2	1.0				
Cl^+–Ar (A)	25	0.26	229±10	257±12	1.15±0.10	0.95±0.15	0±0.2	0±0.2	60±10	65±20
K^+–Ar (F)	60	0.238	246±20	294±20	0.35	0.35				
Mn^+–Ar (F)	60	~0.16	233±30	267±30	0	0				

energy. Since the x-ray process is simply the inverse of electron promotion, one can thus expect electron promotion energies greater than ground state binding energies. The reason for this is that screening by the outer-shell electrons strongly affects inner-shell binding energies. The large x-ray energies observed reflect the increase in the binding energy of the promoted electron due to multiple outer-shell excitation. Note that a 264-eV x-ray transition (interpreted as being most likely a $3d \rightarrow 2p$ transition) observed at 50-keV bombarding energy in the Ar^+–Ar collision agrees well with the observed electron promotion energies. It should be emphasized that this comparison of the x-ray spectral measurements with the scattering experiments is not completely rigorous. In the scattering experiments the measurements are restricted to a fixed distance of closest approach, whereas the x-ray spectral measurements are representative of an average of all possible distances of closest approach. We will return to this discussion in Sec. 3.2.4.

Another important aspect of the electron promotion energies $\bar{Q}^{III-II}$ and $\bar{Q}^{II-I}$ is that, within experimental uncertainty, they are the same. We will see later that in asymmetric collisions, where both vacancies are produced in the same atom, the promotion energy for the second electron is significantly larger than that for the first. The fact that the promotion energies are about the same in the symmetric collision suggests that when two L-shell vacancies are produced, most probably one is produced in each atom (this is the energetically preferred mode).

In a direct ionization of an inner shell the average charge state is expected to change by two, accounting for the electron which is ejected and for the subsequent autoionization. (Since the fluorescence yield is small for these vacancies, the radiative transition is unimportant in these considerations.) In the case of inner-shell vacancy production via electron promotion, the average state of ionization changes by only one, since the promoted electron remains in the atom. Thus, in principle, by monitoring the change in average state of ionization one can study the excitation mechanism, and determine which atom has the inner-shell vacancies. A summary of these measurements is presented in Table 3.1.

For the Ar^+–Ar collision, the change in the state of ionization is the same for both the target and the projectile. In addition, the change in ionization is the same for both L-shell vacancies. This suggests that the L-shell vacancies are equally likely to be produced in each atom, and that the mechanism for the vacancy production is similar for both. Del Boca, Hayden, and Thomson (1971) have reported observations of collisions in which no ionization is produced by purely outer-shell processes. In these collisions they find that only one electron is ejected per L-shell vacancy, as would be expected in the electron promotion mechanism. However, when all final charge states are con-

sidered, the total change in the final charge state is 1.4 electrons (0.7 per atom) for each L-shell vacancy. The value is intermediate between that expected for direct ionization and for electron promotion. We will see in the discussion of asymmetric collisions that this ambiguity is not as apparent in those cases. The reason for the anomaly in symmetric collisions, such as Ar^+–Ar, is not clear.

The high resolution measurements of Afrosimov *et al.* (1969, 1971) provide data on the intrinsic line width of the inner-shell excitation, $\Delta\bar{Q}^{l-l'}$. This quantity is defined by the equation

$$\Delta\bar{Q}^{l-l'}=[(\Delta\bar{Q}^{l'})^2-(\Delta\bar{Q}^{l})^2]^{1/2}, \qquad (3.16)$$

where $\Delta\bar{Q}^{l}$ and $\Delta\bar{Q}^{l'}$ are the linewidths of $\bar{Q}^{l}$ and $\bar{Q}^{l'}$, respectively. When these numbers have been measured, they are also included in Table 3.1.

For the Ar^+–Ar collisions, the intrinsic linewidths $\Delta\bar{Q}^{II-I}$ and $\Delta\bar{Q}^{III-II}$ are both 65 eV. Several possible factors may contribute to the width. The effect of final charge state is one possibility. The width $\Delta\bar{Q}^{III-II}$ appears to exhibit some dependence on the final charge state but $\Delta\bar{Q}^{II-I}$ appears to be relatively insensitive to this. We will return to this point in Sec. 3.2.4.

Kr^+–Kr. The Kr^+–Kr collision has been investigated by several experimenters. The first results (Afrosimov *et al.*, 1966; and McCaughey *et al.*, 1968a, b) used the coincidence scattering technique. These early measurements were not able to resolve any triple structures but the data did show several plateaus in the inelastic energy loss spectra. Afrosimov *et al.* (1971), using the improved high resolution coincidence technique, were able to resolve the triple peak structure. The results of their measurements are summarized in Table 3.1 and Fig. 3.8.

Vacancy production via molecular orbitals, completely analogous to that for Ar^+–Ar collision, is expected for Kr^+–Kr. Electron promotion of $3d$ electrons via a rapidly rising $6h\sigma$ MO (see Barat and Lichten, 1972, Fig. 4) is a parallel to $2p$ promotion via the $4f\sigma$ level in Ar^+–Ar collisions. It is not surprising, then, that the relative probabilities $P_{\rm I}$, $P_{\rm II}$, and $P_{\rm III}$ for Kr^+–Kr collisions, which are plotted in Fig. 3.8 as a function of distance of closest approach r_0 should have the same characteristic behavior as those observed in the Ar^+–Ar collisions (Fig. 3.4).

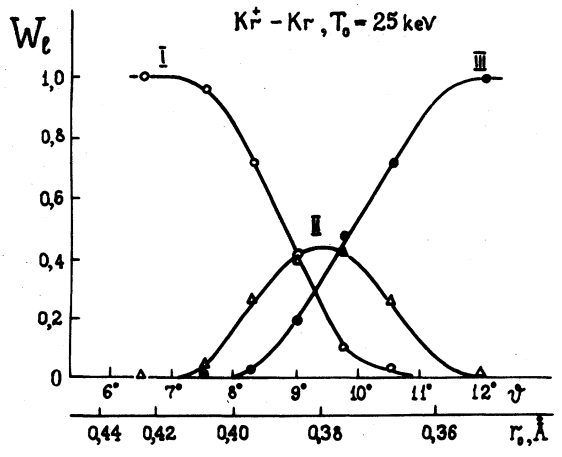

FIG. 3.8. The relative probabilities W_l for events in the $\bar{Q}^{I}$, $\bar{Q}^{II}$, and $\bar{Q}^{III}$ peaks are plotted as a function of distance of closest approach r_0 for 25-keV Kr^+–Kr collisions. [After Afrosimov *et al.* (1971).]

The electron promotion energies $\bar{Q}^{II-I}$ and $\bar{Q}^{III-II}$ are both approximately 89 eV, which is the $3d$ Kr binding energy. The change in ionization state has been measured for the scattered particle only; within experimental uncertainty its value is the same as that for the Ar^+–Ar measurements. Measurements of the intrinsic linewidths are reported but they are dominated by instrumental effects.

(2) *Asymmetric collisions*

In discussing asymmetric collisions it is useful to first discuss the molecular orbital diagrams for these collisions. These correlation diagrams are constructed (see Sec. 3.1) by joining separated atom levels, in order of decreasing binding energy, with the lowest unfilled level in the combined atom that has the same number of radial wave function nodes [i.e., equal $(n-l-1)$]. Figures 3.2(a) and 3.2(b) show two cases where the $1s$ binding energy of the collision partner is near the Ar $2p$ binding energy. In the first case, B+Ar, the Ar $2p$ electrons have no level crossing in the quasimolecule formed during the collision. On the other hand, the B $1s$ electrons are in a steeply rising $3d\sigma$ MO. Transitions can occur with empty $3d\pi$ and $3d\delta$ MO's. Also, it is probable that the steepness of the $3d\sigma$ level results, at least for higher bombarding energies, in strong coupling to the continuum through nonadiabatic terms, with resultant large excitation probabilities. The appropriate $2p$ and $1s$ binding energies are reversed in the C+Ar case [Fig. 3.2(b)]. The $2p$ electrons of Ar are then in the steeply rising $3d\sigma$ MO, whereas the C $1s$ electrons have no level crossings. In this case we expect to find vacancies in the Ar L shell.

The same general effect is seen when $2p$ electrons of both partners have near matching energies, except that electron promotion in these cases is produced by the $4f\sigma$ MO. In the Al–Ar case shown in Fig. 3.2(c) the $4f\sigma$ level has two Al $2p$ electrons and so we would expect vacancies to be produced in the Al $2p$ shell. The role is reversed in the Ca–Ar case shown in Fig. 3.2(d). In this case, the $2p$ binding energy of Ca is greater than that of Ar. The effect of this larger binding energy is that now the $2p$ electrons of Ar are in the $4f\sigma$ level and thus the vacancies are produced in the Ar $2p$ level.

It is appropriate in the following to discuss the asymmetric collisions in two categories. The first

TABLE 3.2. The $2p_{3/2}$ and $2p_{1/2}$ binding energies of various elements.

Element	Binding energy (eV)
Al	73, 74
P	135, 136
S	164, 165
Cl	200, 202
Ar	245, 247
K	294, 297
Mn	641, 652

category involves electron promotion via a $4f\sigma$ molecular orbital [Figs. 3.2(c) and (d)]. These data are characteristic of the L-shell–L-shell interaction. The second category represents $3d\sigma$ electron promotion in the vicinity of the K-shell–L-shell level match [Figs. 3.2(a) and (b)]. Similar comments could be made regarding L-shell–M-shell, M-shell–M-shell, etc., interactions, but no data corresponding to inner-shell excitation have been published on these collisions.

Electron promotion via the $4f\sigma$ or $3d\sigma$ level can produce two inner-shell vacancies. In the symmetric collisions, the diagrams indicate that the vacancies can be produced with equal probability in either collision partner; this is consistent with the data. In asymmetric collisions, the situation is quite different; as indicated by the correlation diagrams both electrons in the $4f\sigma$ or $3d\sigma$ levels are from the same collision partner and thus both vacancies are expected to be produced in the *same* atom. We will see the consequences of this in the following discussion.

L-Shell–L-Shell interaction ($4f\sigma$ *promotion*). The triple peak structures in asymmetric collisions are best illustrated by collisions where the interaction concerns two L shells. These measurements (Fastrup and Hermann, 1969; Afrosimov *et al.*, 1971; and Fastrup, Hermann, and Smith, 1971) have involved collisions of Ar with collision partners in the range $Z=13$–25. Triple peak structures very similar to those shown in Figs. 3.3–3.6 have been observed (see Table 3.1).

Molecular-orbital diagrams predict electron vacancy production via the $4f\sigma$ level in the collision partner with the lower $2p$ binding energy—that is, for the partner with lower Z. Thus, in collisions of Ar with Al, P, S, and Cl we would expect the vacancies to be not in Ar but in the other collision partner. For the collisions K–Ar and Mn–Ar, on the other hand, the vacancies are expected to be in the Ar atom. Indeed, the data do support these molecular-orbital ideas, and, in fact, this general observation for L-shell–L-shell interactions was made by Fastrup and Hermann (1969) prior to the discussion of asymmetric molecular orbitals by Barat and Lichten (1972).

In the scattering experiments one can establish the locations of the vacancies by observing either the electron promotion energies $\bar{Q}^{\mathrm{II-I}}$ and $\bar{Q}^{\mathrm{III-II}}$ or the changes in the average states of ionization $\bar{m}^{\mathrm{II-I}}$, $\bar{m}^{\mathrm{III-II}}$, $\bar{n}^{\mathrm{II-I}}$, and $\bar{n}^{\mathrm{III-II}}$. Comparison of the electron promotion energies $\bar{Q}^{\mathrm{II-I}}$ and $\bar{Q}^{\mathrm{III-II}}$ in Table 3.1 for the Al^+–Ar, P^+–Ar, and S^+–Ar collisions with the $2p$ binding energies in Table 3.2 shows that the inner-shell vacancies are produced in the collision partner other than Ar. Indeed, measurements of the change of ionization presented in Table 3.1 substantiate these observations. A change in the state of ionization varying between 1.0 and 1.2 is seen for the projectile, consistent with L-shell vacancy production in the projectile due to electron promotion (as opposed to direct ionization). In the case of the P projectile, the changes in ionization of the Ar target, $\bar{n}^{\mathrm{II-I}}$ and $\bar{n}^{\mathrm{III-II}}$ have been measured and no change was seen, as would be expected from the previous discussion. Dahl and Lorents (1971) have measured Auger electrons in coincidence with scattered particles for the P^+–Ar 50-keV collisions. They observed a 62-eV P Auger electron in coincidence with P^{5+} ions.

The first excitation energies $\bar{Q}^{\mathrm{II-I}}$ for Al^+–Ar, P^+–Ar, and S^+–Ar agree, within experimental uncertainty, with the projectile $2p$ binding energies. On the other hand, the second excitation energy $\bar{Q}^{\mathrm{III-II}}$ is consistently larger than both the projectile $2p$ binding energy and the first excitation energy $\bar{Q}^{\mathrm{II-I}}$. This trend is seen in all triple peaks for asymmetric collisions. The reason for this is that both vacancies are produced in the same atom. Just as the second ionization potential is greater than the first in outer-shell excitation, more energy is required to excite the second inner-shell electron than the first.

For the Cl^+–Ar collision, two measurements are available. The scattered-particle method gives excitation energies $\bar{Q}^{\mathrm{II-I}}$ and $\bar{Q}^{\mathrm{III-II}}$ of 190 and 238 eV, respectively. The improved coincidence technique gives 229 and 257 eV for the same quantities. The discrepancy between the measurements is much greater than that in the symmetric Ar^+–Ar collisions. The reason for the discrepancy is not clear. One possible reason may be the different bombarding energies used in the two experiments; however, such a dependence on bombarding energy has not been observed in other collisions. The fact that the vacancies are produced in the Cl atom is clearly seen in the change in ionization, where both measurements agree very well. A change of ionization of about 1, consistent with electron promotion is seen for both excitations in the Cl atom. In the Ar target, no change in ionization is observed. The correlation of the excitation energies with the Cl $2p$ binding energies ($\sim$200 eV) is questionable due to the discrepancy of the two measurements, but the first excitation energy $\bar{Q}^{\mathrm{II-I}}$, obtained using the scattered-particle method, agrees well with the Cl $2p$ binding energy. It should be emphasized that in the previous discussions of asymmetric collisions, where agreement was found with the $2p$ binding energies, the data were all obtained using the scattered-particle method. On the other hand,

measurement of $\bar{Q}^{II-I}$ in the Cl^+–Ar collision, using the improved coincidence technique, gives a number substantially greater than the $2p$ Cl binding energy. As was discussed earlier, excitation energies greater than ground state binding energies can be due to outer-shell excitations.

In the Cl^+–Ar collisions, the intrinsic linewidths $\Delta\bar{Q}^{II-I}$ and $\Delta\bar{Q}^{III-II}$ are 60 and 65 eV, respectively. It is interesting that, in contrast to the Ar^+–Ar case, in the Cl^+–Ar collision the change in ionization agrees remarkably well with what one would expect in electron promotion, and yet large intrinsic linewidths are still observed.

In the collisions K^+–Ar and Mn^+–Ar we expect the $2p$ vacancies to be produced in the Ar target. The first electron promotion energy does agree well with the $2p$ binding energy of Ar. The second electron promotion energy is, as usual, larger. The change in the state of ionization is known only for the projectile. No change is seen for the Mn^+ projectile, but a small change is seen in the K^+ projectile. It is possible that this change in the state of ionization is due to production of $2p$ vacancies in K in a small fraction of the collisions. However, similar small changes in the state of ionization are seen in collisions which do not support this argument (e.g., Ne^+–Ar).

We mentioned previously that Everhart and Kessel had derived the probability α of producing an inner-shell vacancy by an analysis of data similar to that shown in Fig. 3.4. The basic assumption used is that the two electron promotions are independent. An immediate consequence of this assumption is that appropriate ranges of P_I, P_{II}, and P_{III} are 0 to 1.0, 0 to 0.5, and 0 to 1.0, respectively. The only data at variance with the assumption of independent probabilities is the Al^+–Ar data which are presented in Fig. 3.9. In the case of Al^+–Ar, the measured probabilities P^{II} vary between 0 and 0.7.

We have not yet addressed ourselves to the question of the internuclear distance at which the triple peak region appears. In Fig. 3.10, the distance of closest approach corresponding to the maximum probability of a $\bar{Q}^{II}$ energy loss (see Fig. 3.4) is plotted as a function of the nuclear charge of the projectile (Z_1) for collisions involving Ar targets. In addition, in the plot we have included the sum of radii of the $2p$ orbits in the colliding partners. The general Z_1 dependence of both quantities is similar and the triple peaks occur in a region where the overlap of both $2p$ atomic wave functions is large.

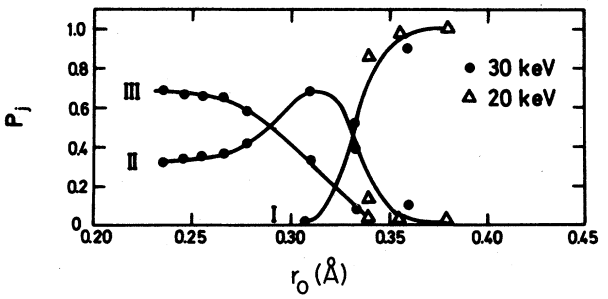

FIG. 3.9. The relative probabilities P_j for events in the $\bar{Q}^I$, $\bar{Q}^{II}$, and $\bar{Q}^{III}$ peaks are plotted as a function of distance of closest approach r_0 for 20-and 30-keV Al^+–Ar collisions. The data violate the assumption of independent probabilities for inner-shell vacancy production. [After Fastrup, Hermann, and Smith (1971).]

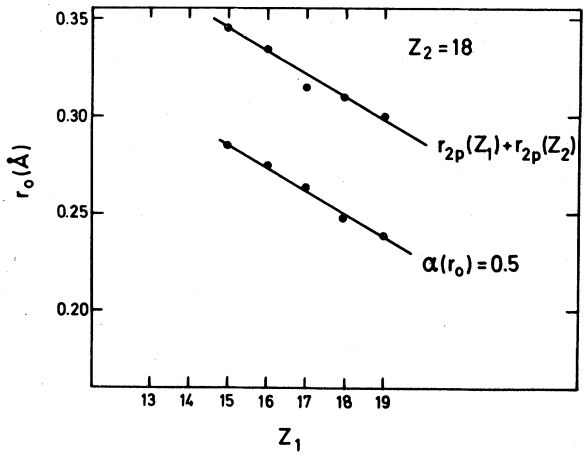

FIG. 3.10. A comparison of the r_0 value at which $P_{II}=1/2$, corresponding to the center of the triple peaked region, with the sum of the radii of $2p$ electrons in the projectile atom and the target atom. [After Fastrup, Hermann, and Smith (1971).]

K-shell–L-shell interaction ($3d\sigma$ *promotion*). The existence of triple structures for electron promotion by a $3d\sigma$ molecular orbital has not been clearly established. That is, no data similar to that shown in Fig. 3.4. have been reported. However, since the general behavior of the $3d\sigma$ molecular orbital (this is a steeply rising molecular orbital terminating near the continuum) is similar to that of the $4f\sigma$ it is believed that triple structures resembling those described in Figs. 3.3 to 3.6 should be observed as this area is further investigated. The first evidence for triple structures via $3d\sigma$ electron promotion is in the Ne^+–Ar collision (Afrosimov, *et al.*, 1966; Kessel, McCaughey, and Everhart, 1967). At 50-keV bombarding energy, two steps are seen in the inelastic energy loss when it is plotted as a function of distance of closest approach, indicating the production of one and then two inner-shell vacancies. Using the improved coincidence technique, Afrosimov, *et al.* (1971) have been able to resolve three peaks in the inelastic energy-loss spectra. Their data are listed in Table 3.1. On the basis of previous discussion we expect vacancies to be produced in the Ar L shell, as opposed to the Ne K shell (867 eV), as the result of electron promotion by the $3d\sigma$ molecular orbital. The data on electron promotion energies $\bar{Q}^{II-I}$ and $\bar{Q}^{III-II}$ and changes in the state of ionization $\bar{m}^{II-I}$, $\bar{m}^{III-II}$, $\bar{n}^{II-I}$, and $\bar{n}^{III-II}$ confirm this. The change in ionization of the Ar target $\bar{n}^{II-I}$ and $\bar{n}^{III-II}$ is approximately

one, consistent with the electron promotion mechanism. The state of ionization of the Ne projectile *decreases* a small amount upon the production of the first inner-shell vacancy. The reason for this change is not understood. In addition, we see that the first electron promotion energy $\bar{Q}^{II-I}$ is smaller than the Ar $2p$ binding energy. Whether this small electron promotion energy is associated with the decrease in the ionization of the Ne projectile is not clear and further work is necessary. Notice that in the case of the Ne–Ar collision the measurements are reported for both neutral and singly ionized Ne. Within experimental uncertainty, the measurements agree. The intrinsic linewidths $\Delta\bar{Q}^{II-I}$ and $\Delta\bar{Q}^{III-II}$ are also reported for the Ne^+–Ar collisions. The numbers are both 70 eV, similar to those for the Ar^+–Ar collisions.

Knystautas *et al.* (1970) studied N^+–Ar collisions using the coincidence technique. Afrosimov *et al.* (1971), using the improved coincidence technique reported electron promotion energies and a summary of their results is presented in Table 3.1. The results are in agreement with the MO picture. Bingham (1969) has studied O^+–Ar collisions using the coincidence technique. He reports an apparent second peak in the inelastic energy loss. Unfortunately, due to the poor resolution of the coincidence technique, it is difficult to obtain accurate electron promotion energies for this collision.

Note that in those collisions where inner-shell vacancies have been produced via the $3d\sigma$ MO, the vacancies are always produced in the L shell. An analogous set of collisions exists where the vacancies will be produced in the K shell, that is, in collisions where the $1s$ electron binding energy for one particle is less than the $2p$ electron binding energy of its collision partner [see, for example, Fig. 3.2(a)]. Unfortunately these collisions have not been investigated. These collisions are important as they represent a class of collisions where double K-shell vacancies can be produced. Work in this area is clearly needed.

3.2.3(b) *Double Peak Observations*

(1) *Symmetric collisions*

Ne–Ne. In these collisions usually only two peaks (one inner-shell vacancy) are observed in the inelastic energy-loss spectra and the probability of producing the inner-shell vacancy is less than 0.5. In addition, in many of these collisions the probability of producing an inner-shell vacancy is a strong function of the initial charge state of the incident ion. The double peak observations represent those collisions where the vacancies are produced in the K shell of one of the collision partners. In terms of a molecular-orbital description, electron promotion is via $2p\sigma$–$2p\pi$ rotational coupling. It is not surprising that this class of observations is fundamentally different from the triple peak observations, since in these collisions we are dealing with a single level crossing whereas in the triple peak observations many different level crossings are possible.

Ne–Ne collisions have been studied most extensively. Kessel, McCaughey, and Everhart (1966a, b, 1967) first reported the existence of a second peak in the inelastic energy loss spectra. More extensive measurements were made by Fastrup, Hermann, and Kessel (1971); the results of these measurements are presented in Fig. 3.11. These data exhibit two important properties which are characteristic of the double peak structures—that is, the inner-shell excitation probability P_{II} depends strongly on both the incident charge state and the velocity of the collision.

The dependence of the K-shell excitation probability on the incident charge state in Ne–Ne collisions was originally predicted by Lichten (1967). The Lichten predictions are consistent with Fig. 3.11. For example, at 300-keV bombarding energy, the K-shell excitation probability P_{II} at a fixed distance of closest approach r_0 is roughly twice as large for Ne^{2+}–Ne collisions as for Ne^+–Ne collisions. This charge dependence can be explained using the molecular-orbital diagrams (see Fig. 3.1). A K-shell electron can be promoted by $2p\sigma$–$2p\pi$ rotational coupling if a vacancy exists in the $2p\pi$ MO. In order for a vacancy to exist in the $2p\pi$ MO there must be an initial vacancy in the $2p$ atomic level of one of the collision partners. If the collision is neutral Ne on Ne the $2p\pi$ MO is filled and no electron transfer can take place. If, however, the collision is Ne^+–Ne then there exists one vacancy in the $2p$ level and thus a vacancy can appear in the $2p\pi$ MO. If the collision is Ne^{2+}–Ne the probability for a vacancy existing in the $2p\pi$ MO doubles. The Auger electron

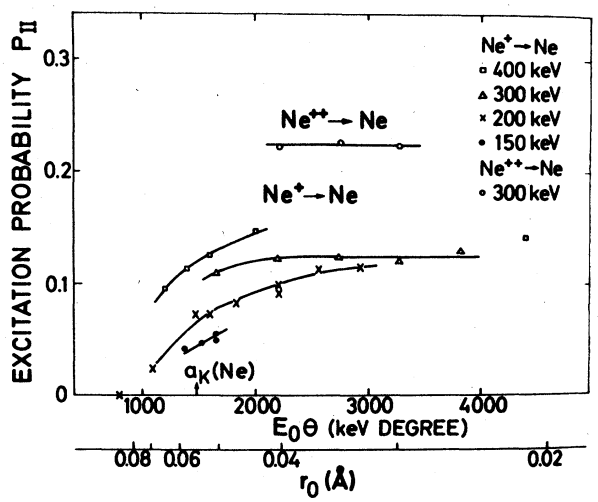

FIG. 3.11. The K-shell excitation probability P_{II} for Ne^+–Ne and Ne^{2+}–Ne collisions is plotted as a function of the distance of closest approach r_0 and, in addition, the product of bombarding energy and scattering angle, $E_0\theta$. The K-shell radius for a Ne atom, a_K(Ne) is indicated. [After Fastrup, Hermann, and Kessel (1971).]

measurements of McCaughey *et al.* (1968 a, b) indicate that the K-shell promotion probabilities for projectiles Ne^{2+}, Ne^{+}, and Ne are in the ratio of 2:1:0.6, in partial agreement with the prediction of 2:1:0 based on the above. It is not known if the discrepancy in the neutral Ne–Ne collision is due to a breakdown in the MO picture or whether it might be the result of projectiles not in the ground state at the time of collision. (For asymmetric collisions the general agreement with the MO predictions is better.)

The probability for producing two K-shell vacancies in a Ne–Ne collision should also be a function of the incident charge states. Molecular orbital considerations do not allow the production of two K shell vacancies in a Ne^{+}–Ne collision since there can be only one vacancy in the $2p\pi$ MO. This, however, is not the case in Ne^{2+}–Ne collisions. The experimental data simply show that the probability of producing two K-shell vacancies in any of the observed Ne–Ne collisions must be small, since a third peak in the inelastic energy loss spectra has not been observed.

In addition to the charge state dependence, the data presented in Fig. 3.11 also exhibit a strong velocity dependence—that is, the excitation probability P_{II} for a given distance of closest approach r_0 changes, depending on the incident energy of the projectile. This velocity dependence is characteristic of the $2p\sigma$–$2p\pi$ level crossing. The vacancies are being produced with high probability at distances of closest approach which are comparable to the K-shell radii of the collision partners. *Ab initio* calculations of Briggs and Macek (1972) for this crossing agree with the data presented in Fig. 3.11 to within a factor of 2. We have found that the Landau–Zener model (see Sec. 3.3) also provides a good functional form for both the velocity dependence of the total cross sections and the excitation probability P_{II} as a function of distance of closest approach.

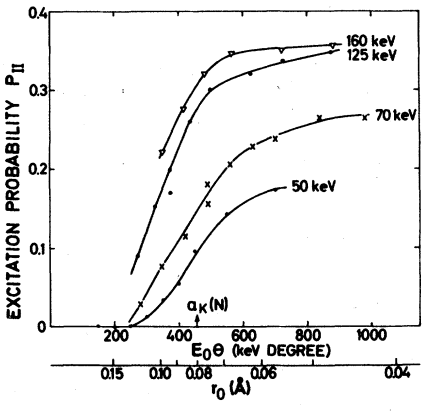

FIG. 3.12. The K-shell excitation probability P_{II} for N^{+}–N_2 collisions is plotted as a function of the distance of closest approach r_0, and in addition the product of bombarding energy and scattering angle, $E_0\theta$. The K-shell radius for a N atom $a_K(N)$ is indicated. [After Fastrup, Hermann, and Kessel (1971).]

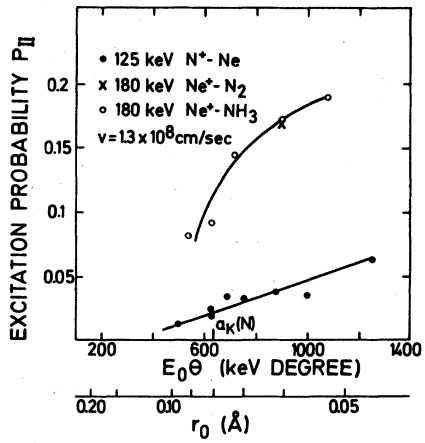

FIG. 3.13. The excitation probability P_{II} for the N K shell in N^{+}–Ne, Ne^{+}–N_2 and Ne^{+}–NH_3 collisions plotted as a function of distance of closest approach r_0, and the product of bombarding energy and scattering angle $E_0\theta$. The K-shell radius for the N atom $a_K(N)$ is indicated. [After Fastrup, Hermann, and Kessel (1971).]

N^{+}–N_2. The K-shell excitation probability in N^{+}–N_2 collisions was measured by Fastrup, Hermann, and Kessel (1971); their results are presented in Fig. 3.12. The measurements are very similar to the Ne^{+}–Ne results previously discussed. The over-all probability is higher in the N^{+}–N_2 collision but never larger than 0.5. The higher probability is probably due in part to the large number of vacancies in the $2p\pi$ MO. Only in these collisions has the existence of a third peak in the inelastic energy loss spectra (indicating the production of two K-shell vacancies) been reported.

(2) *Asymmetric collisions*

Production of K-shell vacancies via the $2p\sigma$–$2p\pi$ coupling can also occur in asymmetric collisions. The appropriate MO diagrams are represented by either Fig. 3.2(c) or 3.2(d). In the asymmetric case the electrons in the $2p\sigma$ level are the K-shell electrons of the *low* Z collision partner. The $2p\pi$ MO in this case is correlated with the $2p$ level of the *high* Z collision partner. Thus, on the basis of these diagrams two conclusions can be reached: First, the K-shell vacancies are expected to be produced in the collision partner of low Z (lower binding energy); second, if there is any dependence on initial charge state, it will depend only on the initial charge state of the higher Z (greater binding energy) collision partner.

The effects discussed above are best demonstrated in the N–Ne collisions reported by Fastrup, Hermann, and Kessel (1971). In Fig. 3.13, the N K-shell excitation probability, P_{II}, for three different collisions, N^{+}–Ne, Ne^{+}–N_2, and Ne–NH_3 is presented. The vacancies are produced in the collision partner of lower Z, N, as expected. In addition, there is a strong dependence on the initial charge state of the higher Z

(greater binding energy) collision partner. In the N^+–Ne collisions, where no $2p$ vacancies exist in the Ne atom, the probability for producing a K-shell vacancy in N is very small. However, in both Ne^+–N_2 and Ne^+–NH_3, where a single vacancy exists in the $2p$ level of Ne, the N K-shell excitation probability, P_{II}, has increased by more than a factor of 3.

Although in the N^+–Ne collisions the probability for producing a N K-shell vacancy remains small, it is definitely observed. However, Fastrup, Hermann, and Kessel (1971) report that in the Na^+–N_2 collision they were unable to observe the production of any K-shell vacancies. On the basis of molecular-orbital diagrams we expect these collisions to be the same, since the $2p\pi$ level will be filled in both cases. A possible explanation for this anomaly occurs if there is a breakdown in the simple MO model for these outer-shell electrons. In Sec. 3.1 we showed that molecular-orbital descriptions would be appropriate when $E/\lambda u$ is small, where E is the incident bombarding energy, λ is the projectile mass in electron mass units, and u is the electron binding energy. For the N^+–Ne and Na^+–N_2 collisions this corresponds to $E/\lambda u \approx 0.1$ when the $2p$ binding energy of Ne is used. Some breakdown of the MO concepts might be expected for such a value (see Sec. 3.3.2). This could result in a "mixing" of the N $2p$ level (9 eV) and the Ne $2p$ level (18 eV) which would result in possible vacancies in the $2p\pi$ MO. In the Na^+–N_2 collisions this "mixing" would be less due to the greater energy separation between the $2p$ levels. The $2p$ binding energy in Na is 31 eV.

3.2.4 Electron Promotion Energies and Higher Energy Collisions

In many energy loss measurements evidence for inner-shell vacancies is observed, but the resolution is not sufficient to resolve any structure in the energy-loss spectra. In these cases it is difficult to interpret the measurements and to obtain detailed information concerning the collision. In this section, we discuss high-energy collisions, and for a particular case, Ar^+–Ar, analysis of energy-loss measurements is presented.

The calculations of inner-shell electron promotion energies in heavy-ion–atom collisions is not straightforward because many electrons are excited and thus electron promotion energies cannot be determined from the ground state electron binding energies. Energy loss calculations which we will be discussing in this section were performed using Hartree–Fock–Slater wave functions and the virial theorem (i.e., $E_{\text{configuration}} = -\langle T \rangle$). The calculations were performed by removing one electron, allowing the atom to relax, then removing the next electron, and so on until a desired final charge state configuration was achieved. Thus, promotion is assumed to be from atoms relaxed to all but the final promotion. Where comparisons could be made with the full Hartree–Fock calculations, (Larkins, 1971a; E. Clementi, 1965), the Hartree–Fock–Slater results were about 10% higher. A general discussion of such calculational techniques is presented in Sec. 3.4.4.

The measurements of Afrosimov *et al.* (1969) for Ar^+–Ar collisions at 25 keV suggest that electron promotion energies for the Ar L shells are fairly independent of the final state of ionization. However, the opposite conclusion follows from the fact that the measured promotion energies are greater than ground state $2p$ Ar binding energies. We have performed calculations for Ar to determine the effect of M-shell excitation on L-shell electron binding energies. The calculations were performed by removing $3p$ electrons sequentially from the atom and then calculating the $2p \rightarrow 3d$ electron promotion energy. The results indicate that for symmetric final charge configurations the electron promotion energy ($2p \rightarrow 3d$) would vary from 254 to 278 eV while the final charge state varied between $+2$ and $+12$, while under the same conditions the $2p$ binding energy varied from 247 to 343 eV (see Sec. 3.4.4). This indicates that the electron promotion energy may be much less sensitive to outer-shell excitation than is the binding energy. In Afrosimov's measurements the final charge states varied between 2 and 6. Our calculations suggest that the $2p \rightarrow 3d$ promotion energies could be expected to vary between 254 and 263 eV for this same range of charge states. The experiments give values of 257 and 266 eV for $\bar{Q}^{II-I}$ and $\bar{Q}^{III-II}$ with changes (due to charge state) of no more than 23 eV and 7 eV, respectively. The results of the calculations are thus consistent with the experimental values.

These same calculations give us some insight into the intrinsic line widths $\Delta\bar{Q}^{I-I'}$ associated with these promotions. On the basis of our calculations, the measured width of 65 eV is larger than one would expect for $2p \rightarrow 3d$ promotions alone. However, if one

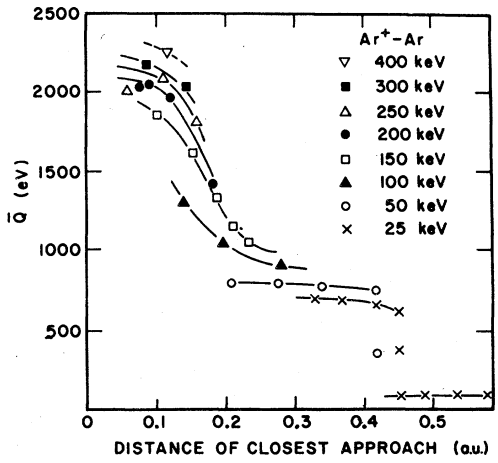

FIG. 3.14. The average inelastic energy loss $\bar{Q}$ in Ar^+–Ar collisions plotted as a function of distance of closest approach. [After Kessel and Everhart (1966).]

allows the $2p$ electrons to be promoted to many levels, some being near the continuum, then a wide range of promotion energies are available which might be consistent with the measured intrinsic widths.

The data in Table 3.1, previously discussed, give clear indications of the effect of multiple L-shell excitation on the electron promotion energies. In particular, in the asymmetric collision where both vacancies are produced in the same atom and the same amount of outer-shell excitation is involved, the second L-shell electron promotion energy is always greater than the first. In general, the promotion energies for these second L-shell electrons are in agreement with our calculations.

Kessel and Everhart (1966) have extended the energy-loss measurements for the Ar^+–Ar collision to 400 keV and to distances of closest approach much smaller than the region of the triple peaks. The results of their measurements are summarized in Figs. 3.14 and 3.15. From these figures we see that both the number of ejected electrons and the energy losses increase for larger bombarding energies and smaller distances of closest approach.

Since multiple peaks are not observed, calculations are required to interpret the data. The results of our calculations of the inelastic energy loss are presented in Fig. 3.16. The calculations were performed by removing electrons until the desired final charge state given in Fig. 3.15 was achieved. In addition, the total ionization is presumed to be about evenly split between the projectile and the target, in reasonable agreement with the data. Calculations were performed assuming that no inner-shell vacancies were produced. The results of these calculations are presented in Fig. 3.16(a). The dashed line in the Figure corresponds to adding the binding energy of the last electron to the calculated energy loss. This represents an attempt to correct for photon de-excitation in the outer shells which would not change the number of ejected electrons. As would be expected, the agreement is poor since we have failed to include possible L-shell vacancies.

In Fig. 3.16(b), calculations are presented where L-shell promotions have been added. It is assumed that L-shell vacancies change the final charge state by one, due to an Auger process. We have chosen this number since it is in the best agreement with the experimental numbers presented in Table 3.1. To obtain reasonable agreement with experiment, it is necessary to introduce two L-shell ($2p$) promotions at about 0.46 a.u. This is, of course, the triple peak region and so we expect two L-shell vacancies. To obtain reasonable agreement with the data, it is necessary again to invoke additional multiple L-shell vacancies between 0.1 and 0.2 a.u. In fact, it is necessary to invoke three additional $2p$ vacancies (five in total) with promotion energies of 348, 371, and 401 eV, respectively, to obtain reasonable agreement with the experiment. The agreement is best when the radiative correction has been added. The

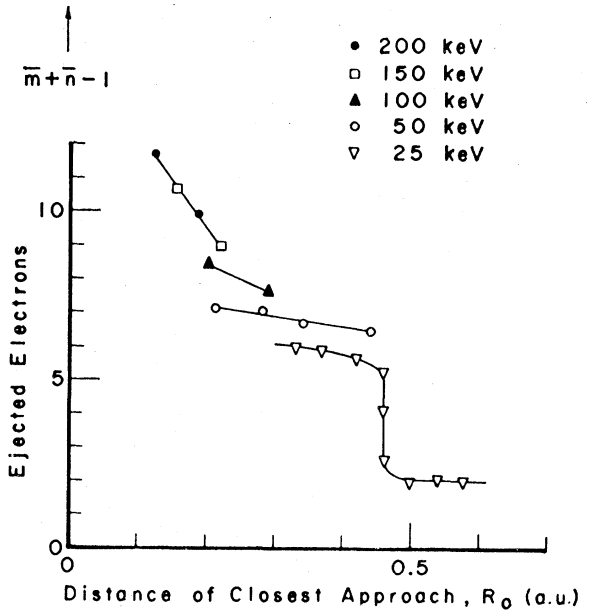

FIG. 3.15. The average number of ejected electrons, $\bar{m}+\bar{n}-1$, in Ar^+–Ar collisions plotted as a function of distance of closest approach. The data are from Kessel and Everhart (1966) and the figure is from Lichten (1967).

production of these additional L-shell vacancies is probably due to the $3d\sigma$, $3d\pi$, and $3d\delta$ MO's (see Fig. 3.1).

Kessel (1969b) has extended the inelastic energy-loss measurements to 1.5 MeV. A composite of all the energy-loss measurements for Ar^+–Ar is presented in Fig. 3.17. The inelastic energy losses increase in going from 0.05 to 0.02 Å. It is probably reasonable to attribute this rise primarily to additional L-shell promotions. Only two additional L-shell vacancies are required to explain the increase in the inelastic energy loss to 3000 eV. There is a final rise in the inelastic energy loss of about 3 keV which occurs between 0.01 and 0.02 Å. There is more than one explanation for this final rise. However, the most reasonable explanation is the production of a K-shell vacancy. This seems plausible since the 3-keV energy loss closely resembles the Ar $1s$ binding energy (3.2 keV). This is also consistent with the observation of Ar K x rays from these collisions (Kessel, Rose, and Grodzins, 1969).

Although in our discussion we have referred to production of $2p$ vacancies, the production of $2s$ vacancies is also possible. In fact Ogurtsov, Flaks, and Avakyan (1969a) have seen Auger electrons corresponding to the filling of $2s$ vacancies. However, the difference in the promotion energies for $2s$ and $2p$ electrons is small and this makes little change in the analysis.

Kessel (1969b) has extended the inelastic energy loss measurements to 1 MeV incident projectile energies for Ne^+–Ne and Ne^+–Ar collisions. These measure-

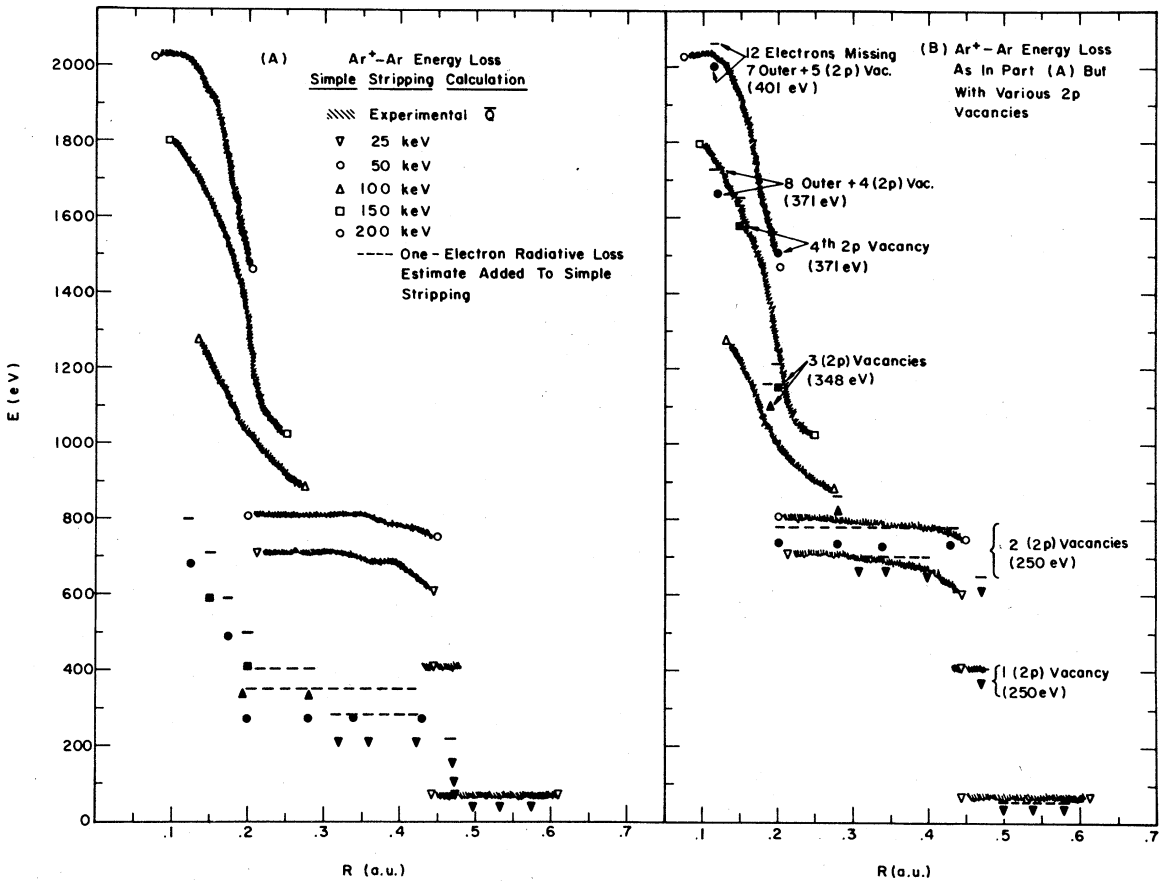

FIG. 3.16. Calculations of the average inelastic energy loss $\bar{Q}$ for Ar^+–Ar collisions are compared with experiment. The data are from Fig. 3.15 and are indicated by the open characters connected by the broad wavy line. The calculations are indicated by solid characters. The dashed lines represent radiative corrections to the calculations. In A, the calculations using the assumption of no inner-shell vacancies are presented. In B, the same calculations are presented except that the various $2p$ vacancies have been included. The relative number of outer vacancies and $2p$ vacancies is indicated in the figure. The number in the parenthesis indicates the electron promotion energy of the last $2p$ electron that has been removed. For details of calculation refer to the text.

ments show an increase in the inelastic energy loss as one goes to higher incident energies and smaller distances of closest approach. Kessel (1969b) has also measured the inelastic energy loss for 3 and 6 MeV I–Xe collisions. The energy losses are again large and suggest multiple excitation of the M shell and possibly some L-shell excitation.

3.3 Total Cross Section Measurements

3.3.1 Introduction

In this section we discuss cross section measurements for vacancy production by heavy ions. An attempt has been made to include essentially all the available data. The measurements involve direct observation of either characteristic x rays or Auger electrons that result from the filling of an inner-shell vacancy. The data underline two important features of the heavy ion–atom interaction: Cross sections are much larger than those for incident protons or alpha particles of comparable velocities, and the cross sections depend critically on the relative electron binding energies for the collision partners. These features are much stronger for lower collision velocities, and the low energy data support an interpretation based on molecular concepts. The dependence of cross sections on relative binding energies—the "level-matching" effect—is discussed in some detail, and models for predicting excitation cross sections are outlined. A discussion of fluorescence yields, in which we examine the effects of the multiple excitations occurring in these complex interactions, is included.

3.3.2 X-Ray Cross Sections

3.3.2(a) Experimental Data

The determination of cross sections for vacancy production using measured characteristic x-ray yields

has already been discussed for incident protons and alpha particles (see Sec. 2.3.1). The techniques used for heavy ions are essentially the same. A study of the formulation (Merzbacher and Lewis, 1958) conventionally used for determining x-ray production cross sections from x-ray yields in the *thick-target* configuration has recently been made (Taulbjerg and Sigmund, 1972), however, and is shown to be seriously in error in certain cases for incident heavy ions. An additional feature in which the heavy-ion case differs from that for light ions is with regard to fluorescence yields, which can differ from normal values, and can even be bombarding-energy dependent. In some cases, for this reason only cross sections for *x-ray production* are reported, i.e., as distinguished from cross sections for *vacancy production.*

The majority of x-ray measurements have been in the bombarding-energy range of a few tens to a few hundreds of keV, involving proportional counter detection of relatively soft x rays ($h\nu \lesssim 1.5$ keV). A new area being actively investigated involves higher energy ions from tandem Van de Graaffs (ion energies >10 MeV), and the use of solid state x-ray detectors ($h\nu \geq$ a few keV), though primary interest here has been in the effects of multiple excitations on characteristic x-ray energies (see Sec. 3.4, below).

While x-ray production by incident heavy ions ($M > M_\alpha$) was observed much earlier (Coates, 1934; Tanaka and Nonaka, 1937), the first measurements of x-ray production cross sections for incident heavy ions were those of Armbruster (1962). This work was continued by Armbruster *et al.* (1964) and by Specht (1965). Specht's paper describing x-ray production by incident fission fragments elucidated most of the major features discussed to date regarding x-ray production in complex ion–atom collisions. We outline the results of these and later cross section measurements below.

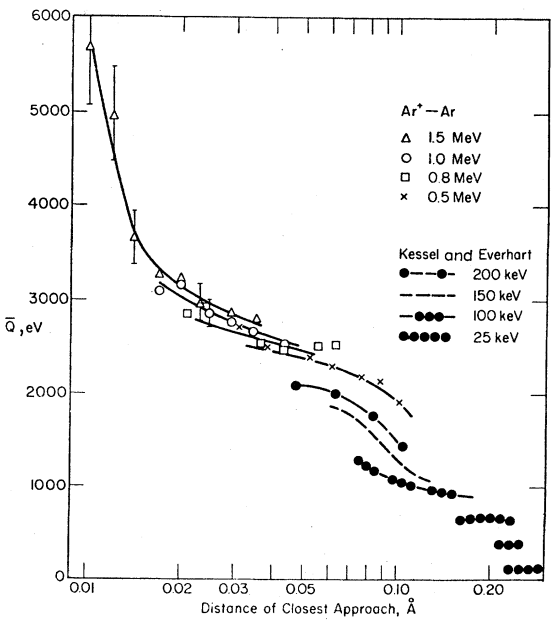

FIG. 3.17. The average inelastic energy loss $\bar{Q}$ is plotted vs the distance of closest approach. The data are from Kessel (1969b) and Kessel and Everhart (1966). [After Kessel (1969b).]

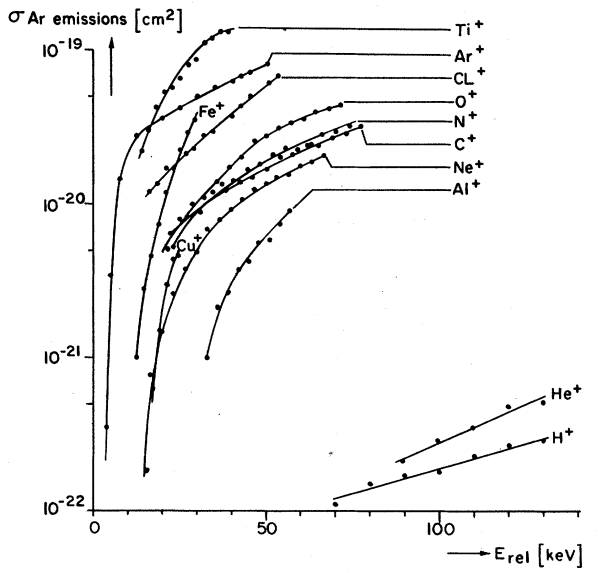

FIG. 3.18. Cross sections for Ar L x-ray production in Ar gas targets for various incident heavy ions, from Saris (1971). Note that the horizontal scale represents incident ion energy in the center of mass system.

Cross section data of Saris and Onderdelinden (1970) and Saris (1971) are unique in that gas targets (Ar and Ne) were used, in a manner such that the targets were "thin" to the incident beam. This eliminates a large source of uncertainty, common to the other measurements, resulting from the difficulties of extracting an x-ray production cross section from the x-ray yield from thick, solid targets (see Sec. 2.3.1). [Note, however, that thick-target data can, in some cases, contain an advantage with regard to fluorescence yields (see Sec. 3.3.5)]. Data from Saris (1971) for Ar L x-ray production in Ar gas targets are shown in Fig. 3.18. Saris and Onderdelinden (1970) have also measured cross sections for K x-ray production in Ne^+–Ne collisions and these data will be discussed later (Sec. 3.3.4).

Thick-target data from the Livermore group are shown in Fig. 3.19 for K-vacancy production in C (Der *et al.*, 1971a), and in Fig. 3.20 for L x-ray production in Cu targets (Kavanagh, *et al.*, 1972). Extensive data on L x-ray production in Cu *ions* have also been collected by Kavanagh *et al.*, for incident Cu ions in the range 100 to 200 keV; results for 160 keV are discussed in Sec. 3.3.6.

Data of Brandt and Laubert (1970) on K-vacancy

TABLE 3.3. Summary of experimental ionization cross sections (in barns) for the K shells of Al and Ne in collision with various atoms. The absolute magnitude of the cross sections are uncertain by ±50%; the relative cross sections are uncertain by ±<25% (from Brandt and Laubert, 1970).

Projectile	Target	Z_1/Z_2	Measured x ray	$\sigma_K(E)=P(E/E_1)^n$, $E_1\leq E\leq E_2$			
				$\sigma_K(E_1)=P$ b	n	E_1 (keV)	E_2 (keV)
$^{7}N_{14}$	$^{13}Al_{27}$	0.54	Al(K)	0.8	3.5	175	300
$^{8}O_{16}$	$^{13}Al_{27}$	0.61	Al(K)	1.2	3.5	175	300
$^{10}Ne_{20}$	$^{13}Al_{27}$	0.77	Al(K)	1.7	3.0	100	3200
$^{18}Ar_{40}$	$^{13}Al_{27}$	1.38	Al(K)	3.1×10^{1}	6.5	175	350
$^{10}Ne_{20}$	$^{13}Al_{27}$	0.77	Ne(K)	6.0×10^{2}	2.7	100	400
$^{10}Ne_{20}$	$^{10}Ne_{20}$	1.00	Ne(K)	1.0×10^{5}	3.7	100	200
$^{10}Ne_{20}$	$^{6}C_{12}$	1.67	Ne(K)	2.3×10^{1}	1.9	125	300

production in Al and Ne are summarized in Table 3.3. These are all thick-target data, and use ordinary fluorescence yields in the conversion from x-ray production cross sections. (Data for Ne targets were obtained from Ne implanted in Al.)

Higher energy, *thin-target* data from Sakisaka (1971), on Al K-shell cross sections for incident C^+, N^+, and O^+, are shown in Fig. 3.21. Data from Brandt and Laubert (Table 3.3), and also from Needham and Sartwell (1970a) are shown in Fig. 3.21, for comparison; the two sets of lower-energy data do not agree very well, and the Brandt and Laubert curves appear to be in better accord with those of Sakisaka. Needham and Sartwell have also obtained cross sections for Al K-shell excitation in Ar^{2+}–Al collisions that are one to two orders of magnitude larger than those of Brandt and Laubert for Ar^{+}–Al collisions in the same energy range.

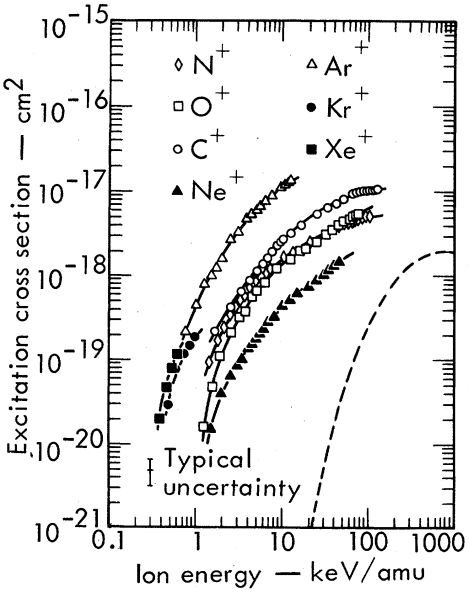

FIG. 3.19. Carbon K-shell excitation cross sections as a function of incident ion energy per atomic mass unit, from Der *et al.* (1971a), for solid targets. The dashed curve is for incident protons. The data for Kr^+ and Xe^+ may be only order of magnitude estimates due to the recoil effect in thick, solid targets (Taulbjerg and Sigmund, 1972). The data assume a value 0.00113 for the fluorescence yield.

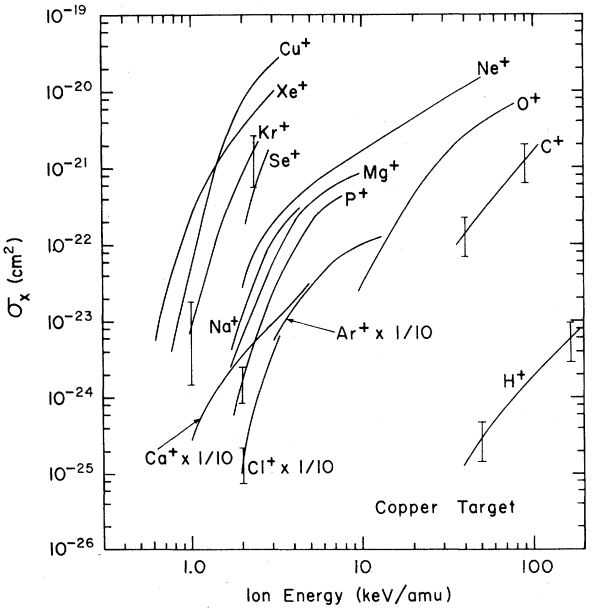

FIG. 3.20. Cross sections for L x-ray production in Cu for various heavy ions incident on thick Cu targets, as a function of ion energy per amu. The data for incident Xe^+ and perhaps also Kr^+ and Se^+ may be in error due to the recoil effect in solid targets (Taulbjerg and Sigmund, 1972). The Cu data are from Kavanagh *et al.* (1972).

The reasons for these discrepancies are not understood; it is not expected that the different initial charge states of the ions in the two measurements could be responsible, especially for solid targets. Further duplication of measurements of this kind, particularly where thick targets are involved, is clearly desirable.

Data of Terasawa, Tamura, and Kamada (1971) for K-shell ionization of Be are reproduced in Fig. 3.22. These workers have also measured cross sections for C K-shell ionization using the same ion beams; preliminary data (Terasawa, 1971) indicate possible systematic disagreement with Der *et al.* (1971a).

Data on M-shell excitation of Hf have been presented by Needham and Sartwell (1970a), for N^{2+}, O^{2+}, and Ar^{2+} ions in the energy range 70–400 keV. Cross sections for M x-ray production in Sb in ~85–130 keV Kr^{+}–Sb collisions have been published by Nelson, Cairns, and Blamires (1970). Both of these are thick-target measurements.

Cross-section data for collisions at much higher energies are shown in Figs. 3.23–3.25. Figure 3.23 from Specht (1965) represents target atom excitation by incident fission fragments. (Specht also shows similar data on L-shell excitation of the projectiles. The data are all from thick targets.) Figure 3.24 shows cross sections for K x-ray production in Al, Ca, and Cu by 7.5–40.0 MeV O ions (Burch and Richard, 1971). In Fig. 3.25 we reproduce data of Stein *et al.* (1972) on L x-ray production in I–Te collisions for I ions in the range ~18–60 MeV. [Stein *et al.* (1970) have also quoted cross sections of 2.0×10^{-19} and 5.5×10^{-18} cm², respectively, for producing L vacancies in I, and M vacancies in Yb, for 30-MeV I–Yb collisions.] The measurements of Burch and Richard, and those of Stein *et al.*, were for thin targets.

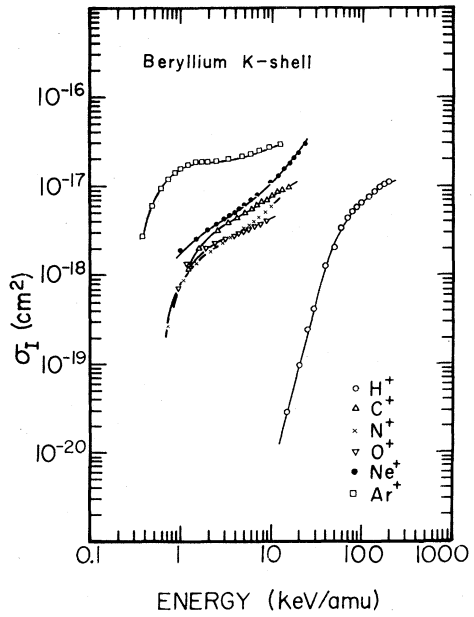

FIG. 3.22. K-shell excitation cross sections for Be for various incident ions. Data are from Tarasawa, Tamura, and Kamada (1971).

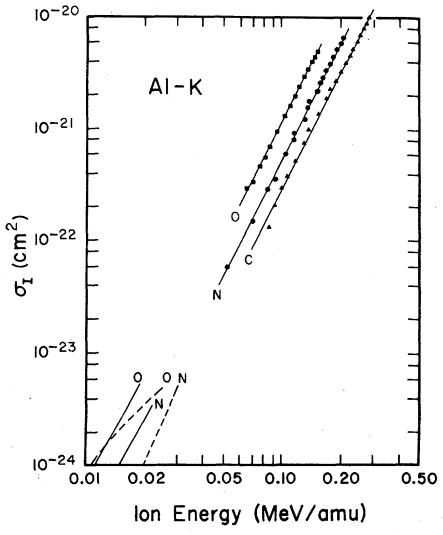

FIG. 3.21. Cross sections for Al K-shell excitation for incident C, N, and O ions. The plotted points are from Sakisaka (1971) for *thin* targets and the solid and dashed curves in the lower left are thick target data from Brandt and Laubert (1970) and Needham and Sartwell (1970a), respectively.

3.32(b) Discussion

A clear indication of the general disparity between the heavy-ion data and the predictions of theories applicable to incident point charges (e.g., protons) is given in Fig. 3.26. Here we have plotted most of the data for K shells in terms of the reduced parameters $u^2\sigma_I/Z_1^2$ and $E/\lambda u$ (where u is the binding energy of the K electron being excited and λ is the ratio of the incident ion mass to the electron mass). As shown in Sec. 2.3 this kind of plot quite successfully collapses the proton and alpha-particle data to a single curve; this universal curve is shown as a solid line in Fig. 3.26. Clearly the model is not successful for heavy ions: At lower ion velocities, the experimental cross sections are, in general, much too large. (The use of a screened nuclear charge in the ordinate, instead of simply Z_1, would *raise* the plotted points. Also, inclusion of a "binding correction," i.e., a correction for adiabatic effects, in the binary encounter model would *lower* the theoretical curve for lower ion velocities.) It is interesting that the data for incident O ions appear to fall on a common curve for the Al, Ca, and Cu targets. The data for heavier ions show a much flatter velocity dependence, except at very low velocities, and tend toward the O

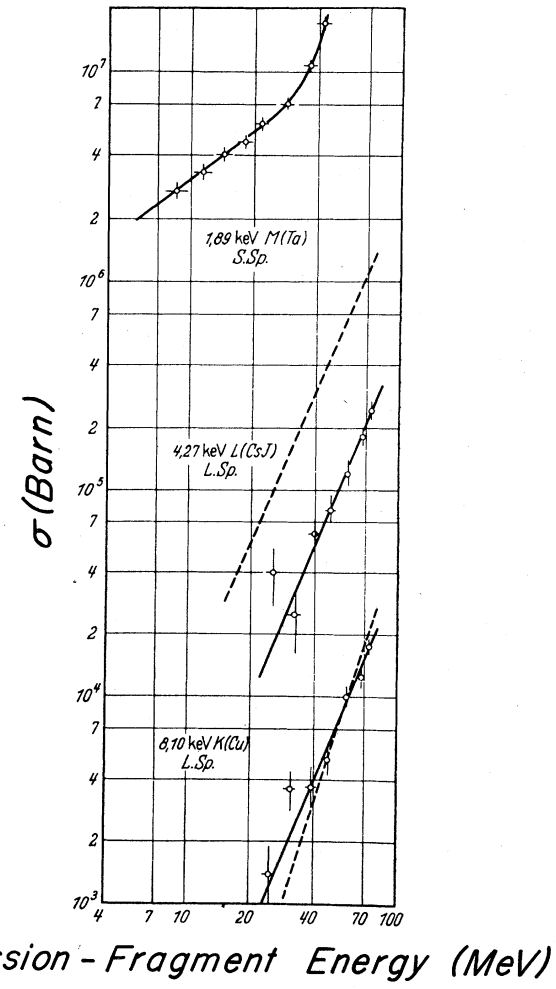

FIG. 3.23. Cross sections for the excitation of the Cu K shell and CsI L shells by light fission fragments and the M shell of Ta by heavy fission fragments. Dashed curves are Born approximation predictions. [After Specht (1965).]

data at higher velocities. The O data are in qualified agreement (see Sec. 2.3) with the binary encounter theory. Thus, at least insofar as K-shell cross sections are concerned and for the collisions considered here, the O ion is apparently like a point charge.

A similar plot, showing representative L- and M-shell data is presented in Fig. 3.27. We have excluded the extensive data of Saris and Onderdelinden (1970) and Saris (1971) on Ar L-shell excitation because of the large uncertainty in fluorescence yield values for the Ar L-shell in such heavy-ion interactions. These effects will be discussed in Sec. 3.3.5. We have, however, included data for the Ar^{+}–Ar system based on Auger electron measurements. As for the K-shell case most of the experimental cross sections are greatly in excess of theoretical values for an incident point charge. (The use of the actual projectile Z instead of a screened value in the vertical scale parameter again places a lower limit on the discrepancies; the screening effect would be even larger in these cases than in the K-shell case.) The available data for L shells extend to much lower values of $E/\lambda u$ than do those for the K-shell case, and the data show rapidly rising cross sections at these low relative velocities, followed by a less gradual velocity dependence as seen in most of the K-shell data; this thresholdlike effect is seen in some of the K-shell curves.

The plots in Figs. 3.26 and 3.27 serve to illustrate another aspect of the heavy-ion data. The parameter $E/\lambda u$ is equal to $(v_0/v)^2$, where v_0 is the incident ion velocity, and v is the orbital velocity of the electron being excited, and thus provides a criterion for the applicability of molecular-orbital concepts (see Sec. 3.1). Deviations of cross sections from direct scattering theory persist for $E/\lambda u$ as large as 0.1, suggesting that quasiadiabatic effects are important for ion velocities as large as about one-third the relevant electron velocity. The only data that exist for $E/\lambda u > 0.1$ are for Al, Ca, and Cu K-shell excitation by O ions (Burch and Richard, 1971) and for the C K shell (Der *et al.*, 1971a). It is important that more data be obtained for $E/\lambda u \gg 0.1$ to see if the heavy-ion data do indeed merge with the expectations for protonlike projectiles.

The classification above of the O-ion data of Burch and Richard (1971) with protons and alpha particles rather than with heavy ions relates to the concept of "level matching" that will be discussed in Sec. 3.3.6. For these data the poor level matching leads to quasiadiabatic effects on the target-atom K shell that amount simply to an increase in binding energy, with a resultant decrease in the direct-excitation cross section (see Sec. 2.5).

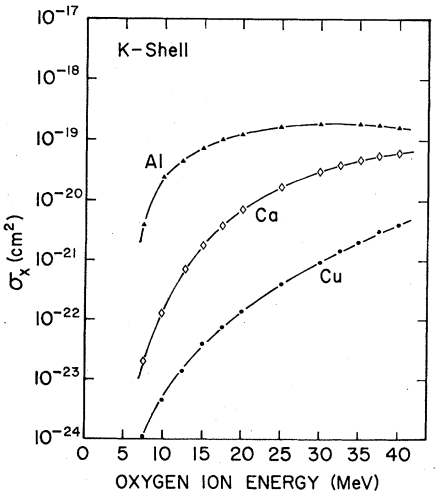

FIG. 3.24. Cross sections for K x-ray production in Al, Ca, and Cu by incident O ions, from Burch and Richard (1971). Data are for thin targets.

3.3.3. Auger Electron Cross Sections

Cross sections for the emission of Auger electrons from Ar^+–Ar and Ne^+–Ne collisions have been presented by Cacak, Kessel, and Rudd (1970) for collision energies from 50 to 300 keV. While earlier Auger studies (Snoek *et al.*, 1965; Rudd, Jorgensen, and Volz, 1966) provided striking confirmation of the Fano and Lichten molecular-orbital model, essentially all earlier cross section data were based on x-ray measurements (see previous section). In addition to the data of Cacak, Kessel, and Rudd, preliminary cross-section data have been presented by Ogurtsov (1971) and Fastrup and Larsen (1971). All the Auger data that will be discussed are for collision velocities such that $E/\lambda u \lesssim 10^{-2}$; thus the collisions may be considered to be quasiadiabatic, and the molecular-orbital point of view is appropriate.

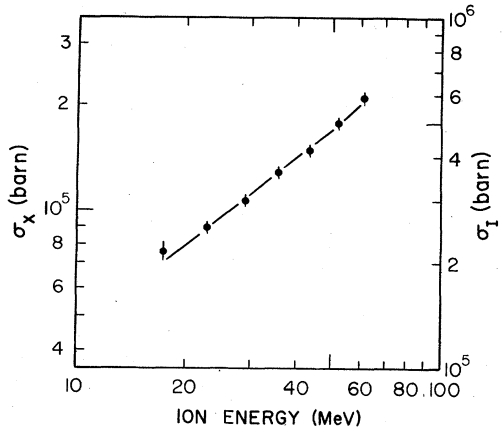

FIG. 3.25. Cross sections for L x-ray production (left-hand scale) and L-shell vacancy creation (right-hand scale) in the I–Te collision system, as a function of incident I ion energy. Data are from Stein *et al.* (1972), and are for thin Te targets.

The cross-section data of Cacak, Kessel, and Rudd (1970) were obtained from the absolute doubly differential cross sections of Cacak and Jorgensen (1970). (For a general description of experimental procedures, see Secs. 2.3.2 and 2.4.1.) While the energy resolution of the electron spectrometer was purposely made low for these experiments, the apparatus was similar to that used to obtain the high-resolution spectral data discussed in Sec. 3.4.2, below. The low-resolution system is described in detail by Cacak (1969). Electron energy spectra are shown in Fig. 3.28 for the Ar^+–Ar system. A prominent peak appears at an electron energy of about 190 eV due to Auger emission following vacancy creation in the Ar L-shell. [The dashed lines in the figure represent statistical calculations made according to the prescriptions of Bierman *et al.* (1970) and Russek and Meli (1970). While these curves show qualitative agreement with the continuum portion of the spectrum, they do not show the ~190 eV peak or the prominent low-energy component. These features were predicted by Fano and Lichten on the basis of their molecular-orbital model.] The analogous K-shell Auger peak for Ne^+–Ne collisions is shown by Cacak (1969).

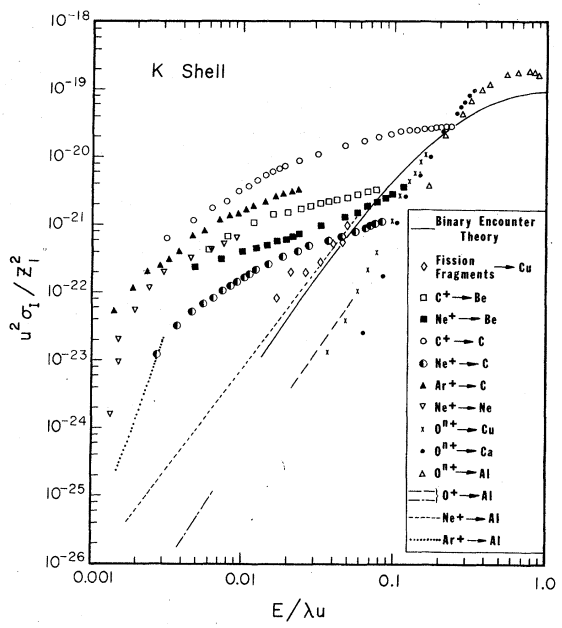

FIG. 3.26. Cross sections for K-shell excitation by incident heavy ions plotted in terms of the reduced parameters used in the binary encounter theory (Garcia, 1970; see Fig. 2.3 for a similar plot for incident protons). E and u are, respectively, the ion energy and the K electron binding energy, λ is the ratio of the projectile to electron mass, and Z_1 is the projectile atomic number. All the data are based on x-ray measurements except those for Ne^+–Ne, which contain some Auger-electron data (see Sec. 3.3.3). For all the asymmetric collisions the x rays were from the target atom. The solid curve represents binary encounter theory.

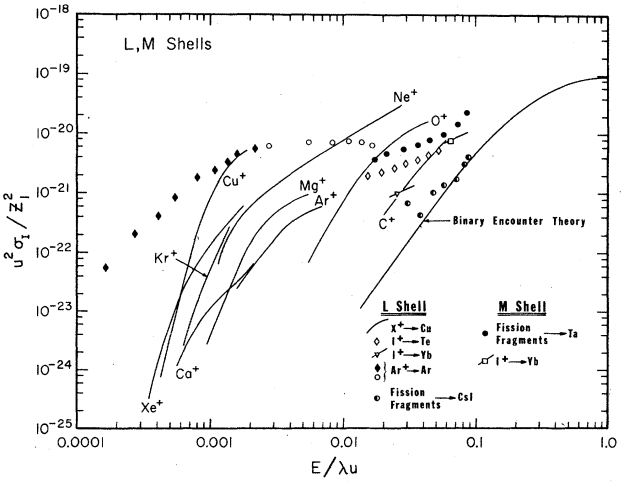

FIG. 3.27. A plot similar to that in Fig. 3.26 for L- and M-shell excitation. The data for Ar^+–Ar are from Auger electron measurements (see Sec. 3.3.3).

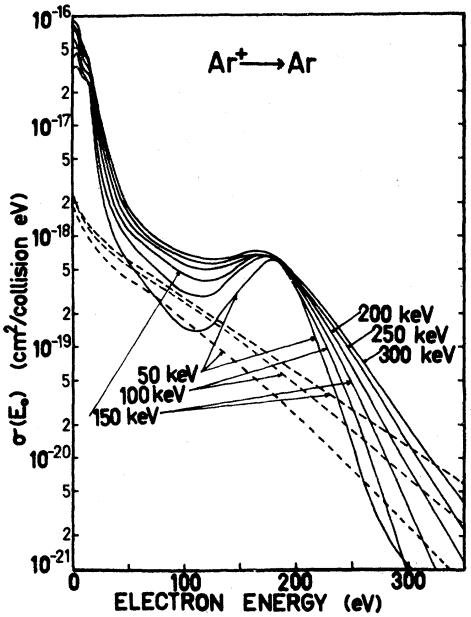

FIG. 3.28. Energy spectra, integrated over all angles, of electrons emitted in Ar^+–Ar collisions. The dashed lines in the figure represent statistical model calculations (see text). The figure is from Cacak and Jorgensen (1970), and the different curves are for different ion energies.

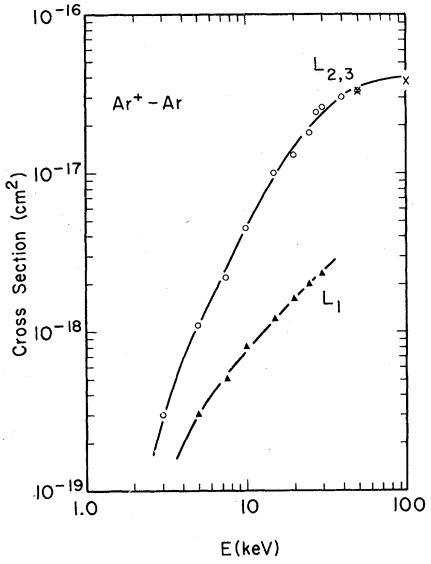

FIG. 3.30. L-shell excitation cross sections from Auger measurements of Ogurtsov (1971) for the Ar^+–Ar system. Data were normalized to those of Cacak, Kessel, and Rudd (1970) at 50 keV. Crosses at 50 and 100 keV are from Cacak *et al.*

The total cross sections for Auger emission are plotted as a function of ion energy in Fig. 3.29. The solid curves are based on a simple level-crossing model, for parameters indicated on the Figure; this model will be discussed in the following section. Striking features of the data in Fig. 3.29 are the flatness of the Ar Auger cross-section curve, and the difference in the energy dependence of x-ray and Auger data in the region where they overlap (see Sec. 3.3.5).

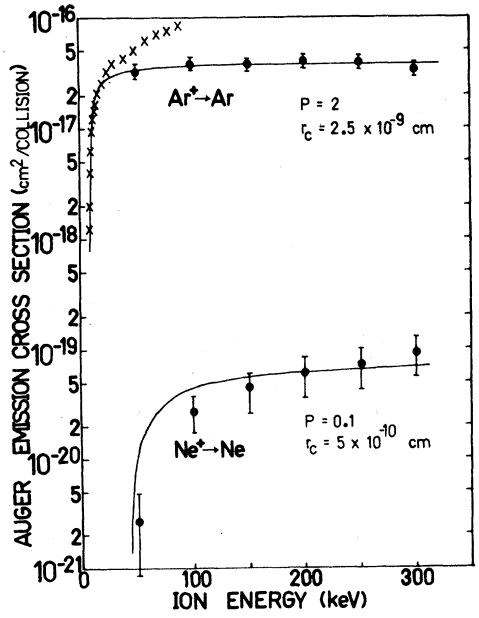

FIG. 3.29. Auger emission cross sections for Ar and Ne symmetric collisions (solid circles). Crosses are x-ray results of Saris and Onderdelinden (1970) normalized at 20 keV to the solid (theoretical) curve for Ar. The theoretical curves were generated using a simple model based on level crossings, for fitting parameters shown on the figure; the model is discussed in Sec. 3.3.4. [After Cacak, Kessel, and Rudd (1970).]

Ogurtsov (1971) reports cross sections for $L_{2,3}$- and L_1-shell excitation of Ar in Ar^+–Ar collisions for ion energies in the range 2.5–50 keV. The data, shown in Fig. 3.30, were obtained by normalizing the $L_{2,3}$ cross sections to those of Cacak, Kessel, and Rudd at 50 keV.

Fastrup and Larsen (1971) studied K Auger-electron production in collisions of C^+, N^+, O^+, and Ne^+

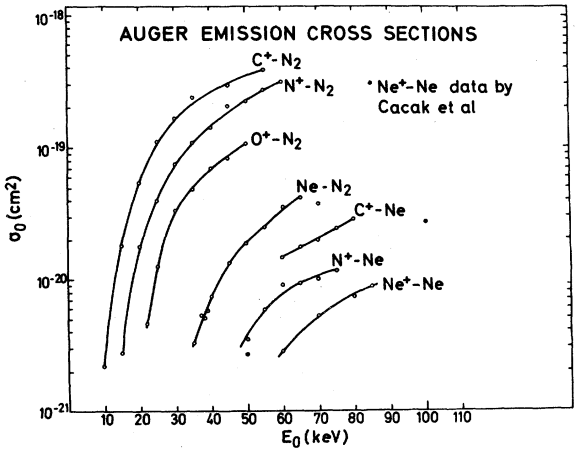

FIG. 3.31. Cross sections for K-Auger production from Fastrup and Larsen (1971). The solid circles at 50 and 100 keV are Ne^+–Ne data of Cacak, Kessel, and Rudd (1970). For the asymmetric collision systems the K-shell vacancies were observed to be in the partner of lower Z.

with Ne and N targets, in the bombarding energy range 10–85 keV. Data are shown in Fig. 3.31. (A detector efficiency of 100% was tentatively assumed for calculating cross sections. A comparison of their Ne^+–Ne data with 50 and 100 keV points from Cacak, Kessel, and Rudd leads the authors to speculate that their detection efficiency may have been as low as 50%.) The experiments showed that the K-shell vacancies were produced in the lower-Z partner of the colliding particles, in agreement with molecular-orbital considerations. (See Secs. 3.2.3 and 3.3.6). For the same velocities Ne^+–N_2 collisions are about ten times more efficient in the production of N K Auger electrons than are N^+–Ne collisions. This demonstrates the influence of vacancies in Ne outer shells in the promotion process; similar effects are discussed in connection with the scattering experiments in Sec. 3.2.3(b)2.

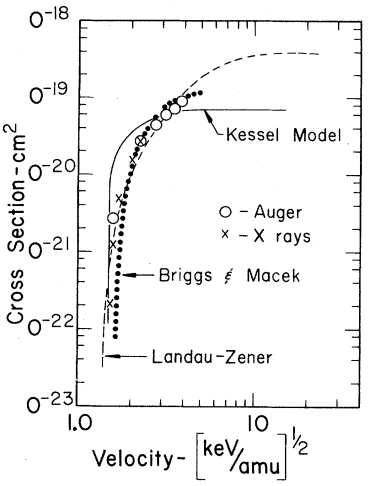

FIG. 3.32. Cross sections for K-shell excitation in Ne^+–Ne collisions as a function of incident ion velocity. The Auger data are from Cacak, Kessel, and Rudd (1970) and the x-ray data are from Saris and Onderdelinden (1970). The x-ray results were normalized to the Auger data at 100 keV. The solid dots show predictions of the theory of Briggs and Macek (1972). The dashed curve is from the Landau–Zener model using $\alpha=0.25$, $y=$ 1.43 a.u. and r_x equal to twice the Ne K-shell radius and assuming a screened Coulomb potential, and the solid curve represents the Kessel model as applied in Fig. 3.30 by Cacak *et al.*

3.3.4 Comparison with Theoretical Models

There are several models based on molecular-orbital concepts (see Sec. 3.1) that are useful for estimating cross sections and that have received attention in the literature; they will be discussed briefly here. One of these, that of Briggs and Macek (1972), is an *ab initio* treatment of interactions in which rotational coupling between molecular orbitals provides the excitation mechanism. Two others, due to Kessel (1969c) and Fortner *et al.* (1969), involve less rigor (either in the basic structure or in the manner in which the model is applied) but both nevertheless provide useful parameterizations of experimental data.

The total cross section for creation of an inner-shell vacancy can be represented by the integral

$$\sigma=2\pi\int_0^\infty P(b)b\,db, \qquad (3.17)$$

where b is the impact parameter, and $P(b)$ is the probability of vacancy production. The calculational models discussed below differ in their determination of the function $P(b)$. Briggs and Macek (1972) obtain a result for $P(b)$ for K-vacancy production in Ne^+–Ne collisions by explicitly treating rotational coupling between the $2p\sigma$ and $2p\pi$ molecular orbitals. The calculations involve an extension to the many-electron system of the one-electron formalism of Bates and Williams (1964). Energies of the $2p\sigma$ and $2p\pi$ orbitals for the Ne^+–Ne system were taken from the calculations of Larkins (1972). Briggs and Macek plot their calculated probabilities for single-electron transfer between orbits for three different collision velocities, and the relationship of these fundamental probabilities [designated as $P(b)$ by Briggs and Macek] to the many-electron probability $P(b)$ in Eq. (3.17) is obtained from straightforward statistical arguments. The curves show peaked structure, with zero probability indicated for $b=0$ and for b greater than twice the Ne K-shell radius. Calculations are performed for both Coulomb and straight line trajectories; the Coulomb deflection is found to be essential in reproducing the thresholdlike behavior in the experimental cross sections. We compare the Briggs and Macek calculations with the experimental Ne^+–Ne cross sections in Fig. 3.32; the agreement is very encouraging, and more work of this general type is required. Regarding extension of their results to other collision systems, Briggs and Macek suggest an approximate scaling law for estimating K-shell excitation in other symmetric cases. (We have attempted to scale the Ne result to the C^+–C system, as suggested; in the restricted energy range of the calculation, the experimental results show a much faster rise with increasing energy than do the calculations. The reasons for this are not understood.)

The formula of Fortner *et al.* (1969) results from Eq. (3.17) if one uses for $P(b)$ the probability calculated by assuming a discrete level crossing, the Landau–Zener theory of level crossing, and classical paths for the nuclear motion (Mott and Massey, 1965). Thus, we have

$$\begin{aligned} P(b)&=2\alpha p(1-p) \qquad b<b_m,\\ &=0 \qquad\qquad\quad b>b_m, \end{aligned} \qquad (3.18)$$

where α is a statistical factor similar to that discussed by Briggs and Macek, b_m is the impact parameter such that the distance of closest approach just equals the level-crossing radius r_x, and p is the probability of a transition at each passage of the crossing. The expression for p that is used in this treatment is the Landau–Zener form (see Mott and Massey, 1965), i.e.,

$$p=\exp\left[-(y/v_x)\right], \qquad (3.19)$$

where v_x is the radial velocity at r_x, and y is related to the coupling between the states and to the slopes of the orbitals at the crossing. As shown by Fortner *et al.*

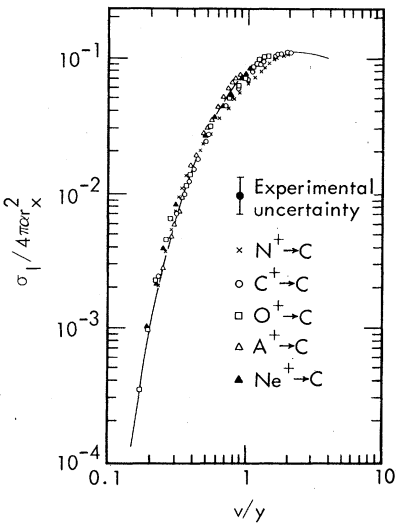

FIG. 3.33. Comparison of C K-shell excitation cross sections as a function of ion velocity (Der *et al.* 1971a) with a theoretical model based on the Landau-Zener formula. The quantities αr_x^2 and y are fitting parameters, though good fits are obtained for $\alpha=1$ and r_x equal, roughly, to the sum of the C K-shell radius and the radius of the shell in the projectile whose binding energy most closely matches the C K-shell binding energy.

(1969), the cross section has the final form:

$$\sigma(E)=4\pi\alpha r_x^2[1-V(r_x)/E] \times\left\{Q_3\left[y\Big/\left(\frac{2}{\mu}[E-V(r_x)]\right)^{1/2}\right] -Q_3\left[2y\Big/\left(\frac{2}{\mu}[E-V(r_x)]\right)^{1/2}\right]\right\}, \quad (3.20)$$

where

$$Q_n(x)=\int_1^\infty \exp(-xt)t^{-n}\,dt,$$

E is the ion energy in the CM system, μ is the reduced mass for the two-atom classical problem, and $V(r)$ is the potential energy. For $E\gg V(r_x)$, Eq. (3.20) reduces to

$$\sigma(E)=4\pi\alpha r_x^2[Q_3(y/v)-Q_3(2y/v)], \quad (3.21)$$

where v is the relative velocity at infinite distance of separation.

The Kessel expression is obtained if, in Eq. (3.17), we choose $P(b)$ to be a constant independent of v_x for $b<b_m$, and zero for $b>b_m$. Then the cross section is simply

$$\sigma(E)=\pi r_x^2 P[1-V(r_x)/E], \quad (3.22)$$

where P is some constant. The Kessel assumption for $P(b)$ was empirically based on Ar^+–Ar scattering data (see Fig. 3.4), in which two $2p$ electrons of Ar are promoted with essentially unit probability for distances of closest approach less than some critical value.

While the Landau–Zener formulation as outlined above is fundamentally valid, it has been fairly widely applied outside the range of its validity. It has been shown by Der *et al.* (1971a), Terasawa, Tamura, and Kamada (1971), and Terasawa (1971) that measured cross sections for K-shell excitation of C and Be by various ions can be fitted remarkably well by this model. The C data of Der *et al.* are compared with the theory in Fig. 3.33 and the agreement is within experimental errors for all the data, including both symmetric and asymmetric collisions over a broad range of collision velocities. (See also the fit to the Ne^+–Ne data in Fig. 3.32.) The Landau–Zener probability [Eq. (3.19)], however, contains only *radial* momentum coupling, whereas the $2p\sigma$–$2p\pi$ interaction that produces K-shell excitation involves *rotational* coupling. Thus, while use of the Landau–Zener formalism is not valid, Eq. (3.19) apparently contains the correct velocity dependence over the range of b values that makes the major contribution to the cross section.

The Kessel formulation has already been shown (Fig. 3.29) to be in excellent agreement with data of Cacak, Kessel, and Rudd (1970) on L-shell excitation in Ar^+–Ar collisions. At lower energies, however, the model shows a much steeper energy dependence than do the experimental results of Ogurtsov (1971). While Kessel's assumptions regarding $P(b)$ constitute an oversimplification, the Ar data support the approach, and underline the need for a different formalism, in that case, than is appropriate for K-shell excitation. Perhaps the clearest experimental indication of different probability distributions for the L-shell and K-shell cases comes from the scattering experiments. Explicit data on excitation probabilities $P(b)$ can be obtained from a simple kinematic transformation of the data in Figs. 3.4 and 3.11 for Ar L and Ne K excitation. The differences for the two cases lead to the "triple" and "double" peaked structures, respectively, that are seen in the energy-loss data. (See Sec. 3.2.)

The apparent requirement of markedly different formalisms for the K-shell and L-shell cases can be understood from an examination of the molecular levels involved (Fig. 3.1). The K-shell case is quite logically interpreted in terms of a two-level formulation so long as the requirement for quasi-adiabaticity is met. The creation of L-shell vacancies in Ar^+–Ar collisions, however, involves the $4f\sigma$ MO which rises very steeply from a level characterized by the $2p$ level of Ar (245 eV) to a level characterized by the $4f$ level of Kr (<1 eV). The proper graphical representation of such a level should perhaps be a broad line, with the breadth determined by the product of velocity and $dE(r)/dr$. The $4f$ level of Kr is near the ionization limit and thus is close to a continuum of other atomic levels. It is just these two factors, the large time derivative and the close proximity to other levels, which lead to mixing through nonadiabatic terms. Thus, for sufficiently small values of b and for sufficiently large velocities

this coupling to the continuum can result in essentially unit probability of emptying the $4f\sigma$ level. This is consistent with the basic assumption regarding $P(b)$ in the Kessel model. For somewhat larger values of b or somewhat smaller velocities leading to distances of closest approach smaller than, but near the first crossing radius of the $4f\sigma$ level, a two-level formalism might be expected to apply even for the Ar^+–Ar case, and smaller transition probabilities would be expected.

We expect K-shell excitations to be reasonably well approximated by a two-level formalism, so long as the incident energy is small enough to assure adiabaticity. The L-shell and higher orbitals, on the other hand, particularly the $4f\sigma$ level, change so rapidly as a function of internuclear distance that the nonadiabatic terms become important at much smaller velocities.

Cacak, Kessel, and Rudd (1970) have attempted to fit their Ne^+–Ne K-shell data with the Kessel model (see Fig. 3.30). Their Auger electron data, however, continue to rise with increasing incident-ion energy, at variance with the assumption of constant probability of vacancy production. Their Ne data and their fit based on constant probability (Kessel model) are shown in Fig. 3.33, where we also show the x-ray data of Saris and Onderdelinden (1970). This figure includes results from the Briggs and Macek and the Landau–Zener calculations, and it appears that the data agree less well with the constant probability curve, consistent with the above discussion.

The important coincidence measurements of Stein *et al.* (1970, 1972) are relevant to the above discussion, because they provide $P(b)$ directly. These workers have studied L-vacancy production in the near-symmetric I–Te collision for $E/\lambda u$ values in the range 10^{-2}–10^{-1}, and have explicitly determined the relationship between vacancy production probability and impact parameter for electron promotion via the $4f\sigma$ MO (as in the Ar–Ar case). As indicated in Fig. 3.34, they find a substantially different behavior from the velocity independent step function that appears to be appropriate to the Ar–Ar data: (i) The probability of vacancy production increases smoothly with decreasing b (designated ρ in the figure). No sudden rise of vacancy production is observed, (ii) The maximum number of vacancies created in both particles is appreciably smaller than 2, and (iii) The probability is apparently energy dependent. The differences between the Ar–Ar and I–Te systems can be qualitatively understood in terms of MO concepts. Stein *et al.* point out that the $4f\sigma$ MO rises less steeply for their system than for Ar–Ar. Furthermore, for smaller ion velocities, the levels crossing with the $4f\sigma$ are filled, except possibly the one involving rotational coupling at small b where the $4f\sigma$ MO merges with other $4f$ MO's. Thus, in terms of the arguments made earlier in this section, it is reasonable that the I–Te L-shell case should differ from that for Ar–Ar, and should, in fact, exhibit features like those discussed for K-electron promotion. The lower curves in Fig. 3.34 indicate maxima in the differential cross section for distances of closest approach corresponding roughly to the radius of the maximum in the radial charge density for the $2p$ state in I or Te.

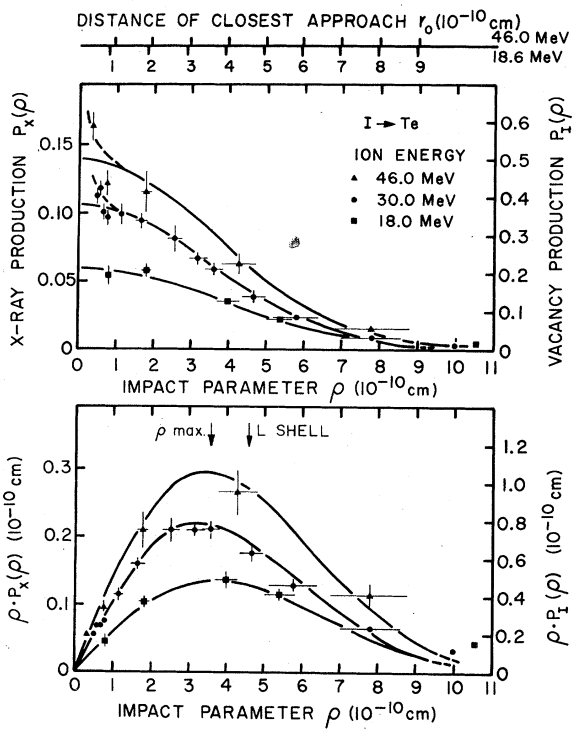

FIG. 3.34. *Top*: L x-ray production probability in the I–Te system (left-hand scale) as a function of the impact parameter ρ. For comparison, the distance of closest approach r_0 is indicated. The right-hand scale gives the L-vacancy production, assuming a fluorescence yield of 0.14. *Bottom*: $\rho P_x(\rho)$ as a measure of the differential cross section for L x-ray production (left-hand scale); it shows a maximum at ρ values comparable to the L-shell radius. Data are from Stein *et al.* (1972).

3.3.5 *A Comparison of Auger and X-Ray Cross Section Data: Fluorescence Yields in Heavy-Ion–Atom Collisions*

Cross sections for inner-shell vacancy production leading to x-ray and Auger-electron emission have been discussed in Sec. 3.3.2 and 3.3.3. Because x-ray emission is a relatively rare occurrence for the cases discussed, the electron measurements, where available, directly provide cross sections for vacancy production. The determination of vacancy-production cross sections from x-ray measurements, however, requires a knowledge of the fluorescence yield for the shell being considered, and for these complex collisions the usual tabulated values (e.g., Bambynek *et al.* 1972) may not be appropriate. The outer-shell excitations and ionizations that accompany the inner-shell processes can, in certain cases, substantially affect fluorescence yields for the inner shell.

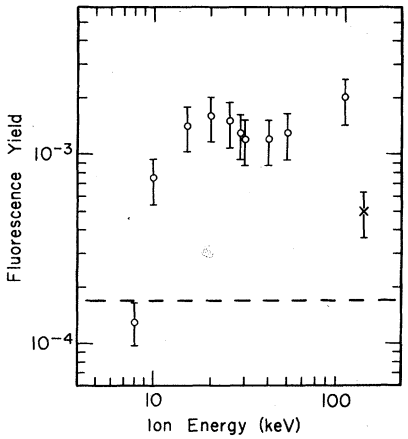

FIG. 3.35. Argon L-shell fluorescence yields in Ar–Ar collisions, as a function of ion energy. The circles are ratios of measured x-ray cross sections (Saris and Onderlinden, 1970) to Auger cross sections (Ogurtsov, 1971; Cacak, Kessel, and Rudd, 1970). The cross represents a value for 125-keV proton bombardment of Ar (Saris and Onderdelinden) and the dashed horizontal line is a theoretical value for the neutral atom from Walters and Bhalla (1971b).

The first experimental evidence of a dependence of fluorescence yield on collision energy was provided by Saris and Onderdelinden (1970), who compared their L x-ray cross sections for Ar^+–Ar collisions with the electron data of Cacak, Kessel, and Rudd (1970). Recent new measurements of electron cross sections for Ar^+–Ar (Ogurtsov, 1971) enable us to extend these data to lower energies. The ratio of the x-ray cross sections from Saris and Onderdelinden (1970) to the electron cross sections of Ogurtsov (1971) and Cacak, Kessel, and Rudd (1970) is plotted in Fig. 3.35 for the energy range in which the measurements overlap (8–100 keV). It is seen that ω_L increases by an order of magnitude as the collision energy goes from 8 to 15 keV, and then changes more slowly, with an indication of a minimum at about 35 keV. Larkins (1971b) has shown (see below) that these experimental results can easily be accounted for in terms of multiple-vacancy production in the collisions. While the Ar ω_L studies emphasize the problems in relating x-ray data to vacancy production, other data indicate that the Ar L shell constitutes a rather extreme example.

Experimental data on K-shell fluorescence yields can be obtained, for a solid target, from a comparison of C K x-ray results for N^+–C collisions in graphite targets (Der *et al.*, 1971a) with electron data for C^+–N collisions (Fastrup and Larsen, 1971). This comparison yields ω_K values for C for the N^+–C interaction in the rather narrow energy range 1.4–4.6 keV/amu. The Auger data constitute direct measurement of cross sections for K-vacancy production in C, independent of details of outer-shell configurations, because ω_K is negligible compared to unity. The fact that Fastrup and Larsen investigate C^+–N rather than N^+–C is not expected to be important insofar as the vacancy production is concerned—though such details of initial charge state *are* important when closed shells are involved, e.g., Ne^+–N vs N^+–Ne. If the electron data are normalized (as suggested by the experimenters) to agree with Cacak *et al.*, one obtains a roughly constant value of ω_K for the graphite target, in good agreement with the atomic value of 1.13×10^{-3} (Dick and Lucas, 1970) used by Der, *et al.* in their cross section calculations. [Note the discrepancy between this value and the one obtained for protons by Toburen (1972); see Sec. 2.3.2]. This apparent insensitivity of ω_K for C to the outer-shell perturbations expected in heavy-ion collisions is probably due to solid state effects, as suggested by Der *et al.* (1971a); since in the solid the outer shell of C is part of the valence band, outer-shell defects are expected to have very short relaxation times. For elements somewhat heavier than C—e.g., Ne—calculations like those to be discussed below indicate a *general* insensitivity of ω_K values to outer-shell defects.

Fluorescence yields for multiple-defect configurations were calculated by Larkins (1971b), and more recently by Fortner *et al.* (1972), by simply correcting ground-state Auger and x-ray transition rates for changes in populations of outer shells. The method assumes that the overlap of the wave functions is not affected in the defect configuration but that only the populations of the relevant atomic states are changed.

The Larkins data are reproduced in Tables 3.4 and 3.5, for ω_L and ω_K, respectively, for various defect configurations in Ar. The data show that ω_L increases rapidly with removal of $3p$ electrons; this is easily understood since $3p$ electrons dominate in filling $2p$ holes via the Auger effect but are not involved in radiative transitions ($2s$ vacancies are not considered since they are assumed to be rapidly transferred to the $2p$ level by Coster–Kronig transitions). Creation of a $3s$ vacancy causes a relatively small *decrease* in ω_L unless large numbers of $3p$ electrons are also missing, in which case ω_L is increased; this is consistent with the requirement for $3s$ electrons in radiative transitions and for *at least* 2 M-shell electrons for nonradiative decay. Table 3.5 shows that ω_K for Ar is relatively insensitive to removal of $2p$ *or* $3p$ electrons, since $2p$ and $3p$ electrons are involved in *both* x-ray and Auger transitions.

TABLE 3.4. Estimated changes in $\omega_{L_{2,3}}$ for various vacancy configurations of the Ar atom (from Larkins, 1971b).

Atomic configuration	$\omega_{L_{2,3}}\times10^4$	Atomic configuration	$\omega_{L_{2,3}}\times10^4$
$[2p]$	1.9	$[2p, 3s]$	1.1
$[2p, 3p]$	2.7	$[2p, 3s, 3p]$	1.6
$[2p, 3p^2]$	4.1	$[2p, 3s, 3p^2]$	2.5
$[2p, 3p^3]$	6.9	$[2p, 3s, 3p^3]$	4.3
$[2p, 3p^4]$	14.0	$[2p, 3s, 3p^4]$	10.9
$[2p, 3p^5]$	40.0	$[2p, 3s, 3p^5]$	53.9
$[2p, 3p^6]$	151.0	$[2p, 3s, 3p^6]$	10^4

The calculations of Fortner *et al.* (1972) are for the Cu L-shell, and give ω_L values that are relatively insensitive to moderate amounts of outer-shell excitation. Results for Cu are compared with those for Ar in Fig. 3.36. The outer-shell configurations were produced by sequentially removing the most weakly bound electrons. The results are quite different for the two cases. Whereas the L-shell fluorescence yield for Ar increases rapidly for even a small number of M-shell vacancies, the copper fluorescence yield remains essentially constant for up to six M-shell vacancies, and then *decreases* until ten M-shell vacancies are produced. After ten M-shell vacancies, the Cu fluorescence yield begins to rise like that of Ar.

The reason for the difference between the two cases is quite clear. As already pointed out, removal of outer ($3p$) electrons from Ar has a strong affect on Auger rates, but does not affect x-ray rates since the principal L x-ray transition is the $3s \rightarrow 2p$ transition. In Cu, however, the $3d$ level is populated and the principal L x ray involves the $3d \rightarrow 2p$ transition; thus as one removes $3d$ electrons from Cu both the x-ray and the Auger transition rates decrease at about the same rate and the ratio, the fluorescence yield, is relatively unchanged. This continues to be the case until a large number of $3d$ electrons has been removed. As one then continues to remove $3d$ electrons the Auger transitions involving $3p$ electrons become relatively more important and the Auger rate decreases at a smaller rate than the x-ray rate, i.e., the fluorescence yield drops. This continues until all the $3d$ electrons are removed. Once all the $3d$ electrons have been removed, we begin to strip $3p$ electrons and so we have returned to a situation similar to that of Ar and fluorescence yield increases with increasing outer-shell ionizations.

Considering possible effects of variations of fluorescence yield on published Cu cross-section data (see Sec. 3.3.2), the spectral measurements from low-energy collisions (less than 3 keV/amu) involving Cu suggest that the number of M-shell vacancies is less than six (Kavanagh *et al.* 1972). Thus effects of possible changes in the fluorescence yield are less than the quoted experimental uncertainties. In more energetic collisions (greater than 100 keV/amu), spectral shift

TABLE 3.5. Estimated changes in ω_k for various vacancy configurations of the Ar atom (from Larkins, 1971b).

Atomic configuration	ω_k	Atomic configuration	ω_k
$[1s]$	0.130	$[1s, 2p^6]$	0.134
$[1s, 2p]$	0.143	$[1s, 2p, 3p^6]$	0.147
$[1s, 2p^2]$	0.158	$[1s, 2p^2, 3p^6]$	0.162
$[1s, 2p^3]$	0.174	$[1s, 2p^3, 3p^6]$	0.177
$[1s, 2p^4]$	0.187	$[1s, 2p^4, 3p^6]$	0.184
$[1s, 2p^5]$	0.183	$[1s, 2p^5, 3p^6]$	0.157

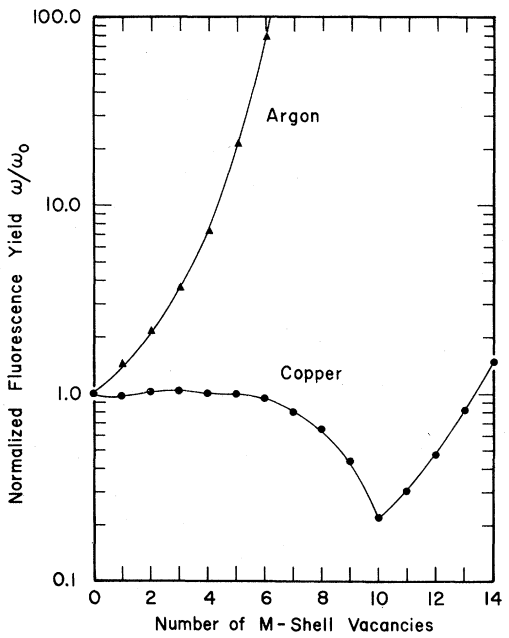

FIG. 3.36. Calculated L-shell fluorescence yields as a function of the number of M-shell vacancies for Ar (Larkins, 1971b) and Cu (Fortner *et al.*, 1972). Results are normalized to ω_0, the normal ground state value.

measurements (Burch, Richard, and Blake, 1971; Der *et al.* 1971b) indicate that the changes in the fluorescence yield could be quite large (i.e., large numbers of M-shell vacancies are produced) and thus considerable care must be taken in obtaining L-shell vacancy production cross sections from such x-ray measurements.

Thus, while in some cases inner-shell fluorescence yield values show extreme sensitivity to outer-shell defects, x-ray measurements can in many cases, at least for lower collision energies, provide a reliable source of excitation cross sections using normal atomic values of fluorescence yield. On the basis of calculations like those discussed above, some general statements can be made: The value of ω_K is insensitive to outer-shell defects except when near depletion of the $2p$ level is involved. Values of ω_L are insensitive to excitation of levels outside the M shell, and to moderate ionization of the $3d$ shell; as shown in Fig. 3.36, near depletion of the $3d$ shell and ionization of the $3p$ shell have strong effects which are in opposite directions. Fluorescence yields for the M shell will not be significantly changed from normal atomic values unless outer-shell effects nearly deplete the $4f$ level; further depletion of the $4f$ level would cause a decrease in ω_M, followed by an increase in ω_M as the $4d$ level loses electrons. Finally, the use of solid targets can in some cases diminish these effects since membership of outer-shell electrons in the valence band can produce rapid effective repair of otherwise serious outer-shell defects.

In addition to the multiple *vacancy* effects discussed above, electron promotion mechanisms in ion–atom

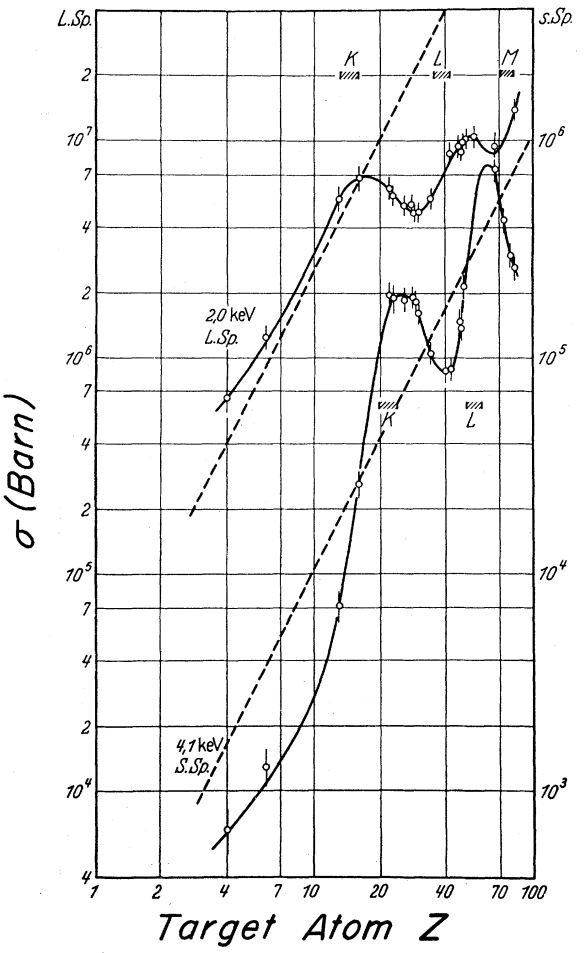

FIG. 3.37. Cross sections for ionization of the L shell of the light fission fragment (curve labeled *L. Sp*) and heavy (*S. Sp*) fission fragment for 74- and 42-MeV fragment energies, respectively, as a function of target atomic number. The dashed curves show Born approximation predictions and the shaded blocks indicate target atom Z values for which target atom K-, L- or M-shell binding energies match (within 20%) the projectile L-shell energy. [After Specht (1965).]

collisions can populate *normally empty* levels producing new configurations that can have different relative Auger and x-ray transition rates. Examples of the creation of new x-ray components by this mechanism are discussed (see Sec. 3.4.3) by Cunningham, *et al.* (1970) for Ar^+–Ar collisions (creation of $3d$ electrons) and by Fortner, Der, and Kavanagh (1971) for collisions involving Xe (creation of Xe $4f$ electrons).

3.3.6 Level Matching Effects

The observation by Specht (1965) of a cyclic Z dependence in x-ray production cross sections was one of the earliest indications of the inadequacy of direct Coulomb excitation theory for describing heavy-ion interactions. His result, showing peak cross sections for fission fragment excitation for those values of target Z for which there is an approximate matching of the binding energy of the electron being excited with some electronic binding energy in the collision partner, is shown in Fig. 3.37. Recently the Z dependence of Cu L-shell x-ray emission has been studied by Kavanagh, *et al.* (1970), and Saris (1971) has discussed a similar effect for the Ar L shell. Cairns *et al.* (1970) observed the level matching effect in their thick target x-ray yields from copper targets.

Data of Kavanagh, *et al.* for Cu are shown in Figs. 3.38 and 3.39. In Fig. 3.38 the Cu x rays originate in target atoms, while in Fig. 3.39 they originate in incident Cu ions. In both Figures the x-ray production cross sections show very pronounced peaking for Z values corresponding to a match of the Cu L-shell binding energy with some electronic binding energy in the collision partner. The data in Fig. 3.38 show decreasing peak-to-valley ratios with increasing ion velocity; such a velocity dependence was also noted by Specht (1965), and explains the weaker effect that he observed. The Cu data appear to demonstrate a lack of reciprocity in the roles of target and projectile, in that the curve for Cu projectiles appears to be shifted to higher Z by one or two units relative to the data for Cu as the target. Kavanagh *et al.* (1970) also note that while near the peaks in Figs. 3.38 and 3.39 both target and projectile x rays are produced (and may be difficult to resolve from one another), Cu L x rays over-

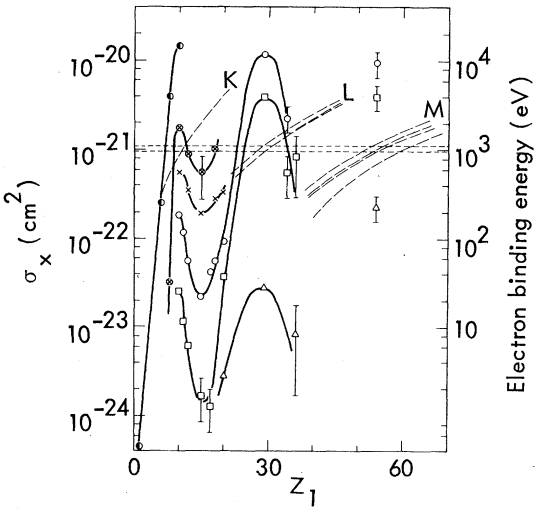

FIG. 3.38. Cross sections for Cu L x-ray production (left-hand scale) in a thick Cu target as a function of the atomic number of the incident ion, for different, fixed, ion energies per atomic mass unit (i.e., fixed ion velocities): triangles, 1.0 keV/amu; squares, 2.0 keV/amu; open circles, 3.0 keV/amu; crosses, 5.0 keV/amu; crossed circles, 10 keV/amu; and half-filled circles, 50 keV/amu. The dashed lines represent ground-state electron binding energies (right-hand scale): The horizontal dashed lines represent Cu L-shell binding energies, and the dashed curves show electron binding energies for the incident ions as a function of their atomic number. The data points for Xe ($Z_1=54$) may be too high due to the recoil effect discussed by Taulbjerg and Sigmund (1972). [After Kavanagh *et al.* (1970).]

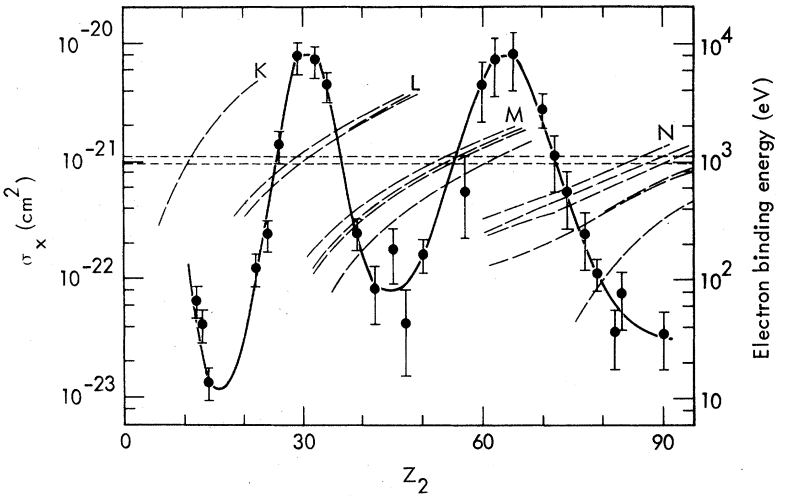

FIG. 3.39. Cross sections for Cu L x-ray production (left-hand scale) in the incident Cu ions striking solid metal targets, as a function of the atomic number of the target, for a fixed ion energy of 160 keV (2.5-keV/amu). The dashed lines represent ground state electron binding energies (right-hand scale): The horizontal dashed lines represent Cu L-shell binding energies, and the dashed curves show target atom binding energies as a function of target atomic number. [After Kavanagh *et al.* (1970).]

whelmingly dominate on the high-Z sides of the peaks, and collision-partner x rays dominate the spectra on the low-Z sides of the peaks. It should be noted that the cross sections shown in Fig. 3.38 for Xe^{+}–Cu ($Z_1 = 54$) may be too large due to the recoil effect discussed by Taulbjerg and Sigmund (1972); such effects are, of course, unimportant when the measured x rays are from the projectile, as in Fig. 3.39.

The level-matching effect for the production of Ar L x rays is shown in Fig. 3.40 from Saris (1971). Here Ar gas is the target. Peaks in the cross section occur for approximate matching of projectile K- and L-shell binding energies with the energy of the Ar L shell. As pointed out by Saris, the peaks appear to move to larger Z values with increasing bombarding energies. While no such effect is evident in the copper data of Fig. 3.38, plots as in Fig. 3.39 for incident copper ions of *different* velocities would show such a shift [Kavanagh *et al.* (1972) show that cross-section curves are steeper for target Z values on the high-Z sides of the level-matching peaks.]

In Sec. 3.1.4 we discuss MO diagrams for asymmetric collisions, and interpretation of the level-matching effect within this framework is quite straightforward. A set of these correlation diagrams, relevant to the Ar L-shell data of Saris, is shown in Fig. 3.2. (The diagrams are qualitatively identical for other collision systems. They were constructed for neutral atoms, and slightly different binding energies would be required for incident ions. Multiple interactions which lead to a distribution of states of outer-shell excitation for the projectile—as encountered when solid targets are used—would

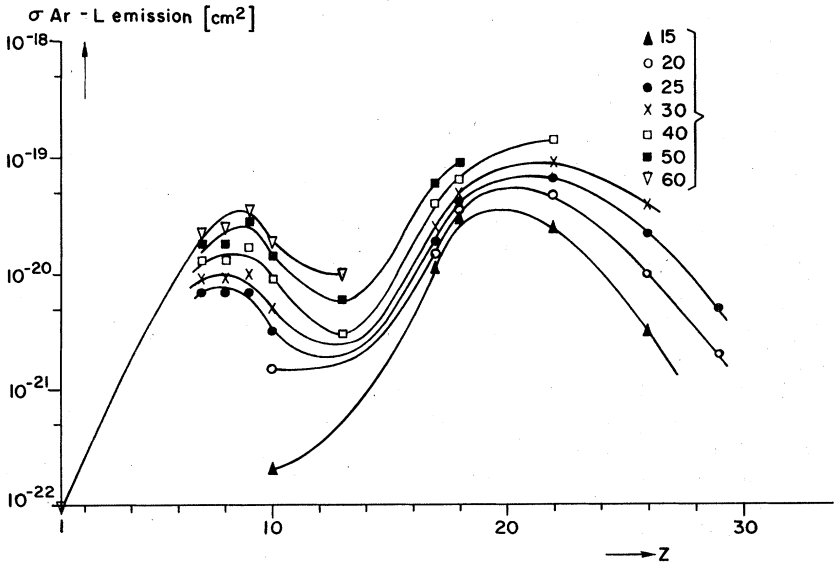

FIG. 3.40. Cross sections for Ar L x-ray production in Ar gas targets as a function of projectile Z. The different curves are for different collision energies in c.m. system [After Saris (1970).]

result in a broadening of the levels in the direction of increased binding energy.) The MO structure is seen to change abruptly with changing collision partner Z when level matching occurs. Figures 3.2(a) and 3.2(b) show cases on either side of an exact match of the Ar $2p$ energy with the collision partner $1s$ binding energy. Note that in Fig. 3.2(a) (B+Ar), the argon $2p$ electrons go smoothly into the combined atom $2p$ level as the two particles approach one another, with the only effect being an increase in the electron binding energy. In Fig. 3.2(b) (C+Ar), however, there are two $2p$ electrons of Ar in the steeply rising $3d\sigma$ MO. Transitions can occur where this MO terminates, together with empty $3d\pi$ and $3d\delta$ orbitals, at the $3d$ level of the combined atom. Also, it is probable that the steepness of the $3d\sigma$ level results, at least for higher bombarding energies, in strong coupling to the continuum through adiabatic terms (see Sec. 3.3.4) with resultant large excitation probabilities. This is consistent with the large cross section for Ar L x-ray production in C–Ar collisions. Figure 3.2(c) represents Al+Ar, for which Saris observes a cross-section minimum. The correlation diagram is qualitatively like that for C+Ar, though the $3d\sigma$ orbital would be more adiabatic, and the $3d\pi$ MO is filled. The cross-section decrease in going from the C+Ar case to Al+Ar [Fig. 3.2(b) to Fig. 3.2(c)] reflects the decreasing radius of the collision partner K shell and the increase in nuclear repulsion between the atoms. The interaction of the Ar L shell with the collision partner K shell, at a collision distance roughly equal to the sum of these shell radii, forces the promotion of Ar $2p$ electrons via the $3d\sigma$ MO. A decrease in the critical interaction radius together with increased nuclear repulsion between the atoms would result, for a given bombarding energy, in a smaller interaction probability. The nuclear repulsion effect dominates at low energy. Figure 3.1 represents the symmetric Ar+Ar collision, with perfect level matching. Argon $2p$ electrons are promoted here via the $4f\sigma$ level which rises very steeply, with many level crossings, to the $4f$ level of the combined atom; coupling to the continuum via nonadiabatic terms should be large at the higher bombarding energies (see Sec. 3.3.4). Figure 3.2(d) illustrates a case on the high-Z side of the L–L matching peak; Ar $2p$ vacancies still result from $4f\sigma$ promotion as in the Ar+Ar case, with the decreasing cross sections, again, reflecting the decreasing radius of the collision partner L shell, and the increasing Coulomb repulsion between the nuclei. Diagrams similar to those in Fig. 3.2 can, of course, be constructed for $2p$ vacancy production in Cu collisions as discussed by Kavanagh *et al.* (1970). In summary, one notes that abrupt changes in MO schemes (e.g., $2p$ promotion switching from $3d\sigma$ to $4f\sigma$ MO's) occur for relationships of Z_1 and Z_2 for which there is an energy matching of atomic levels with the same number of nodes in the radial wave function. Thus, the next abrupt rerouting of $2p$ electrons, beyond those illustrated in Fig. 3.2, occurs when the $2p$ energy matches the $3d$ level of the collision partner. This is strikingly consistent with the apparent position of the L–M matching peak in the Cu data of Fig. 3.39.

While the correlation diagrams discussed above predict the positions of cross-section maxima, a simple application of these ideas would predict *abrupt* rises in cross section at appropriate level matchings, followed by a slow decrease with increasing Z. An extreme illustration of this is offered by data on the low-Z side of the K–L matching peak in Fig. 3.38: Measured cross sections for Cu L excitation by incident O and C ions are much larger than direct scattering theory would predict, yet the correlation diagrams show no Cu $2p$ promotion at all. (The analog in Fig. 3.2 would be Ar $2p$ excitation in B–Ar collisions.) In fact, the only adiabatic effect indicated would result in increased $2p$ binding energy, with correspondingly depressed cross sections. It is suggested by Specht (1965) and Barat and Lichten (1972) that these effects, which manifest themselves in the broad, symmetric level matching peaks, can be explained in terms of the uncertainty principle: uncertainties in electron binding energies during the collision, reflecting the collision times through the uncertainty relation, will contribute to a mixing of *near-matching* levels with resultant smearing of the level-matching peaks. Crucial to this interpretation is a recognition that the interaction length is small compared to the relevant shell radii. Barat and Lichten have attempted an analytical construction of the L–L matching peak for Cu (Fig. 3.39) in which they account for orbit radius and Coulomb repulsion effects using the Kessel expression (see Sec. 3.3.4) and for which they

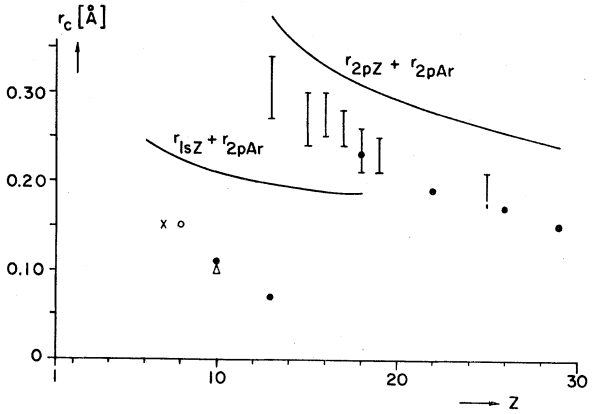

FIG. 3.41. Critical internuclear distances for collisions involving Ar and a range of collision partners, as a function of collision partner Z. The figure is taken from Saris (1971), and the solid circles show his data on critical radii for Ar L x-ray production. The other plotted points are from scattering experiments, and the data represented by bars for $13<Z<18$ represent L excitation not of Ar but of the collision partner. The solid lines represent sums of shell radii.

use a probability function given, essentially, by $p=\exp(-\Delta E\lambda/v)$ to describe mixing of near-matching levels, where ΔE is the energy separation between the atomic levels, λ is the interaction length, and v is the collision velocity. While the justification for this, in this application, is somewhat unclear, the result qualitatively reproduces the structure in the cross-section data.

As has been pointed out by Fastrup and Hermann (1969) and by Kavanagh *et al.* (1970), in collisions involving near-matching, vacancy production is overwhelmingly more probable in the more loosely bound level of the near-matching pair. These observations are in agreement with the correlation schemes in Fig. 3.2. For example, in the case of Ca+Ar [Fig. 3.2(d)], $2p$ vacancies in Ar are strongly produced via the $4f\sigma$ MO, while Ca $2p$ vacancies require the $3d\sigma$ crossing at small collision distances. On the other side of matching, e.g., Al+Ar [Fig. 3.2(c)], there is a swapping of the roles of the $4f\sigma$ and $3d\sigma$ orbitals; Al vacancies now result from crossings of the rapidly rising $4f\sigma$ level. This effect is also strikingly demonstrated in recent x-ray studies of the C–Ar system (Der *et al.*, 1971c) in which spectra were compared for collisions in gas targets and solid C targets (see Sec. 3.4.3). In gas targets, Ar $2p$ vacancies are created as suggested in Fig. 3.2(b), with no evidence of K-shell vacancy creation in C.

The analytical fit by Barat and Lichten to the Cu level matching data illustrates an important point relevant to *relative intensities* of x rays from the two collision partners. Because of the strong effect of target Z on production of target vacancies (through the Coulomb repulsion effect; see also experimental data of Specht), the *ratio* of vacancy production probabilities for the two partners will show a much stronger variation across a matching peak than that shown for projectile x rays in Fig. 3.39. On the low-Z side of a match, cross sections for the target *rise* rapidly with decreasing target Z, while cross sections for the projectile drop rapidly. Thus, to within the sensitivity of many spectral measurements, a given component may be virtually switched on or off by small changes in Z values in the vicinity of level-matching peaks.

Saris (1971) has observed that for Al+Ar collisions the critical distance of closest approach for Ar L-vacancy production, based on the apparent x-ray production threshold, is *much smaller* than the critical distance for L-vacancy production in Al, as determined in the scattering experiments of Fastrup and Hermann (1969) (see Fig. 3.41). This is consistent with the above, since Ar L-shell excitation involves an Ar $2p$–Al $1s$ interaction, whereas Al L excitation would involve an interaction of the two L shells. (Though a particular model was used by Saris, the radii derived on the basis of an apparent energy threshold are moderately model-insensitive because all potential energy curves are steeply rising functions of r for small r.)

3.4 Spectral Measurements

3.4.1. Introduction

In this section we discuss spectral measurements performed with sufficiently high resolution to provide information about the excited-state configurations produced in heavy-ion–atom collisions. In general, the spectra are quite different from those resulting from excitation by photons, electrons, protons, or alpha particles. Principal peaks are broadened and shifted in energy, satellite lines are more intense, and previously unobserved lines appear. The essential point in all the work to be discussed is that multiple excitations occur with very high probability. Interpretation of the data appears to offer two major challenges: The first is the use of calculational techniques (e.g., Hartree–Fock or Hartree–Fock–Slater) to determine the configurations that are consistent with the observed spectra. While such comparisons of calculation and experiment appear, from the literature, to be quite successful for the x-ray data, the ranges of validity of the different calculational techniques are far from clear. In cases where this does not lead to ambiguity in the determination of relevant excited-state configurations, the data can provide a basis for improving these calculational techniques. The second challenge offered by the spectral data is that of integrating the systematics of multiple excitation into the theoretical structures being used to describe the ion–atom interaction itself. Very little has been accomplished to date in this regard. While the molecular-orbital level-crossing mechanism can, in principle, provide multiple excitations in a straightforward way, care must be exercised to avoid using this concept outside the range of its validity. In most of the data to be discussed below, the creation of the primary vacancy (i.e., the one that produces the x ray or electron being examined) can perhaps be considered quasiadiabatic (i.e., $E/\lambda u \lesssim 0.1$), but such is not always the case for the outer-shell vacancies that are apparently created at the same time, and that are responsible for observed shifts in x-ray lines. For example, for 10–40 MeV O ions incident on Cu, $E/\lambda u$ is ~ 0.1 for the K shell, but for the L and M shells that are excited simultaneous with K-shell excitation, the $E/\lambda u$ values are of the order 1 and 10, respectively. Thus, calculations such as those of McGuire and Mittleman (1972) (see Sec. 2.4), which treat multiple excitations by incident point charges, are more appropriate. Possible important effects, in this context, of tightly bound electrons on the projectile (screening) have not been considered.

3.4.2. Auger-Electron Spectra

Previously, in Fig. 2.9, Ne K-shell Auger-electron spectra for excitation by photons, electrons, protons, and Ne ions were presented. In Sec. 2.4.1 we discussed the first three of these spectra in some detail. As can be

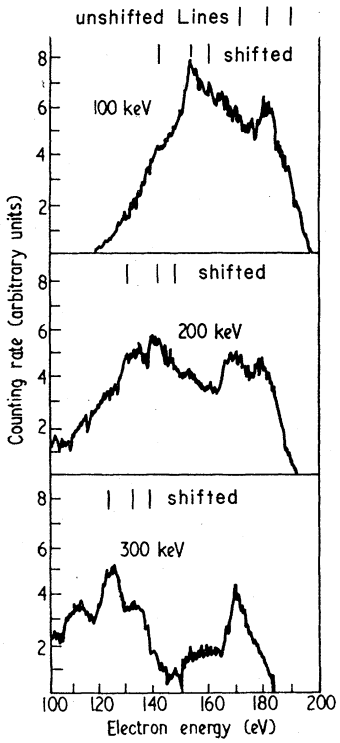

FIG. 3.42. Auger electron spectra for 100-, 200- and 300-keV Ar^+–Ar collisions, from Rudd, Jorgensen, and Volz (1966). These authors have identified three peaks and their Doppler-shifted counterparts at the positions indicated in the figure.

seen from Fig. 2.9, the fourth spectrum, for excitation by incident Ne ions, bears little resemblance to the other three. The experimental procedure used in the heavy-ion case is essentially the same as that previously discussed for light ions (Sec. 2.4.1). For a more detailed discussion of energy spectra of electrons ejected in ion-atom collisions, see Ogurtsov (1972).

An important feature of heavy-ion bombardment is that one may observe transitions from the projectile as well as from the target and, in addition, target atoms may acquire significant recoil velocities. The Doppler effect can thus have considerable influence on the resultant electron spectra. In the case of small scattering angles, the Doppler shift ΔE_D for the incident projectile ion is given by

$$\Delta E_D \simeq m v_p v_e \cos\alpha + (m v_p^2/2)\cos 2\alpha, \quad (3.23)$$

and for the target atom is

$$\Delta E_D \simeq m v_T v_e \cos\alpha, \quad (3.24)$$

where m is the electron mass, α is the observation angle, v_e is the electron emission velocity in the frame of the atom, v_p is the incident particle velocity, and v_T is the recoil velocity of the target atom. In general, these shifts can be quite large; for example, in 300-keV Ar^+–Ar collisions (Rudd, Jorgensen, and Volz, 1966) the observed ~180-eV Auger lines are shifted about 47 eV when transitions from the projectile are observed. In symmetric collisions, these Doppler-shifted lines from the projectile are often superimposed on the lines from the target, which suffer much smaller shifts. In many cases this complicates the analysis of the spectra.

In addition to Doppler shifts, variations in the azimuthal scattering angles give rise to a "Doppler broadening" whose widths are given by

$$\Delta E \simeq 2 m v_p v_e \sin\theta \sin\alpha \quad (3.25)$$

and

$$\Delta E \simeq 2 m v_T v_e \sin\phi \sin\alpha \quad (3.26)$$

for the projectile and the target, respectively, where θ is the scattering angle of the incident particle and ϕ is the recoil angle of the target atom. Since Doppler broadening is a function of the scattering angles, the kinematics associated with the specific collision have a strong effect on the final Auger-electron spectra. Gordeev and Ogurtsov (1971) have investigated the importance of these kinematic effects on the Auger-electron spectra resulting from Ar^+–Ar collisions, and this work is discussed below.

As was the case for proton bombardment, all the reported characteristic electron data involve either the Ar L shell or the Ne K shell. The symmetric Ar^+–Ar collision has been studied most extensively (Rudd, Jorgensen, and Volz, 1966; Ogurtsov *et al.*, 1968; Ogurtsov, Flaks, and Avakyan, 1970). The first reported measurements (Rudd, Jorgensen, and Volz, 1966) were for 100, 200, and 300 keV incident ions, and the results of those measurements are presented in Fig. 3.42. In general, three peaks and their Doppler-shifted counterparts are observed; these are indicated in the Figure. The most intense Auger lines for proton bombardment (see Fig. 2.10) appear above 200 eV; however, in the case of heavy-ion bombardment no Auger lines are seen at these energies. Correlation of these Auger peaks with specific atomic configurations is difficult but some general statements can be made: On the basis of the scattering experiments (Sec. 3.2) one expects considerable M-shell excitation in collisions which produce an L-shell vacancy. Such M-shell excita-

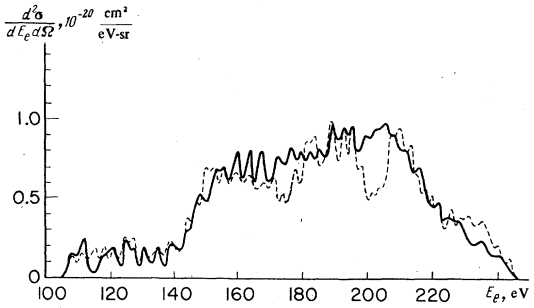

FIG. 3.43. The Auger-electron spectrum between 100 and 240 eV corresponding to the filling of Ar $L_{2,3}$ vacancies. The spectrum was produced in 15-keV Ar^+–Ar collisions. The continuous curve is the data of Ogurtsov, Flaks, and Avakyan (1971) and the dashed curve represents the calculations of Gordeev and Ogurtsov (1971). [After Gordeev and Ogurtsov (1971).]

tion in general would shift L Auger transition energies to lower values, which is consistent with the spectral data. At these collision energies the scattering experiments also indicate that some collisions will give rise to the production of multiple L-shell vacancies; these multiple L-shell vacancies tend to shift Auger transitions to higher energies. For a general discussion of Auger transition energies, see Larkins (1971a, b). Related x-ray spectra from Ar^+–Ar collisions (Cunningham, *et al.*, 1970) will be discussed later in this section.

Ogurtsov, Flaks, and Avakyan (1969a, 1970) have reported Auger electron spectra from Ar–Ar collisions at considerably lower bombarding energies (15 keV); the results of those measurements are summarized in Figs. 3.43, 3.44, and 3.45. In Fig. 3.43 the continuous curve is the measured electron energy spectrum in the energy range 100–240 eV for 15-keV Ar^+–Ar collisions. Auger transitions in this energy range correspond to the filling of one $L_{2,3}$ vacancy. The dashed curve in the Figure is the result of calculations reported by Gordeev and Ogurtsov (1971). These calculations correct *proton-produced* Auger spectra for effects of the kinematics of the atomic collisions by considering the Doppler shift (Eqs. 3.23 and 3.24) and broadening (Eqs. 3.25 and 3.26) of the spectral lines. The calculations used the $L_{2,3}$–Auger electron spectra from H^+–Ar collisions (Ogurtsov, Flaks, and Avakyan, 1969b) and the energy and scattering angle distribution measured by Afrosimov *et al.* (1964). In general, the agreement is quite good, indicating that kinematic effects have a dominant effect on spectral shape.

In Fig. 3.44, the electron energy spectrum in the energy range 400–550 eV for 15-keV Ar^+–Ar collisions is presented. These transitions result from the simultaneous filling of two L-shell holes. [*Note added in proof:* In recent careful investigations M. E. Rudd and coworkers (private communication) find no evidence for these transitions.] These lines, surprisingly, have a total intensity of about one-half that of the single $L_{2,3}$–Auger transitions represented in Fig. 3.43.

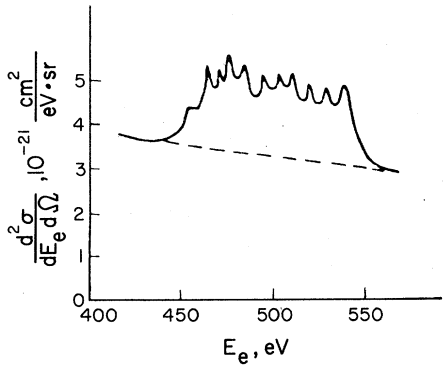

FIG. 3.44. The Auger-electron spectrum between 400 and 550 eV corresponding to the simultaneous filling of two Ar L-shell vacancies. The spectrum was produced in 15-keV Ar^+–Ar collisions. [After Ogurtsov, Flaks, and Avakyan (1971.)]

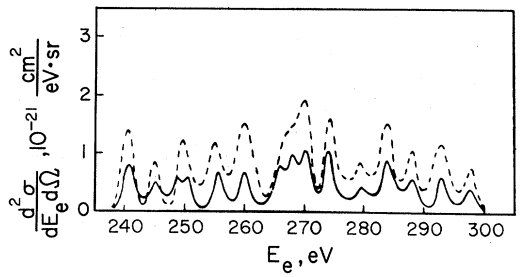

FIG. 3.45. Auger-electron spectra between 240 and 300 eV corresponding to the filling of Ar L_1 vacancies. The spectra were produced in Ar^+–Ar (solid curve) and Ar^{2+}–Ar (dashed curve) collisions with incident ion energies of 15 keV. [After Ogurtsov, Flaks, and Avakyan (1969a).]

In Fig. 3.45 the electron energy spectrum in the energy range 240–300 eV is presented for 15-keV Ar^{2+}–Ar and Ar^+–Ar collisions. Auger transitions in this energy range correspond to the filling of one L_1 vacancy. The comparison of the Ar^{2+}–Ar and Ar^+–Ar data shows a dependence of the cross section on the number of initial $3p$ vacancies. This represents an analog to the similar initial charge state dependence observed in Ne–Ne collisions which was discussed in Sec. 3.2.3, and is consistent with the molecular-orbital picture, where the vacancies are produced by the $3p\sigma$–$3p\pi$ level crossing (see Fig. 3.1).

The Ne K-shell Auger electron spectrum for 200-keV Ne^+–Ne collisions has been presented in Fig. 2.9(d) (Edwards, 1967). Although no detailed interpretation of the spectrum is available, the general absence of intense components between 790–810 eV suggests considerable L-shell excitation associated with the production of the K-shell vacancy. Another important result for 400-keV Ne–Ne collisions has been obtained by Kessel, McCaughey, and Everhart (1966). Due to the Doppler shift, Kessel *et al.* were able to resolve the K-shell Auger electrons from the projectile and target and deduce that the inner-shell vacancy was produced in the target or the projectile with equal probability.

3.4.3 X-Ray Spectra

We attempt here to characterize the available experimental data on x-ray spectra. The picture that emerges is far from cohesive at this time, because of lack of a general theoretical framework for discussing multiple excitation effects; it is hoped, however, that this data review will stimulate further relevant work. While much of the experimental data already available is of high quality, some guidance for future work appears to be appropriate: It is important, in order to test theoretical models, that experiments provide *cross sections* for the production of observed spectral components, as a function of collision energy. This requires the use of thin (or gaseous) targets, or, in cases where thick targets must be used, careful differention of curves of yield versus bombardment energy. (See

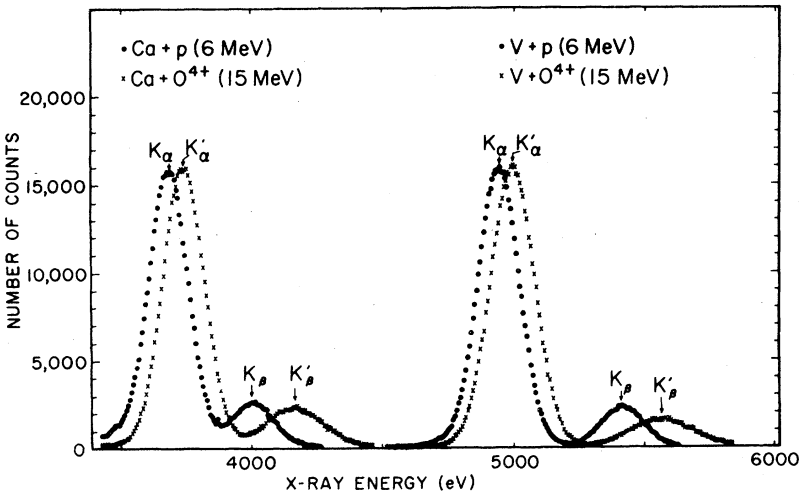

FIG. 3.46. X-ray spectra for Ca and V produced in proton and O ion bombardments. [After Burch and Richard 1970).]

Sec. 2.3.1). Instrumental effects such as variation, with photon energy, or Bragg crystal reflectivity, detector efficiency, window and target absorption (particularly in the region of absorption edges) must be examined with care. Finally, evidence is presented below showing that x-ray spectra can be severely influenced, in solid targets, by multiple collision and recombination effects; these must be separated, in any theoretical analysis, from multiple-excitation phenomena in single collisions.

3.4.3(a) Solid-State Detector Measurements

Early use of lithium-drifted silicon [Si(Li)] detectors in studies of shifted x rays from ion–atom collisions was made by Richard and co-workers. Data from one of their papers (Burch and Richard, 1970) are shown in Fig. 3.46. Spectra of K x rays of Ca and V are compared for 15-MeV O^{4+}-ion bombardment and for 6-MeV protons. Upward shifts in both the K_α and K_β energies, and a broadening of the K_β line are clearly shown for the O-ion bombardments as compared to the proton case. Hartree–Fock–Slater (HFS) calculations were performed by Burch and Richard to estimate the expected shifts of the K_α ($2p\rightarrow 1s$) and K_β ($3p\rightarrow 1s$) lines for multiple ionized atoms. Their results for Ca and V are shown in Fig. 3.47. The requirement of simultaneous agreement for K_α and K_β shifts provides a stringent test of the possible configurations, and it appears that creation of two or three L-shell vacancies, simultaneous with K-vacancy production, is involved. The calculations also indicate that the observed line broadening is consistent with a distribution of ionic configurations.

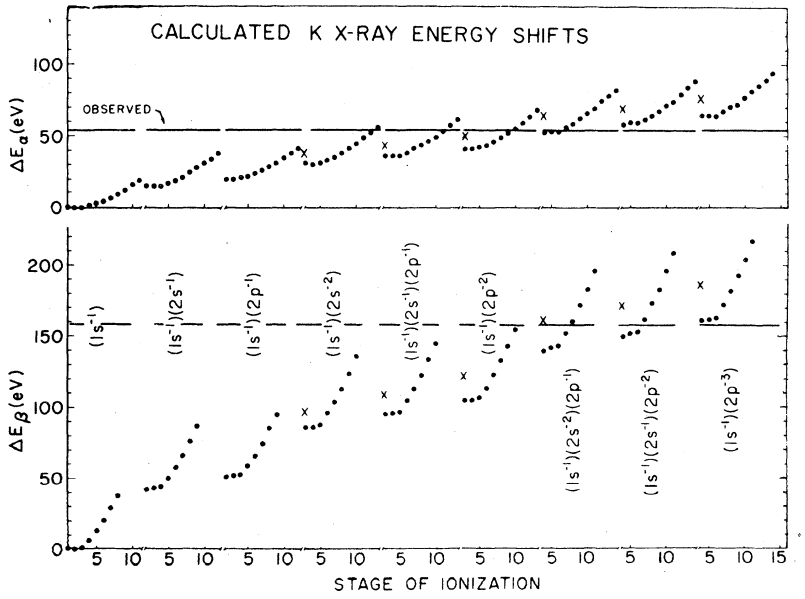

FIG. 3.47. Hartree–Fock–Slater calculations for the K x-ray energy shifts of various ion configurations. $\Delta E = E_K$ (multiply ionized) $- E_K$ (singly ionized) for both the K_α and K_β energies. The levels $(1s)^{-1}(2p)^{-1}$, etc. refer to the core electrons removed from the neutral atom. The K x-ray energy for the decay of this ion is the first point of each series and is followed by points corresponding to the successive removal of the outermost available electron. The closed circles are the calculations for Ca, the ×'s are the calculations for the corresponding core excitations in V, and the solid horizontal lines are the experimentally observed shifts. [After Burch and Richard (1970).]

Figures 3.48 and 3.49 (Burch and Richard, 1971) show the bombarding-energy dependence of K_α and K_β x-ray energy shifts for O-ion bombardment of Cu, Ca and Al, and the variations in the K_α/K_β intensity ratios for Cu and Ca targets. The energy shifts for Cu show a monotonic increase with ion energy, those for Ca show a peaking, and those for Al decrease with increasing bombarding energy. This reflects the general expectations regarding variations of cross sections for the *L- and M-shell vacancies* that determine the shifts—i.e., an increase with increasing ion energy for $E/\lambda u \equiv (v_0/v)^2 \lesssim 1$, and a decrease for $E/\lambda u > 1$ (note that for the K shell, $E/\lambda u < 1$ for the whole range of data).

Measurements by Watson and Li (1971) involved a study of K_α and K_β x rays of Ni produced by ^{252}Cf fission fragments (mass ~107; energy ~60 MeV).

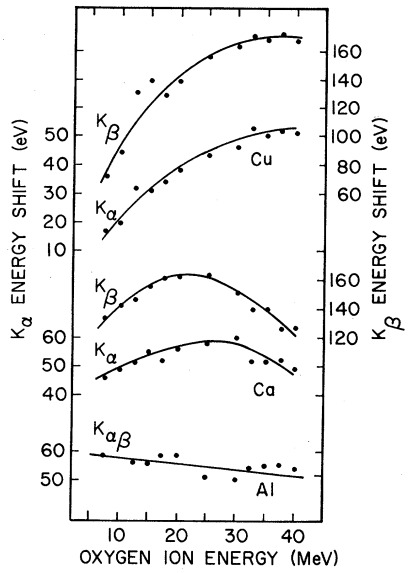

FIG. 3.48. Energy shifts of K_α and K_β x-ray lines of Cu, Ca, and Al as a function of O ion-bombarding energy. [After Burch and Richard (1971).]

These measurements constituted a high-resolution examination of a projectile/target system like the ones discussed by Specht. The K_α and K_β components were shifted up in energy by 69±11 and 210±16 eV, respectively, relative to x rays produced by alpha particles and by photons; the K_β line is also much broader for fission fragments, and a slight broadening of the K_α line is observed. These effects are similar in character to those observed in the O-ion bombardments discussed above, but require extremely high ionic charge states to be explicable in terms of multiple inner-shell plus outer-shell ionization.

Watson and Li performed HFS calculations to find configurations consistent with their data. Various configurations involving multiple inner-shell plus outer-shell ionization could explain the K_α and K_β shifts, and

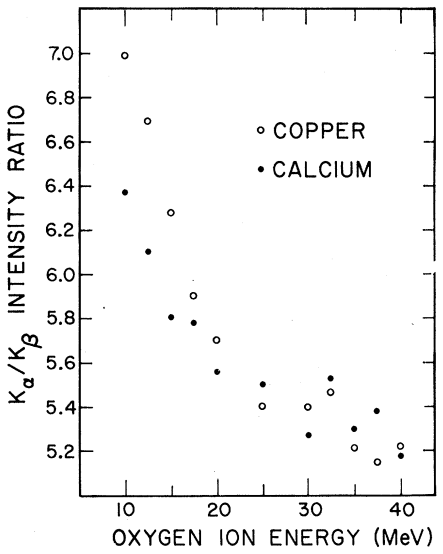

FIG. 3.49. The K_α/K_β intensity ratios for Cu and Ca targets as a function of O ion-bombarding energy. [After Burch and Richard (1971).]

results for the configuration $(1s^{-1})(2s^{-1})(2p^{-1})(3p^{-2})$ plus outer-shell ionizations are reproduced in Fig. 3.50. The K_β shift is a strong function of the degree of outer-shell ionization, consistent with the observed broadening of the K_β line if a range of ionic charge states are pro-

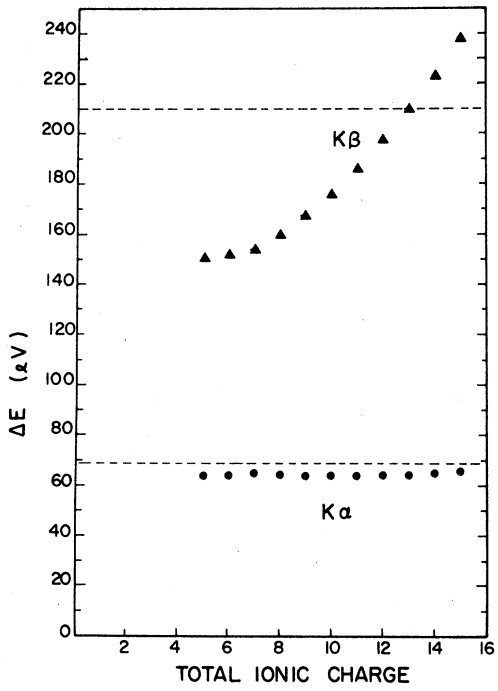

FIG. 3.50. Calculated K_α and K_β x-ray energy shifts for the ion configuration $(1s^{-1})$ $(2s^{-1})$ $(2p^{-1})$ $(3p^{-2})$ of Ni as a function of total ionic charge. The dashed lines indicate the experimentally observed x-ray energy shifts. [After Watson and Li (1971).]

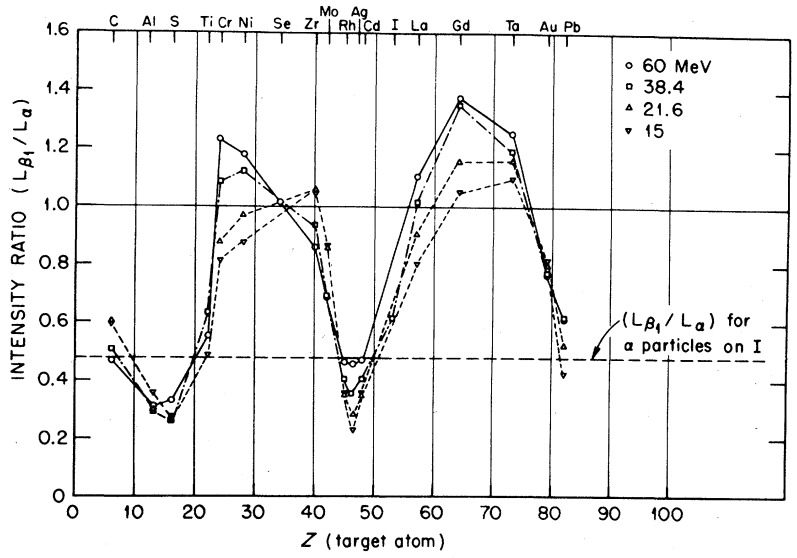

FIG. 3.51. Ratio of I $L_{\beta 1}/L_{\alpha 1,2}$ x-ray intensities produced by I ions incident on targets ranging from C to Pb, for four different ion energies. [After Datz *et al.* (1971).]

duced. The calculations indicate that high ionic charge states are required; on the average a total ionicity of +12 or +13 is needed to give the correct K_β shift. Apparently configurations which involve missing $3p$ electrons could account for an observed reduction in K_β/K_α intensity ratio, compared to that for incident alpha particles.

Mokler (1971) has studied L- and M-shell x rays from the bombardment of thin targets of Mo, Yb, and Au by 15–60 MeV I ions. X rays from both target atoms and projectile ions were recorded, in the photon energy range ~1 to 15 keV. The experimental data show that L-radiation components of both colliding particles are shifted to higher energies compared to photon-induced x rays; some L-x ray components have energies considerably beyond the corresponding L_1 absorption edge. The energy shifts were seen to depend on the nuclear charge of the emitting atom and on the bombarding energy. Mokler points out that energy structure of the M radiations of Yb and Au and the L radiation of Mo may be influenced by self-absorption in the target material in the region of absorption edges. Lines corresponding to the creation of double L-shell vacancies are observed.

Datz *et al.* (1971), studied collisions of 15–60-MeV I ions with target atoms ranging from C to Pb (using thick targets); L x-ray spectra of I were compared with those obtained by bombardment of NaI by 5-MeV alpha particles. All the lines were shifted to higher energies than in the alpha-induced spectrum, and the relative spectral intensities were drastically different. The principal differences in relative line intensities result from differences in relative probabilities of forming $2p_{3/2}$ and $2p_{1/2}$ (or $2s_{1/2}$) vacancies; these conclusions are based on relative intensities of L_α and L_{β_1} lines; the L_{β_1}/L_α intensity ratios are summarized in Fig. 3.51. The ratio varies from 1.4 to 0.2 depending on the target and displays two maxima and two minima. As pointed out by Datz *et al.*, the fluctuations cannot be understood in terms of the level-matching effect observed in gross cross section data (see Sec. 3.3.6), since the minima occur for target Z values *lower* than those corresponding to energy level matching between target and projectile. [Barat and Lichten (1972) show correlation diagrams that include spin–orbit coupling; while the correlations for $p_{3/2}$ and $p_{1/2}$ levels are quite different, there is at present no explanation of Fig. 3.51 in terms of the promotion model.] Datz *et al.* discuss the energy shifts—comparable to those reported by Mokler—and conclude on the basis of Hartree-Fock (HF) and HFS calculations that a collision that causes an L-shell vacancy also causes two to four M-shell vacancies at 15 MeV, and five to seven M-shell vacancies at 60 MeV. A double vacancy in the L-shell would cause shifts larger than those experimentally observed.

3.4.3(b) *Bragg Spectrometer Measurements*

Measurements using Bragg diffraction techniques achieve resolution superior to the Si(Li) measurements described above, and provide data at lower photon energies. Early measurements of this kind were those of Cunningham *et al.* (1970). Figure 3.52 shows their data for Ar^+–Ar collisions for several bombarding energies. For 50-keV energy, lines were detected at 224 and 264 eV. At a bombarding energy of 100 keV, an additional line is shown at about 240 eV. Further increase in bombarding energy causes an increase in the relative intensity of the 240-eV line, and a new line appears at about 250 eV; this is shown in the Figure for 130-keV bombarding energy. An increase in energy to the maximum available (330 keV) causes further

changes in the relative heights of the peaks, but no new lines appeared. An additional effect, not mentioned by Cunningham *et al.* but evident from the Figure, is an upward shift in energy of the high-energy component (i.e., the one at 264 eV for 50-keV bombardment) as the collision energy is increased.

The line observed by Cunningham *et al.* at 224 eV is the normal Ar L x ray (a mixture of L_l and L_η components, i.e., $3s \rightarrow 2p$ transitions). On the basis of HFS calculations, the higher energy lines were interpreted as follows: The highest energy component is the $L_{\alpha,\beta}$ line (the $3d \rightarrow 2p$ transition) usually not produced in Ar because the $3d$ level is normally vacant. This implies a high probability of promotion of an electron into the $3d$ level at the same time that an L-shell vacancy is produced; such a multiple excitation is easily understood within the molecular-orbital framework. The increase in energy of this line with increasing bombarding energy is probably due to increasing degrees of additional outer-shell excitation. The lines at 240 and 250 eV are apparently $3s \rightarrow 2p$ transitions in configurations with multiple M-shell and double L-shell vacancies. Cunningham *et al.* cite their 264-eV line (the $3d \rightarrow 2p$ transition), whose energy exceeds the ground-state binding energy of a $2p$ electron, as an explanation of the energy losses

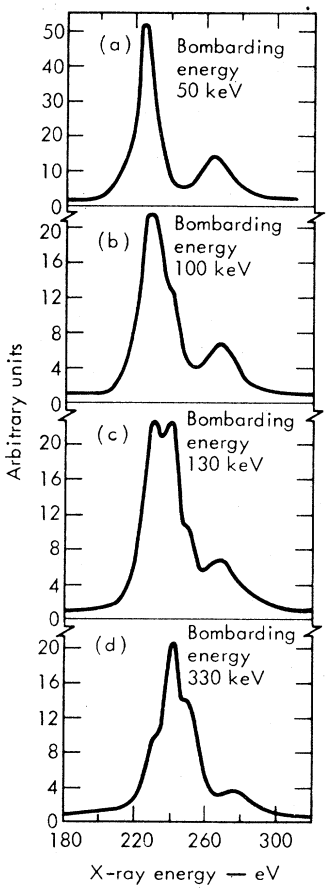

FIG. 3.52. L x-ray spectra from Ar^+–Ar collisions, for several bombarding energies, from Cunningham *et al.* (1970). Energy resolution was ~14-eV FWHM.

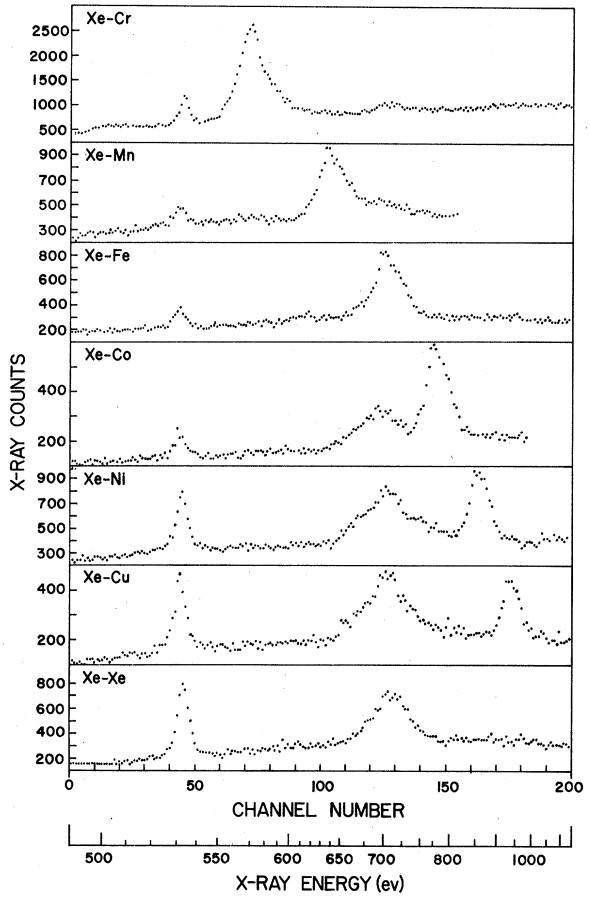

FIG. 3.53. X-ray spectra from collisions of 180-keV Xe^{2+} ions with various targets, from Fortner, Der, and Kavanagh (1971). The figure shows M lines of Xe as well as target L x rays.

observed in Ar–Ar scattering experiments, attributed to L-shell excitation (see Table 3.1).

Results analogous to those just described for the Ar–Ar system have recently been reported by Fortner, Der, and Kavanagh (1971) for excitation of the Xe M shell. Targets of Xe, Cu, Ni, Co, Fe, Mn, and Cr were bombarded by 180-keV Xe^{2+} ions and x rays in the photon energy range 500 to 1000 eV were examined; results are shown in Fig. 3.53. The spectra all show the normal $4p \rightarrow 3d$ transition in Xe at ~532 eV (the M_ζ line), and an anomalous line at ~705 eV attributed, using HFS calculations, to a $4f \rightarrow 3d$ transition (the $M_{\alpha,\beta}$ x rays); the 705-eV line implies promotion of electrons into the normally empty $4f$ level simultaneous with $3d$ vacancy creation. A further striking feature is the virtual disappearance of the 705-eV line for the metal targets as the target atom Z changes from 27 to 25. The spectra for the metal targets all show the characteristic $L_{\alpha,\beta}$ line for the metal. The disappearance of the 705-eV Xe line with decreasing target Z, occurring as the target L line sweeps across it, is not understood.

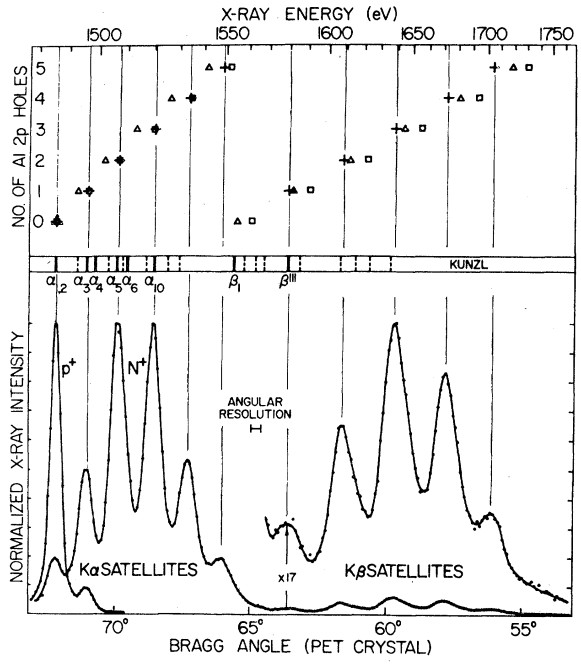

FIG. 3.54. Al K_α x-ray spectra excited by impact of 5-MeV protons and N ions on Al metal. At the top, the measured peak energies (crosses) are compared with x-ray energies obtained from the Herman-Skillman program (squares) and the screening-constant program (triangles) of Veigele, Stevenson, and Henry (1969), assuming $2p$ vacancies as well as the initial $1s$ vacancy. Energies of the $K_{\alpha 1,2}$, $K_{\beta 1}$ and satellite lines measured, for electron excitation, by Kunzl (1936) are indicated with the stronger lines labeled and the weaker satellites shown by dashed lines. [After Knudsen *et al.* (1971).]

In elegant studies of the K x rays of Al produced by 5-MeV N^+ ions, Knudsen *et al.* (1971) used a spectrometer with a resolution of about 3 eV, and clearly resolved the K_α and K_β lines into five components each. Their data are shown in Fig. 3.54, with a spectrum for incident 5-MeV protons also shown. Some of the individual components seen in the N data had previously been identified as K x ray satellites, but others are observed for the first time; relative intensities of the various components are strikingly different for incident N ions than for other means of excitation. The observed K_α and K_β satellites are interpreted to be from atoms with one through five vacancies in the L shell. This is in agreement with earlier interpretations of satellites produced by electron bombardment (Kunzl, 1936) that coincide with the three lowest energy K_α satellites.

Experimental data on x rays from 30-MeV O^{5+} bombardment of Fe, from Burch, Richard, and Blake (1971) are shown in Fig. 3.55, with a spectrum for 5-MeV incident protons for comparison. The O^{5+} data consist of a broad, shifted, K_α peak resolved into two major components, with some indication of other structure. The two major peaks are identified as K_α components from configurations with respectively, one and two holes in the $2p$ shell. Calculations indicate, in addition, that two or three $3p$ electrons are also missing at the time of K_α emission; this conclusion is independent of the occupation of the $3d$ shell. Measurement of the K_β/K_α ratio using a Si(Li) detector yielded a value consistent with HFS predictions for one or two, and two or three $3p$ vacancies for the $(2p)^{-1}$ and $(2p)^{-2}$ configurations, respectively. A third independent indication of M-shell vacancies coincident with K- and L-shell vacancies comes from a consideration of transition rates. Since the $L_{2,3}$–MM Auger process transfers $2p$ vacancies to the M shell, preservation of $2p$ vacancies until after K_α emission requires two or three $3p$ vacancies (i.e., in order to sufficiently reduce the $L_{2,3}$–MM Auger rate). This conclusion is, again, fairly insensitive to assumptions regarding $3d$ occupation; if, however, progressive removal of electrons from the outside is involved, two or three $3p$ vacancies implies a total of eight or nine M-shell holes.

Studies by Der *et al.* (1971b) of L x rays from collisions like those discussed by Burch, Richard, and co-workers provide further evidence of multiple L- and M-shell excitations. While the K x-ray data imply that K vacancies are *always* accompanied by these L- and M-shell defects, because of cross section differences the L x-ray data, to first order, do not involve defects in the K shell. Thus, the L x-ray work relates to the K x-ray data only in the general sense of demonstrating the extreme complexity of the interaction effects. Der *et al.* were able, however, to estimate the *total number* of M- and N-shell vacancies accompanying L-shell excitation, whereas the K x-ray data were sensitive essentially to only the number of $3p$ holes. Data are

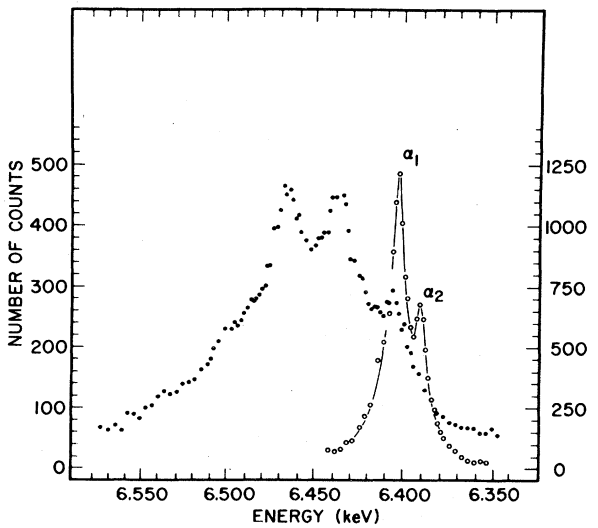

FIG. 3.55. Spectra of Fe K_α x rays produced by 30-MeV O ions (solid circles) and 5-MeV protons (open circles). [After Burch, Richard, and Blake (1971).] Width of the $K_{\alpha 1}$ peak for incident protons is about 6 eV FWHM.

shown in Fig. 3.56. All spectra show discontinuities due to target self absorption at the target L_2- and L_3-absorption edges. HFS calculations yielded the following interpretation: The principal component in each spectrum is the $L_{\alpha,\beta}$ line from an atom having a single $2p$ vacancy and an average of $7M$- and N-shell vacancies. The low energy component is a shifted $L_{l,\eta}$ line involving a similar defect configuration, and the high energy line is the result of an x-ray transition from an atom having two $2p$ vacancies and an average of $12M$- and N-shell vacancies. The high energy tails may represent contributions from configurations with three or more L-shell vacancies. These interpretations are essentially independent of *which* M- or N-shell electrons are removed.

3.4.3(c) Solid-State Effects

Recent experiments using spectroscopic techniques already described above have shown marked differences

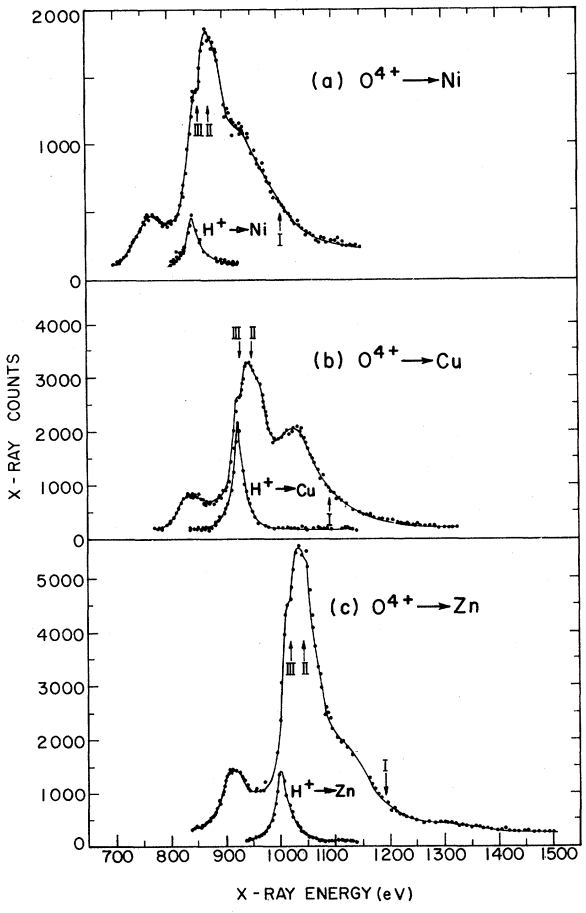

FIG. 3.56. X rays produced by 15-MeV O ions incident on Ni, Cu, and Zn. For each case the L-x rays produced by 1.6 MeV protons are also shown. The absorption edges of the target materials are shown by arrows labeled I, II, and III, corresponding to the L_1, L_2, and L_3 edges, respectively. [After Der *et al.* (1971b).]

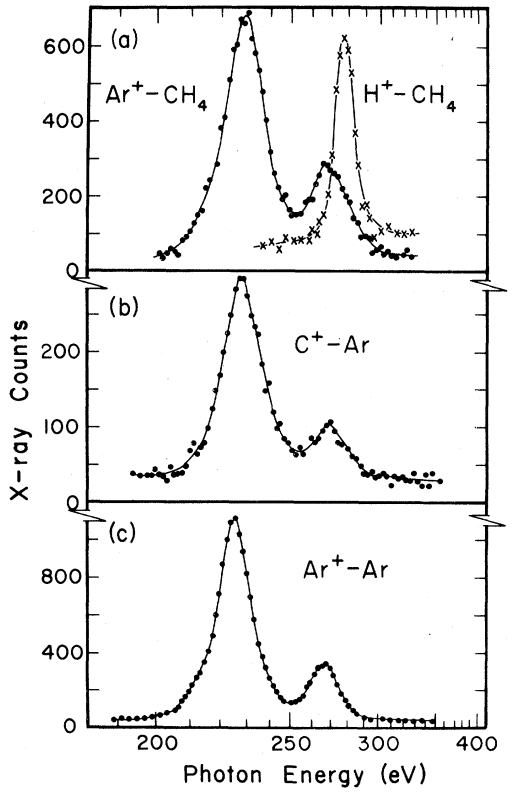

FIG. 3.57. X rays from Ar–C collisions in gas targets: (a) 90-keV Ar^+ and protons incident on CH_4; (b) 80-keV C^+ on Ar; (c) 80-keV Ar^+ on Ar. [After Der *et al.* (1971c).]

in characteristic x-ray spectra for a given projectile-target system depending on whether the target is in solid or gaseous form. The data are interpreted in terms of molecular orbitals. In addition to providing insights into the details of excitation mechanisms in such collisions, the experiments suggest the possibility of using such spectroscopic techniques as a tool for measuring charge states of ions moving *within* a solid.

Der *et al.* used a Bragg spectrometer to observe x rays from low-energy Ar^+–C collisions in solid and gaseous C (graphite and CH_4). Data for the gas target are shown in Fig. 3.57 where spectra for C^+–Ar and Ar^+–Ar are also shown to support the argument that the observed x rays in the Ar^+–C (gas) interaction result from the creation of L vacancies in Ar. A spectrum of C K x rays from proton bombardment of CH_4 is also shown for comparison and any contribution to the Ar^+–C data from C K vacancies is clearly *very* small. Figure 3.58 shows data for graphite targets, for a range of bombarding energies; there is clear evidence of C K-vacancy production in this case, with the relative intensity of the C K x ray increasing with increasing bombarding energy. Der *et al.* interpret these data in terms of a MO diagram like the one in Fig. 3.2(b) suggesting that stripping of the Ar ion in the solid

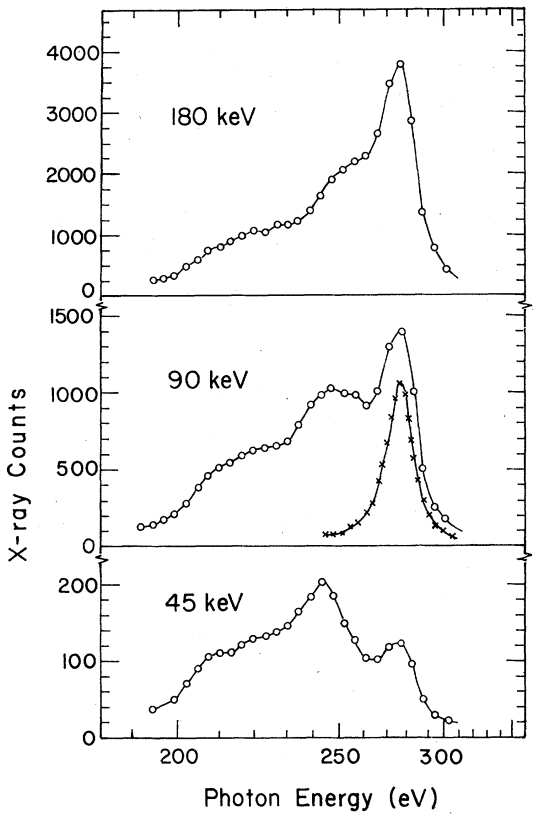

FIG. 3.58. X-ray spectra for Ar–C collisions obtained as in Fig. 3.57 but using solid C (graphite) as the target. Different bombarding energies as indicated were used to show the energy dependence of the solid state effect. The crosses represent a spectrum for 90-keV protons incident on graphite, and indicate the position of the C K x ray.

target can cause an increase in the argon $2p$ binding energy sufficient to reverse the order of the Ar $2p$ level with the C $1s$ level. (The stripping of three or more M-shell electrons, or one L-shell electron, is sufficient.) Thus, while in a gas target Ar $2p$ electrons are promoted along the $3d\sigma$ MO as in the diagram, in the solid it is the C $1s$ electrons that correlate to the united atom levels via the $3d\sigma$ MO. The broad, lower energy structure in the solid-target spectra is attributed to Ar radiations shifted by outer-shell defects. The increasing C x-ray intensity with increasing bombarding energy probably reflects increasing probability of projectile stripping.

An alternative interpretation of these data has been offered by Barat and Lichten (1972). They suggest that in the solid target multiple collisions can result in Ar–C interactions in which there is a prior vacancy in the Ar $2p$ level; vacancies in the C $1s$ level could then result from charge exchange between the $2p\sigma$ and $2p\pi$ MO's. Relaxation of the level structure to a prior $2p$ vacancy would, however, also result in a switching of roles of the Ar $2p$ and C $1s$ levels (see Cunningham *et al.*, 1970) as discussed, for the case of prior M-shell vacancies, by Der *et al.* The possibility of C K x rays being produced in the graphite target by recoil effects has been considered by Taulbjerg and Sigmund (1972) and shown to be too small an effect.

An effect, analogous to that discussed for Ar–C collisions, can be seen in data on ~900 eV x rays from Ne^+–Cu collisions in solid Cu (Der *et al.*, 1970). Copper L x rays are more intense than Ne K x rays, whereas the correlation diagrams would predict promotion of Ne K electrons *only*, via the $3d\sigma$ MO [see Fig. 3.2(a)]. Stripping of three $2p$ electrons from the Ne ion (i.e., a total charge state of four) would, however, cause the necessary binding energy reversal for the creation of $2p$ vacancies in Cu. It is important to note that the mechanism suggested by Barat and Lichten as an alternative interpretation of the Ar–C data (see preceding paragraph) has no analog for this collision system. While outer-shell stripping profoundly affects Ne $1s$ binding energies, HFS calculations predict that the K x-ray energy is essentially unchanged; this is consistent with the experimental data.

A different gas–solid effect has been observed by Lutz *et al.* (1972). Figure 3.59 shows their x-ray spectra for 48-MeV I ions incident on solid Se and gaseous Kr and Br; the most striking result is the drastic increase of I L-radiation yield in the solid as compared to gas targets. Lutz, *et al.* interpret this result in terms of creation in the solid of multiple M-shell vacancies, which render possible an I L-electron promotion, e.g., via a $3d\sigma$ MO, to an unoccupied bound state in the I M shell. These M levels are normally filled, and in a gas target the moving ion has time to de-excite M-shell excitations between collisions. [The relevant MO's are illustrated in Fig. 3.2(c) for Ar–Al where the analogous promotion would involve Ar $2p$ electrons; in the I–Se case, however, *all* the MO's in the diagram would normally by occupied.]

3.4.3(d) Molecular-Orbital X Rays

In a recent publication, Saris *et al.* (1972) discuss observations in collisions of Ar ions with C, Al, Si, and Fe targets of x rays that cannot be identified as characteristic x rays of either the target atoms or of the projectiles. They observe a broad line, or band, with centroid energy of about 1.0 keV which they attribute to radiative filling of a vacancy in the $2p\pi$ orbital of the Ar–Ar quasimolecular system *during a collision*. Such an observation would provide fundamental information about the details of the collision complex itself; all the other observations discussed in this review have involved studies of the properties of the collision partners in some state of relaxation *after* separation from one another.

Saris *et al.* used 70–600 keV Ar ions, incident on thick, high-purity targets; x rays were registered and energy analyzed with a Si(Li) x-ray detector. The x-ray band was observed for all targets. Saris *et al.* interpret

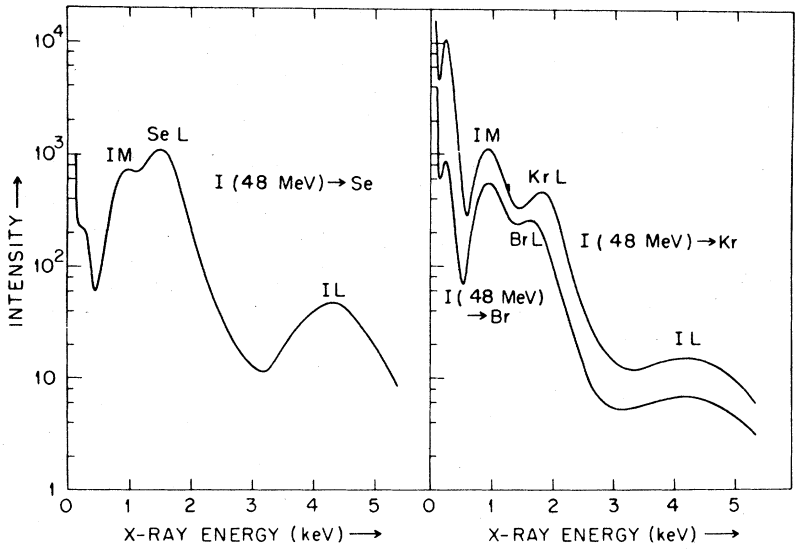

FIG. 3.59. X-ray spectra excited by impact of 48-MeV I ions on solid Se and gaseous Br and Kr targets. [After Lutz *et al.* (1972).]

this to mean that it is due to Ar–Ar collisions involving Ar atoms implanted in the target. The intensity of the ~1-keV x rays was dependent on the total dose of Ar ions, consistent with this conclusion. The characteristics of the observed x rays are consistent with the radiative filling of a previously formed (in a prior collision in the solid) $2p$ vacancy carried into the $2p\pi$ MO during an Ar–Ar encounter. (See Fig. 3.1.) For the filling of the vacancy to occur *during* the collision, the lifetime of the vacancy must be of the same order as the collision time, i.e., $\sim 10^{-16}$ sec. Saris, *et al.* point out that the lifetime of a $2p$ vacancy in the combined atom, Kr, is $\sim 4 \times 10^{-16}$ seconds. The MO x ray is also enhanced by the fact that the L-shell fluorescence yield of Kr is ~100 times larger than that for Ar. Since two collisions are required, one to form the $2p$ vacancy in the Ar ion, and the second to produce the molecular complex, the probability of MO x-ray production must depend on the atomic density of the target, i.e., the initial $2p$ vacancy must live until the second collision. Consistent with this, Saris *et al.* failed to observe the phenomenon in a dilute gas target. The cross section for the production of MO x rays was determined to be $\sim 10^{-22}$ cm^2 for 250-keV Ar ions incident on Ar saturated Si targets.

Macdonald and Brown (1972) have repeated measurements like those of Saris, *et al.*; they bombarded targets of C, Al, and Si with 25–200 keV Ar ions and, in addition, made similar measurements using a *solid Ar* target. They observed the ~1-keV x-ray band discussed by Saris *et al.* in their bombardments of C, Al, and Si; a dose dependence was observed only for the C target. For the solid Ar target Macdonald and Brown observe a much broader x-ray band, centered at higher energy; they report a broad asymmetric peak at ~1160 eV with a FWHM of ~700 eV. These differences in energy spectra raise questions regarding the earlier claim that the ~1 keV x-ray band is from Ar–Ar collisions involving previously implanted Ar ions. Macdonald and Brown conclude that the x-ray band originates from ion–target atom interactions, though it

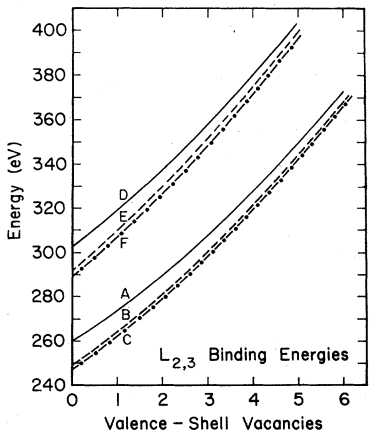

FIG. 3.60. $L_{2,3}$-orbital energies in Ar as functions of ion state. Curves labeled A are Hartree–Fock "sudden" values, those labeled B are HF "adiabatic," and those labeled C are Hartree–Fock–Slater "sudden" values. The curves D, E, and F are corresponding values for an Ar atom with a total of two $2p$ vacancies.

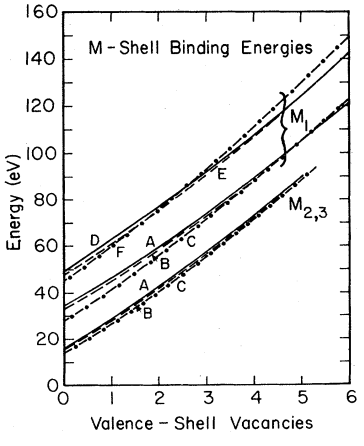

FIG. 3.61 M-shell orbital energies in Ar. Designations of the different curves are as described for Fig. 3.60.

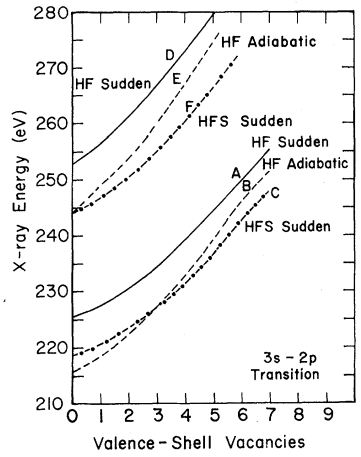

FIG. 3.62. $3s$–$2p$ x-ray energy for Ar atoms with various states of ionization where an additional $2p$ vacancy has been produced. The labeling is the same as in Fig. 3.60.

remains surprising that similar spectra are obtained for C, Al, Si, and Fe targets.

The requirement that a prior vacancy be brought by one of the collision partners into the final collision is also invoked by Saris *et al.* to explain Ar and Si K x rays that are observed in their spectra. This mechanism for producing *characteristic* x rays not otherwise consistent with MO systematics has been discussed in some detail by Macek, Cairns, and Briggs (1972).

3.4.4 Transition Energy Calculations

As discussed in Sec. 3.4, it is common to make comparisons of experimental spectral data with calculated transition energies. The most frequently used comparisons are with Hartree–Fock or Hartree–Fock–Slater calculations using a "sudden" approximation, i.e., using Koopman's theorem. For this approximation, it is assumed that the vacancy production and subsequent filling of the vacancy both occur in times short compared to the relaxation times for the atomic wave functions, so that the initial state orbital energies can be used. Thus, for a neutral atom, the K_α x-ray energy is calculated in the sudden approximation by finding the difference in ground-state orbital energies of the $1s$ and $2p$ orbitals. Similarly, the corresponding K–L_1M_1 Auger energy is calculated by subtracting the $2s$ and $3s$ orbital energies from the $1s$ orbital energy.

An alternative approach uses the assumption that the atom has relaxed fully to the inner-shell vacancy. Then the appropriate transition energies are given by differences of total energies calculated for both the initial and final states. This is referred to as a relaxed or adiabatic approximation.

The "sudden" approximation is the most convenient, but, for slow, heavy-ion collisions it violates the adiabaticity assumptions commonly used in describing such collisions. If the only disturbance of an atom is the removal of an inner-shell electron, the actual transition energies should lie between the predictions based on the sudden and the adiabatic models. This latter, of course, is a gross idealization for heavy ion–atom collisions, where many processes may be simultaneously occurring.

Despite these objections, these models provide at least a good first approximation to these energies. Larkins (1971a) has investigated the use of adiabatic and sudden approximations using HF wave functions. He calculates orbital energies, Auger, and x-ray energies, for the Ar atom for several stages of ionization using both models. He concludes, based on several neutral atom comparisons, that the adiabatic model produces results in closer agreement with the experiment.

We have used HFS (Herman-Skillman) calculations to compare with Larkins results. Figures 3.60 and 3.61 show the $L_{2,3}$, M_1, and $M_{2,3}$ orbital energies using HF sudden (labeled A), HF adiabatic (labeled B), and HFS sudden (labeled C) for ground-state Ar ions, as functions of the number of valence ($M_{2,3}$) shell vacancies. The curves labeled D, E, and F are similar results, but with one additional $L_{2,3}$ shell vacancy. We see that the HFS sudden values lie within 5% (and usually much closer than that) of the HF adiabatic values.

Since differences are our primary interest, and these can magnify small discrepancies, we have plotted the $3s \rightarrow 2p$ x-ray energies from these three approximations in Fig. 3.62. The labeling is the same as in the previous figures. We see that all three models predict these x-ray energies within 5% of each other, and that the HFS sudden model gives values generally close to the HF adiabatic values.

Unfortunately, 5% is not quite good enough for identification of close-lying spectral lines. As the experimental investigations improve in accuracy and resolution, such estimates will become totally inadequate as aids in interpretation. A proper, time-dependent treatment of the atomic transition, though unavailable at this time, will become an essential tool in spectral investigations.

ACKNOWLEDGMENTS

The authors acknowledge contributions made to this review by Dr. J. M. Khan. He provided us with the summary in Appendix 1 of x-ray cross sections for incident light ions, and helped during many conversations in formulating the scope of the paper. We thank Mr. R. C. Der for the support that he has given us during the course of the work.

One of us (JDG) would like to thank NORDITA and the Research Institute for Physics, Stockholm, Sweden, for hospitality during which a portion of the work reported herein was accomplished. We gratefully acknowledge the encouragement and support of Dr. E. Goldberg, head of the Experimental Physics Division at Livermore.

APPENDIX 1

TABLE A1. Summary of x-ray production cross section measurements for incident protons, deuterons, and alpha particles.

Z	Element	Shell	Projectile	Projectile energy	Target configuration	Reference
4	Be	K	p	10–200 keV	Thick	a
6	C	K	p	1.5 MeV	Thick	b
			p	15–1908 keV	Thick	c
			p	15–50 keV	Thick	d
			α	60–200 keV	Thick	d
8	O	K	p	20–100 keV	Thin Al_2O_3	e
12	Mg	K	p	25–1700 keV	Thick	f, c
			α	1–5 MeV	Foil	g
			p	125–200 keV	Thick	h
			α	125–200 keV	Thick	h
13	Al	K	p	1.5 MeV	Thick	b
			p	25–1700 keV	Thick	f, c
			p	90–200 keV	Thick	i
			d	180–360 keV	Thick	i
			α	1–5 MeV	Foil	g
			p	80–200 keV	Thick	j
			α	180–400 keV	Thick	j
			p	30–200 keV	Thick	h
			^{3}He	40–200 keV	Thick	h
			α	60–200 keV	Thick	h
18	Ar	L	p	70–100 keV	Gas	k
20	Ca	K	p	2–25 MeV	Foil	l
22	Ti	K	p	200–500 keV	Thick	m
			p	1.5 MeV	Thick	b
			p	2–25 MeV	Foil	l
			p	90–170 keV	Thick	i
			d	180–340 keV	Thick	i
26	Fe	K	p	140–1300 keV	Thick	n
			p	441 keV	Thick	m
			p	1.5 MeV	Thick	b
			p	160 MeV	Foil	o
			α	30–80 MeV	Foil	p
			p	700–2500 keV	Foil	q
28	Ni	K	p	5–28 MeV	Foil	l
			α	1.5–5.3 MeV	Foil	r
			α	30–80 MeV	Foil	p
29	Cu	K	p	200–1215 keV	Thick	s
			p	140–1200 keV	Thick	n
			p	400–1000 keV	Foil	t
			p	200–500 keV	Thick	m
			p	1.5 MeV	Thick	b
			p	150–500 keV	Thick	f
			p	160 MeV	Foil	o
			d	600–1000 keV	Foil	t
			α	30–80 MeV	Foil	p
			p	700–2500 keV	Foil	q
			α	1.5–5.3 MeV	Foil	s
			α	700–1000 keV	Foil	r
		L	p	1.5 MeV	Thick	b
			p	90–180 keV	Thick	i
			d	180–360 keV	Thick	i
		L_{III}	p	25–1700 keV	Thick	u, v

TABLE A1 (*Continued*)

Z	Element	Shell	Projectile	Projectile energy	Target configuration	Reference
30	Zn	K	p	700–2500 keV	Foil	q
40	Zr	K	p	200–500 keV	Thick	m
			p	160 MeV	Foil	o
			α	30–80 MeV	Foil	p
		L	p	441 keV	Thick	m
41	Nb	K	α	30–80 MeV	Foil	p
42	Mo	K	p	2.4 MeV	Thick	w
			p	250–1610 keV	Thick	s
			p	240–1200 keV	Thick	n
			p	441 keV	Thick	m
			p	160 MeV	Foil	o
			α	1.5–5.3 MeV	Foil	r
		L	p	200–500 keV	Thick	m
			p	1.5 MeV	Thick	b
			p	90–170 keV	Thick	i
			d	180–340 keV	Thick	i
45	Rh	K	p	160 MeV	Foil	o
			α	30–80 MeV	Foil	p
46	Pd	K	α	30–80 MeV	Foil	p
47	Ag	K	p	1.70–2.88 MeV	Thick	w
			p	260–1200 keV	Thick	n
			p	600–1000 keV	Foil	t
			p	160 MeV	Foil	o
			p	2–30 MeV	Foil	x
			α	30–80 MeV	Foil	p
		L	p	441 keV	Thick	m
			p	1.5 MeV	Thick	b
			p	2–30 MeV	Foil	x
			p	120–210 keV	Thick	i
			d	180–360 keV	Thick	i
			p	700–2500 keV	Foil	q
48	Cd	L	p	200–500 keV	Thick	m
50	Sn	K	p	260–1040 keV	Thick	n
			p	160 MeV	Foil	o
			α	30–80 MeV	Foil	p
		L	α	30–80 MeV	Foil	p
52	Te	L	p	441 keV	Thick	m
56	Ba	K	p	160 MeV	Foil	o
		L	p	441 keV	Thick	m
60	Nd	L	p	500–1700 keV	Thick	c
		M	p	25–100 keV	Thick	y
			p	500–1700 keV	Thick	c
62	Sm	K	p	160 MeV	Foil	o
		L	p	500–1700 keV	Thick	c
		M	p	25–100 keV	Thick	y
			p	500–1700 keV	Thick	c
64	Gd	L	p	441 keV	Thick	m
			p	500–1700 keV	Thick	c
		M	p	25–100 keV	Thick	y
			p	500–1700 keV	Thick	c

TABLE A1 (*Continued*)

Z	Element	Shell	Projectile	Projectile energy	Target configuration	Reference
65	Tb	K	p	160 MeV	Foil	o
		L	p	500–1700 keV	Thick	c
		M	p	25–100 keV	Thick	y
			p	500–1700 keV	Thick	c
66	Dy	L	p	500–1700 keV	Thick	c
		M	p	25–100 keV	Thick	y
			p	500–1700 keV	Thick	c
67	Ho	L	p	500–1700 keV	Thick	c
		M	p	25–100 keV	Thick	y
			p	500–1700 keV	Thick	c
68	Er	L	p	441 keV	Thick	m
69	Tm	L	p	441 keV	Thick	m
			α	30–80 MeV	Foil	p
70	Yb	L	p	441 keV	Thick	m
		M_V	p	30–100 keV	Thick	z
71	Lu	L	p	441 keV	Thick	m
72	Hf	L	p	441 keV	Thick	m
		M	p	50–200 keV	Thick	j, aa
			α	200–400 keV	Thick	j, aa
73	Ta	K	p	1.92–3.15 MeV	Thick	w
			p	1–1.25 MeV	Thick	n
			p	160 MeV	Foil	o
		L	p	1.5–4.25 MeV	Thick	bb
			p	200–500 keV	Thick	m
			p	1.5 MeV	Thick	b
			α	30–80 MeV	Foil	p
		M	p	70–190 keV	Thick	aa
			α	210–360 keV	Thick	aa
74	W	L	p	441 keV	Thick	m
		M	p	90–180 keV	Thick	i
			d	180–360 keV	Thick	i
			p	70–200 keV	Thick	aa
			α	180–380 keV	Thick	aa
75	Re	L	p	441 keV	Thick	m
76	Os	L	p	441 keV	Thick	m
77	Ir	L	p	441 keV	Thick	m
78	Pt	K	p	160 MeV	Foil	o
		L	p	441 keV	Thick	m
		M	p	441 keV	Thick	m

TABLE A1 (*Continued*)

Z	Element	Shell	Projectile	Projectile energy	Target configuration	Reference
79	Au	*K*	*p*	2.4 MeV	Thick	w
			p	160 MeV	Foil	o
		L	*p*	1.5–4.25 MeV	Thick	bb
			p	200–500 keV	Thick	m
			p	700–2500 keV	Foil	q
			p	70–200 keV	Thick	aa
			α	200–300 keV	Thick	aa
			α	30–80 MeV	Foil	p
		M	*p*	441 keV	Thick	m
80	Hg	*L*	*p*	441 keV	Thick	m
		M	*p*	441 keV	Thick	m
82	Pb	*K*	*p*	1.92–2.88 MeV	Thick	w
			p	160 MeV	Foil	o
		L	*p*	1.5–4.25 MeV	Thick	bb
			p	441 keV	Thick	m
		M	*p*	200–500 keV	Thick	m
83	Bi	*L*	*p*	441 keV	Thick	m
		M	*p*	441 keV	Thick	m
			p	70–200 keV	Thick	aa
			α	300 keV	Thick	aa
92	U	*K*	*p*	160 MeV	Foil	o
		L	*p*	1.5–4.0 MeV	Thick	bb
			p	441 keV	Thick	m
		M	*p*	200–500 keV	Thick	m
			p	80–200 keV	Thick	aa

[a] Terasawa, Tamura, and Kamada (1971).
[b] Ogier *et al.* (1964).
[c] Khan, Potter, and Worley (1965).
[d] Terasawa, Inouye, and Kamei (1970).
[e] Hart *et al.* (1969).
[f] Khan and Potter (1964).
[g] Sellers, Hanser, and Wilson (1969).
[h] Brandt, Laubert, and Sellin (1966).
[i] Shima, Makino, and Sakisaka (1971).
[j] Needham and Sartwell (1970a).
[k] Saris and Onderdelinden (1970).
[l] Bissinger *et al.* (1970).
[m] Jopson, Mark, and Swift (1962).
[n] Messelt (1958).
[o] Jarvis, Whitehead, and Shah (1972).
[p] Watson, Lewis, and Natowitz (1970).
[q] Fahlenius and Jauho (1971).
[r] Buhring and Haxel (1957).
[s] Hansteen and Messelt (1956).
[t] Singh (1957).
[u] Khan, Potter, and Worley (1964a).
[v] Khan, Potter, and Worley (1966).
[w] Lewis, Simmons, and Merzbacher (1953).
[x] Bissinger, Shafroth, and Waltner (1972).
[y] Khan, Potter, and Worley (1964b).
[z] Khan, Potter, and Worley (1964c).
[aa] Needham and Sartwell (1970b).
[bb] Bernstein and Lewis (1954).

APPENDIX 2

Table A2 lists the scaled cross sections for K-shell vacancy production by proton impact. In the table headings, u is the binding energy of the shell in question (in keV), $\lambda = m_1/m_e$ is the projectile mass in electron mass units, E the projectile energy (in keV), Z_1 is the projectile charge, and σ is the cross section in cm^2.

To use the Table for other shells, the scaled cross section must be multiplied by the ratio of the number of equivalent electrons in that shell to those in the K shell, i.e., by $N_e/2$. These values should be valid for most light projectiles as well.

TABLE A2. Binary encounter approximation cross sections.

$E/\lambda u$	$u^2\sigma/Z_1^2$ (keV^2 cm^2)	$E/\lambda u$	$u^2\sigma/Z_1^2$ (keV^2 cm^2)
8.35×10^{-3}	1.25×10^{-24}		
1.67×10^{-2}	1.79×10^{-23}	4.65×10^{-1}	6.55×10^{-20}
2.50	7.38	5.82	7.70
3.34	1.92×10^{-22}	6.99	8.42
4.17	3.89	8.15	8.84
5.01	6.80	9.32	9.03
5.84	1.07×10^{-21}	1.05×10^{0}	9.07
6.68	1.57	1.16	9.01
7.51	2.18	1.28	8.87
8.35	2.89	1.51	8.49
9.18	3.71	1.75	8.04
1.00×10^{-1}	4.62	1.98	7.59
1.09	5.63	2.10	7.36
1.17	6.72	2.45	6.73
1.25	7.90	2.79	6.17
1.34	9.15	3.03	5.83
1.42	1.05×10^{-20}	3.26	5.53
1.59	1.33	3.49	5.25
1.75	1.62	3.73	4.99
1.92	1.93	3.96	4.76
2.00	2.09	4.19	4.54
2.17	2.41	4.54	4.25
2.25	2.57	5.01	3.92
2.50	3.06	5.84	3.42
2.75	3.54	6.67	3.03
3.01	4.01	7.51	2.72
3.26	4.45	8.34	2.47
3.51	4.88	9.18	2.26
4.17	5.87	10.0	2.08

REFERENCES

Aberg, T., 1967, Phys. Rev. **156,** 35.

Afrosimov, V. V., Yu. S. Gordeev, M. N. Panov, and N. V. Fedorenko, 1963, Proc. Sixth Intern. Conf. on Ionization of Gases, Paris, Eds. P. Hubert and E. Cremieu-Alcav, p. 111.

——, Yu. S. Gordeev, M. N. Panov, N. V. Fredorenko, 1964, Zh. Tekhn, Fiz. **34,** 1613; 1624; 1637 [Soviet Phys.—Tech. Phys. **9,** (1965) 1248; 1256; 1265].

——, Yu. S. Gordeev, M. N. Panov, and N. V. Fedorenko, 1966, Zh. Tekhn. Fiz. **36,** 123 [Soviet Phys.—Tech. Phys. **11** (1966) 89].

——, Yu. S. Gordeev, A. M. Polyanski, and A. P. Shergin, 1969, Zh. Eksp. Teor. Fiz. **57,** 806 [Soviet Phys.—JETP **30** (1970), 441].

——, Yu. S. Gordeev, A. M. Polyansky, and A. P. Shergin, 1971, VII ICPEAC Abstracts (North-Holland Publ. Co., Amsterdam), p. 397.

Armbruster, P., 1962, Z. Physik, **166,** 341.

——, E. Roeckl, H. J. Specht, and A. Vollmer, 1964, Z. Naturforsch **19A,** 1301.

Bambynek, W., B. Craseman, R. W. Fink, H.-U. Freund, H. Mark, C. D. Swift, R. E. Price, and P. Venugopala Rao, 1972, Rev. Mod. Phys. **44,** 716.

Bang, J., and J. M. Hansteen, 1959, Kgl. Danske Videnskab Selskab, Mat.-Fys. Medd. **31,** No. 13.

Barat, M., and W. Lichten, 1972, Phys. Rev. **A 6,** 211.

Basbas, G., W. Brandt, and R. Laubert, 1971, Phys. Letters **34A,** 277.

——, W. Brandt, R. Laubert, A. Ratkowski, and A. Schwarzschild, 1971, Phys. Rev. Letters **27,** 171.

Bates, D. R., 1962, in *Atomic and Molecular Processes,* edited by D. R. Bates (Academic P., New York), Chap. 14.

——, and D. A. Williams, 1964, Proc. Phys. Soc. (London) **83,** 425.

Bernstein, E. M., and H. W. Lewis, 1954, Phys. Rev. **95,** 83.

Bierman, D. J., W. F. Van der Weg, C. Snoek, and D. Onderdelinden, 1970, Physica **46,** 244.

Bingham, F. W., 1969, Phys. Rev. **182,** 180.

Bissinger, G. A., J. M. Joyce, E. J. Ludwig, W. S. Moever, and S. M. Shafroth, 1970, Phys. Rev. A **1,** 841.

——, S. M. Shaforth, and A. W. Waltner, 1972, Phys. Rev. A**5** 2046.

Brandt, W., R. Laubert, and I. Sellin, 1966, Phys. Letters **21,** 518; Phys. Rev. **151,** 56.

——, and R. Laubert, 1970, Phys. Rev. Letters **24,** 1037.

Briand, J. P., P. Chevallier, M. Tavernier, and J. P. Rozet, 1971, Phys. Rev. Letters **27,** 777.

Briggs, J. S., and J. Macek, 1972, J. Phys. B **5,** 579.

Buhring, W., and O. Haxel, 1957, Z. Physik **148,** 653.

Burch, D., and P. Richard, 1970, Phys. Rev. Letters **25,** 983.

——, and P. Richard, 1971, private communication.

——, P. Richard, and R. L. Blake, 1971, Phys. Rev. Letters **26,** 1355.

Cacak, R. K., 1969, Ph.D. Thesis, University of Nebraska (unpublished).

——, and T. Jorgensen, Jr. 1970, Phys. Rev. A **2,** 1322.

——, Q. C. Kessel, and M. E. Rudd, 1970, Phys. Rev. **A2,** 1327.

Cairns, J. A., D. F. Holloway, and R. S. Nelson, 1970, *Atomic Collision Phenomena in Solids,* Proceedings of Int. Conference Univ. of Sussex, Sept. 1969 (North-Holland Publ. Co.), p. 541.

Chen, J. C. Y., 1964, J. Chem. Phys. **40,** 3513.

Clementi, E., 1965, IBM J. Res. Develop. **9,** 2, plus supplementary tables.

Choi, B., and E. Merzbacher, 1969, Phys. Rev. **177,** 233.

——, 1971, Phys. Rev. **A4,** 1002.

Coates, W. M., 1934, Phys. Rev. **46,** 542.

Coleman, J. P., 1969, *Case Studies in Atomic Collision Physics,* edited by E. W. McDaniel and M. R. C. McDowell (North-Holland Publ. Co., Amsterdam).

Cunningham, M. E., R. C. Der, R. J. Fortner, T. M. Kavanagh, J. M. Khan, C. B. Layne, E. J. Zaharis, and J. D. Garcia, 1970, Phys. Rev. Letters **24,** 931.

Datz, S., C. D. Moak, B. R. Appleton, and T. R. Carlson, 1971, Phys. Rev. Letters **27,** 363.

Del Boca, R., H. C. Hayden, and G. M. Thomson, 1971, Phys. Rev. Letters **26,** 1417.

Der, R. C., T. M. Kavanagh, J. M. Khan, B. P. Curry, and R. J. Fortner, 1968, Phys. Rev. Letters **21,** 1731.

——, T. A. Boster, M. E. Cunningham, R. J. Fortner, T. M. Kavanagh, and J. M. Khan, 1970, Rev. Sci. Instr. **41,** 1797.

——, R. J. Fortner, T. M. Kavanagh, and J. M. Khan, 1971a, Phys. Rev. **A4,** 556.

——, R. J. Fortner, T. M. Kavanagh, J. M. Khan, and J. D. Garcia, 1971b, Phys. Letters **36A,** 239.

——, R. J. Fortner, T. M. Kavanagh, and J. D. Garcia, 1971c, Phys. Rev. Letters **27,** 1631.

Dick, C. E., and A. C. Lucas, 1970, Phys. Rev. A **2,** 580.

Edwards, A. K., 1967, Ph.D. Thesis, University of Nebraska, (unpublished).

——, and M. E. Rudd, 1968, Phys. Rev. **170,** 140.
Everhart, E., R. J. Carbone, and G. Stone, 1955, Phys. Rev. **98,** 1045.
——, and Q. C. Kessel, 1965, Phys. Rev. Letters **14,** 247.
——, and Q. C. Kessel, 1966, Phys. Rev. **146,** 27.
Fahlenius, A., and P. Jauho, 1971, Ann. Acad. Sci. Fennicae Avi. **367,** 3.
Fano, U., and W. Lichten, 1965, Phys. Rev. Letters **14,** 627.
——, and G. Hermann, 1969, Phys. Rev. Letters **23,** 157.
——, G. Hermann, and Q. C. Kessel, 1971, Phys. Rev. Letters **27,** 771.
——, G. Hermann, and K. J. Smith, 1971, Phys. Rev. **A3,** 1591.
——, and G. A. Larsen, 1971, *VII ICPEAC Abstracts* (North-Holland Publ. Co., Amsterdam), p. 392.
Fischer, D. W., and W. L. Baun, 1965, J. Appl. Phys. **36,** 534.
Fortner, R. J., B. P. Curry, R. C. Der, T. M. Kavanagh, and J. M. Khan, 1969, Phys. Rev. Letters **185,** 164.
——, R. C. Der, and T. M. Kavanagh, 1971, Phys. Letters **37A,** 259.
——, R. C. Der, T. M. Kavanagh, and J. D. Garcia, 1972, J. Phys. B **5,** L73.
Garcia, J. D., 1970a, Phys. Rev. **A1,** 280.
——, 1970b, Phys. Rev. **A1,** 1402.
——, 1971, Phys. Rev. **A4,** 955.
Gryzinski, M., 1965, Phys. Rev. **138A,** 336.
Hansteen, J. M., and T. S. Messelt, 1956, Nuclear Physics **2,** 526.
——, and O. P. Mosebekk, 1970, Z. Physik **234,** 281.
Hart, R. R., F. W. Reuter, III, H. P. Smith, Jr., and J. M. Kahn, 1969, Phys. Rev. **179,** 4.
Henneberg, W., 1933, Z. Physik **86,** 592.
Hund, F., 1927, Z. Physik **40,** 742.
Jamnik, D., and C. Zupancic, 1957, Med. Dan. Vid. Selsk. **31,** No. 2.
Jarvis, O. N., C. Whitehead, and M. Shah, 1972, Phys. Rev. A **5,** 1198.
Jopson, R. C., H. Mark, and C. D. Swift, 1962, Phys. Rev. **127,** 1612.
Kavanagh, T. M., M. E. Cunningham, R. C. Der, R. J. Fortner, J. M. Khan, E. J. Zaharis, and J. D. Garcia, 1970, Phys. Rev. Letters **25,** 1473.
——, R. C. Der, R. J. Fortner, and M. E. Cunningham, 1972, private communication.
Kessel, Q. C., 1969a, *Case Studies in Atomic Collision Physics I,* Eds., E. W. McDaniel and M. R. C. McDowell (North-Holland Publishing Company, Amsterdam), p. 401.
——, 1969b, VI ICPEAC Abstracts (MIT Press), p. 751, 754.
——, 1969c, Bull. Am. Phys. Soc. **14,** 946.
——, and E. Everhart, 1966, Phys. Rev. **146,** 16.
——, M. P. McCaughey, and E. Everhart, 1966a, Phys. Rev. Letters **16,** 1189.
——, M. P. McCaughey, and E. Everhart, 1966b, Phys. Rev. Letters **17,** 1170.
Kessel, Q. C., M. P. McCaughey, and E. Everhart, 1967, Phys. Rev. **153,** 57.
——, P. H. Rose, and L. Grodzins, 1969, Phys. Rev. Letters **22,** 1031.
——, A. Russek, and E. Everhart, 1965, Phys. Rev. Letters **14,** 484.
Khan, J. M., and D. L. Potter, 1964, Phys. Rev. **133,** A890.
——, D. L. Potter, and R. D. Worley, 1964a, Phys. Rev. **134,** A316.
——, D. L. Potter, and R. D. Worley, 1964b, Phys. Rev. **135,** A511.
——, D. L. Potter, and R. D. Worley, 1964c, Phys. Rev. **136,** A108.
——, D. L. Potter, and R. D. Worley, 1965, Phys. Rev. **139,** A1735.
——, D. L. Potter, and R. D. Worley, 1966, Phys. Rev. **145,** 23.
Khandelwal, G. S., and E. Merzbacher, 1966, Phys. Rev. **151,** 12.
Knudson, A. R., D. J. Nagel, P. G. Burkhalter, and K. L. Dunning, 1971, Phys. Rev. Letters **26,** 1149.
——, P. G. Burkhalter, D. J. Nagel, 1972, private communication.
Knystautas, E. J., Q. C. Kessel, R. Del Boca, and H. C. Hayden, 1970, Phys. Rev. **A1,** 825.
Kostroun, V. O., M. H. Chen, and B. Crasemann, 1971, Phys. Rev. **A3,** 533; **4,** 1.
Krause, M. O., T. A. Carlson, and R. D. Dismukse, 1968, Phys. Rev. **170,** 37.
——, F. A. Stevie, L. J. Lewis, T. A. Carlson, and W. E. Moddeman, 1970, Phys. Letters **31A,** 81.
Kunzl, V., 1936, Z. Phys. **99,** 1481.
Laegsgaard, E., L. C. Feldman, and J. U. Andersen, 1971, *VII ICPEAC Abstracts* (North-Holland Publ. Co., Amsterdam), p. 414.
Landau, L., 1932, Physik. Z. Sowjetunion **2,** 46.
Larkins, F. P., 1971a, J. Phys. B **4,** 14.
——, 1971b, J. Phys. B **4,** L29.
——, 1972, J. Phys. B **5,** 571.
Lewis, H. W., B. E. Simmons, and E. Merzbacher, 1953, Phys. Rev. **91,** 943.
——, J. B. Natowitz, and R. L. Watson, 1971, Phys. Rev. Letters **26,** 481.
——, R. L. Watson, and J. B. Natowitz, 1972, Phys. Rev. A **5,** 1773.
Lichten, W., 1967, Phys. Rev. **164,** 131.
Lipsky, L., and A. Russek, 1966, Phys. Rev. **142,** 59.
Lutz, H. O., H. J. Stein, S. Datz, and C. D. Moak, 1972, Phys. Rev. Letters **28,** 8.
MacDonald, J. R., and M. D. Brown, 1972, Phys. Rev. Letters **29,** 4.
Macek, J., J. A. Cairns, and J. S. Briggs, 1972, Phys. Rev. Letters **28,** 1298.
McCaughey, M. P., E. J. Knystautus, H. C. Hayden, and E. Everhart, 1968a, Phys. Rev. Letters **21,** 65.
——, E. J. Knystautus, and E. Everhart, 1968b, Phys. Rev. **175,** 14.
McGuire, E. J., 1969, Phys. Rev. **185,** 1.
McGuire, J. H., and M. H. Mittleman, 1972, Phys. Rev. **A5,** 1972.
Mehlhorn, W., D. Stalherm, 1968, Z. Physik **217,** 294.
Merzbacher, E., and H. W. Lewis, 1958, *Handbuch der Physik* (Springer-Verlag, Berlin) **34,** 166.
Messelt, S., 1958, Nuclear Physics **5,** 435.
Mokler, P. H., 1971, Phys. Rev. Letters **26,** 811.
Morgan, G. H., and E. Everhart, 1962, Phys. Rev. **128,** 667.
Mott, N. F., and S. N. Massey, 1965, *The Theory of Atomic Collisions* (Oxford U. P., London), 3rd edition.
Mulliken, R. S., 1928, Phys. Rev. **32,** 186.
Needham, P. B., Jr., and B. D. Sartwell, 1970a, Phys. Rev. **A2,** 27.
——, and B. D. Sartwell, 1970b, Phys. Rev. **A2,** 1686.
Nelson, R. S., J. A. Cairns, and N. Blamires, 1970, Radiation Effects **6,** 131.
Northcliffe, L. C., and R. F. Schilling, 1970, Nuclear Data Tables **7,** 233.
Ogier, W. T., G. J. Lucas, J. S. Murray, and T. E. Holzer, 1964, Phys. Rev. **134,** A1070.
Ogurtsov, G. N., I. P. Flaks, S. V. Avakyan, and N. V. Fedorenko, 1968, Zh. Etf Pis. Red. **8,** 541 [Soviet Phys.—JETP Letters **8,** 330].
——, I. P. Flaks, and S. V. Avakyan, 1969a VI ICPEAC Abstracts (MIT Press), p. 274.
——, I. P. Flaks, and S. V. Avakyan, 1969b, Zh. Eksp. Teor. Fiz. **57,** 27 [Soviet Phys.—JETP **30** (1970) 16].
——, I. P. Flaks, and S. V. Avakyan, 1969c, Zh. Tekh. Fiz. **39,** 1293 [Soviet Phys.—Tech. Phys., **14,** (1970), 972].
——, I. P. Flaks, and S. V. Avakyan, 1970, Zh. Tekh. Fiz. **40,** 2124 [Soviet Phys.—Tech. Phys. **15** (1971), 1656].
——, 1971, *VII ICPEAC Abstracts* (North-Holland Publ. Co., Amsterdam), p. 400.
——, 1972, Rev. Mod. Phys. **44,** 1.
O'Malley, T. F., 1966, Phys. Rev. **150,** 14.
——, 1967, Phys. Rev. **162,** 98.
Richard, P., I. L. Morgan, T. Furuta, and D. Burch, 1969, Phys. Rev. Letters **23,** 1009.
Richard, P., T. I. Bonner, T. Furuta, I. L. Morgan, and J. R. Rhodes, 1970, Phys. Rev. A **2,** 1044.
——, 1972, private communication.
Rudd, M. E., and T. Jorgensen, Jr., 1963, Phys. Rev. **131,** 666.
——, 1966, Rev. Sci. Instr. **37,** 971.
——, T. Jorgensen, Jr., and D. J. Volz, 1966, Phys. Rev. **151,** 28.
Russek, A., and J. Meli, 1970, Physica **46,** 222.
Sakisaka, M., 1971, private communication.
Saris, F. W., and D. Onderdelinden, 1970, Physica **49,** 441.
——, 1971, Physica **52,** 290.

——, and D. J. Bierman, 1971, Phys. Letters **35A,** 199.
——, W. F. Van der Weg, H. Tawara, and R. Laubert, 1972, Phys. Rev. Letters **28,** 717.
Sellers, B., F. A. Hanser, and H. H. Wilson, 1969, Phys. Rev. **182,** 90.
Shima, K., I. Makino, and M. Sakisaka, 1971, J. Phys. Soc. Japan **30,** 611.
Sidis, V., and H. Lefebvre-Brion, 1971, J. Phys. B: Atom. Molec. Phys. **4,** 1040.
Singh, B., 1957, Phys. Rev. **107,** 711.
Slater, J. C., 1930, Phys. Rev. **36,** 57.
——, 1963, *The Quantum Theory of Molecules and Solids, Vol. II. Molecules* (Academic, New York).
Smith, F. T., 1969, Phys. Rev. **179,** 111.
Snoek, C., R. Geballe, W. F. Van der Weg, P. K. Rol, and D. J. Bierman, 1965, Physica **31,** 1553.
Specht, H. J., 1965., Z. Physik **185,** 301.
Stein, H. J., H. O. Lutz, P. H. Mokler, K. Sistemich, and P. Armbruster, 1970, Phys. Rev. Letters **24,** 701; see also P. H. Mokler, H. O. Lutz, H. J. Stein, and P. Armbruster, 1970, Nucl. Instr. Meth. **90,** 321.
——, H. O. Lutz, P. H. Mokler, and P. Armbruster, 1972, Phys. Rev. A **5,** 2126.
Stolterfoht, N., 1972, private communication.
Stuckelberg, E. C. G., 1932, Helv. Phys. Acta **5,** 369.
Swift, C. D., 1972, private communication.
Tanaka, M., and I. Nonaka, 1937, Proc. Phys.—Math. Soc. Japan **20,** 33.
Taulbjerg, K., and P. Sigmund, 1972, Phys. Rev. A **5,** 1285, and private communication.
Terasawa, M., T. Inouye, and H. Kamei, 1970, J. Phys. Soc. Japan **29,** 1394.
——, T. Tamura, and H. Kamada, 1971, *VII ICPEAC Abstracts* (North-Holland Publ. Co., Amsterdam), p. 410.
——, 1971, private communication.
Thomas, B. K., and J. D. Garcia, 1969, Phys. Rev. **159,** 39.
Thomson, G. M., P. C. Laudieri, and E. Everhart, 1970, Phys. Rev. **A1,** 1439.
Thulstrup, E. W., and H. Johansen, 1971, *VII ICPEAC Abstracts* (North-Holland Pub. Co., Amsterdam), p. 118.
Toburen, L. H., 1971, Phys. Rev. A **3,** 216.
——, 1972, Phys. Rev. **A5,** 2482.
Veigele, D. E., D. E. Stevenson, and E. M. Henry, 1969, J. Chem. Phys. **50,** 5404.
Volz, D. J., and M. E. Rudd, 1970, Phys. Rev. **A2,** 1395.
Vriens, L., 1969, *Case Studies in Atomic Collision Physics,* Eds. E. W. McDaniel and M. R. C. McDowell (North-Holland Publ. Co., Amsterdam).
——, 1970, Physica, **49,** 602.
Walters, D. L., and C. P. Bhalla, 1971a, Phys. Rev. **A3,** 519.
——, and C. P. Bhalla, 1971b, Phys. Rev. **A4,** 2164.
Watson, R. L., C. W. Lewis, and J. B. Natowitz, 1970, Nuclear Physics **A154,** 561.
——, and T. K. Li, 1971, Phys. Rev. A **4,** 132.
Zener, C., 1932, Proc. Roy. Soc. (London) **A137,** 696.